Developing Brain Connectivity- Effects of Parcellation Scale on Network Analysis in Neonates

Schirmer, Markus D.

Awarding institution:
King's College London

Developing Brain Connectivity

Effects of Parcellation Scale on Network Analysis in Neonates

Markus D. Schirmer

Submitted in fulfilment of the requirements for the degree of
Doctor of Philosophy

Division of Imaging Sciences and Biomedical Engineering
School of Medicine
King's College London

July 2015

KING'S College LONDON

Abstract

Diffusion magnetic resonance imaging (dMRI), tractography and the use of network measures have combined to form an established approach for exploring brain connectivity. When applied to the human brain, a definition of regions of interest (ROIs) which act as network nodes is required. In adults, regions commonly represent brain areas that are assumed to be functionally coherent. During early development however, a complete set and locations of ROIs in the brain is yet to be established. This motivates the use of random parcellation schemes with varying numbers of regions or scales. However, network measures can be scale dependent, making comparisons across multiple scales challenging and hindering group comparisons.

To address such scale dependence, network measures are commonly normalised using random surrogate networks which act as a baseline. In this work, the efficacy of commonly used normalisation techniques is determined and new methods for generating randomised surrogate networks are introduced. Furthermore, a subset of measures is derived by investigating inter-measure correlations and the framework is then applied to serial dMRI data of a preterm cohort. It is shown that a new method for generating surrogate networks for normalisation improves on established approaches and eliminates scale dependencies over a local range, allowing for meaningful group comparison.

While normalisation may be used for group comparison over a local range, scale dependence can remain over larger ranges. This work shows that the nature of the scale dependence varies between cohorts, and proposes a multi-scale framework for group comparison. Using this framework to characterise the scale dependence, it is possible to differentiate the groups of neonates studied. This approach, however, requires the calculation of networks at multiple scales. Therefore the use of a node-merger scheme is also proposed to infer network properties at a coarse scale from a single network estimated at a fine scale. This approach allows for multi-scale group comparison based on a single starting network.

Contents

List of Figures

List of Tables

Acknowledgements

I would like to thank my supervisors, Paul Aljabar and Jo Hajnal, for giving me the opportunity to undertake my PhD and for supporting me in my efforts to become an independent researcher. My thanks also go to Robert Leech and Martijn Van den Heuvel for their time and commitment in the process of examining my thesis.

For useful advise and discussions throughout my PhD, I would like to thank in particular Gareth Ball and Daniel Rueckert. Furthermore, I would like to thank David Edwards for the opportunity to animate the logo for the developing human connectome project (dHCP). My thanks also go to my colleagues at King's College London, who were always willing to lent me an ear and offered encouragement throughout this journey.

Besonderen Dank geht an meine Freunde und Familie. Mimi und Elli, euch beiden danke ich, dass ihr für mich da seid und wir unsere Leben miteinander teilen, egal wo wir uns gerade befinden. An Matthias, der mir auch die Details von dem erzählt was Zuhause passiert und mich dadurch daran erinnert, dass die Heimat nicht allzu weit entfernt ist. Meiner Schwester möchte ich dafür danken, dass sie mir über all die Jahre ein Vorbild war und auch weiterhin ist und mir immer mit Rat und Tat zur Seite steht. Insbesondere möchte ich meiner Mutter dafür danken, dass sie mir den Rückhalt und den Antrieb gibt niemals aufzugeben und die Gewissheit, dass wir als Familie immer für einander da sind.

Chapter 1

Introduction

The human brain is a remarkably complex system of units which interact with one another to incorporate and process internal and external stimuli. Complex systems cannot simply be studied by investigating the individual units separately, as many features emerge due to their interaction and global connectivity. The study of connections within the brain has indicated that brain organisation is non-random and has led to a wide range of studies investigating its topology [8, 36, 15, 59, 60, 148, 159].

A variety of methods have been used to uncover the underlying connectivity profile in human and non-human brains based on invasive or non-invasive procedures. Tracer studies, for example, were first introduced at the end of the 19th century [170, 171]. They identify connections between regions of the brain by following individual white matter pathways. These studies, however, can only be carried out post-mortem and need a significant number of subjects to be able to map out the connectivity profile of a given species, which prevents comparisons on the subject level [156]. The limitation to groups, in addition to the rarity of human paediatric samples, motivated the development of non-invasive imaging techniques to study developing brain connectivity.

With the development of magnetic resonance imaging (MRI), it became possible to investigate structural and functional connectivity within the living brain [58]. It also allows the study of the development of and changes in the connectivity profiles over the life time. One benefit of MRI, over many other *in-vivo* imaging techniques, lies in the fact that MRI does not use ionising radiation and is generally considered a safe imaging technique [147]. This is particularly important when imaging paediatric patients at younger ages.

A mathematical framework for these investigations, which has gained significant attention in recent years is network theory [29, 138, 154]. Various network-theoretical aspects of brain connectivity have been investigated, such as rich club organisation [8, 36] and segregation and integration [15]. Studies of conditions such as Alzheimer's disease [87], attention deficit hyperactivity disorder (ADHD) [168] and developmental changes due to premature birth [110], have explored the potential of using network theory for characterising group differences within the brain.

The use of network theory relies on the definition of regions within the brain which act as nodes in a graph or network. However, this aspect is particular challenging when studying neonates, due to the lack of a consensus on which parcellation scheme or map of brain regions to use. Nonetheless, studying brain development in the very early stages, where significant changes occur [143], provides an opportunity to uncover biomarkers indicative of neurodevelopmental and neurodegenerative diseases [62, 87, 165, 168], especially in prematurely born infants. Prematurity has been linked, for example, to motor [94, 95], auditory [94, 125], visual [37, 94] and cognitive impairments [94] and it has been suggested that approximately 50% of all infants born prematurely suffer from negative cognitive outcome [175]. Therefore it would be beneficial to find biomarkers to help identify infants at risk and allow for early intervention and support.

Aims and Outline

The aim of this thesis is to develop methods based on global network measures that can be used for comparing networks where the location, size and number of nodes is unknown. The proposed methods are used to investigate brain development after premature birth, where these challenges are relevant due to a lack of consensus on which parcellation scheme to use.

The following chapter begins with a brief overview of the biological aspects of brain development and motivates the investigation of prematurely born infants. It continues by introducing the principles underlying MRI and diffusion MRI in particular, a modality often used to image the developing brain. Chapter 3 continues by discussing the general concepts used in the field of network theory and discusses the background of network measures that are used to analyse brain networks in this work and in the literature. It also highlights the contribution of network theory with respect to neuroscientific investigations. Both, chapters 2 and 3 describe difficulties, such as the lack of a standard

parcellation scheme and the unknown location, size and number of nodes in the brain, that originate when applying network theoretical analyses to the developing brain.

Following this, chapter 4 motivates the use of random parcellations by comparing global network measures calculated using random parcellations with those using atlas based parcellations. It subsequently employs random parcellations to investigate network normalisation as a tool for comparing networks of varying size. This includes an exploration of methods for generating surrogate networks, which may act as a baseline in network theoretic approaches.

Network normalisation may be used for comparing networks at local scales, i.e. small variations in the number of regions. When the variation of number of regions increases, however, the dependence remains and comparison of network measures continues to be challenging. For that reason, chapter 5 investigates how this dependence can be used for comparisons of networks over multiple scales. A multi-scale framework that characterises the global network measures across scales is introduced and utilised for group comparison.

The multi-scale framework discussed in chapter 5 relies on the definition of multiple networks over a range of numbers of brain regions. This leads to additional computational cost compared to using network normalisation, which can use a single observed network for comparison. Chapter 6 subsequently investigates the use of a node-merger scheme which can be used to infer coarse scale information from a single network at a fine scale as a starting point. The utility of this framework is investigated with respect to its efficacy in differentiating between groups using both observed and synthetic networks.

This work concludes in chapter 7 by discussing the limitations of the presented approaches. In addition, section 7.3 outlines potential frameworks which can be used to place an observed network within the spectrum of random surrogate networks. These frameworks will form the foundation of future work which aims to quantify changes of the network type as a result of development or disease.

Chapter 2

Studying the Developing Brain

The human brain undergoes rapid and significant changes in the early stages of development [32]. With advances in non-invasive neuroimaging techniques, it became possible to follow the neuroanatomical development of the human brain safely [11, 32, 70, 82, 83, 137, 147, 154]. Studies have suggested that the time-line of cortical maturation is linked to cognitive milestones depending on the functional demand, where the primary motor and sensory systems mature earliest [55, 136, 137]. Studies have also explored the possibility of using non-invasive imaging techniques to investigate neurodevelopmental disorders, such as autism and attention deficit hyperactivity disorder [5, 84, 115, 125].

The biological aspects of human brain development from the early stages until birth are outlined in this chapter and the study of prematurely born babies is motivated. Furthermore the physical basis of magnetic resonance imaging (MRI) are discussed, followed by an introduction to diffusion weighted MRI and the use of tractography to infer fibre pathways in the human brain *in-vivo*.

2.1 Early Brain Development

In the human embryo, the neural plate starts closing at around 3 weeks of gestational age (GA), forming the predecessor of the central nervous system (CNS) called the neural tube. Subsequently three principal enlargements develop, namely the prosencephalon (forebrain), mesencephalon (midbrain) and the rhombencephalon (hindbrain) (see Figure 2.1). Over the course of gestation, the hindbrain continues to evolve into the cerebellum, pons and medulla

oblongata. Simultaneously, the prosencephalon is subdivided into the diencephalon, the precursor for the optic vesicles, the thalamus and the hypothalamus, as well as the telencephalon, which forms the cerebral hemispheres.

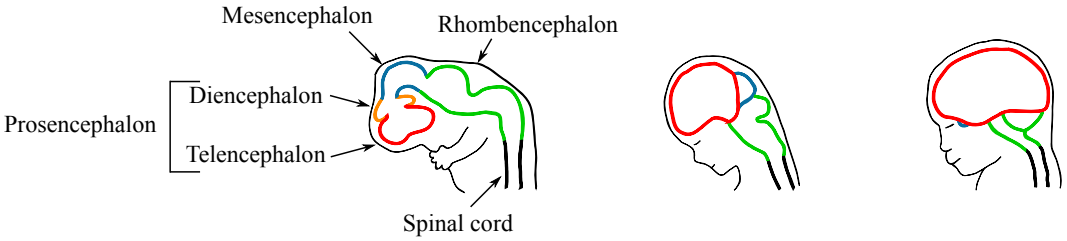

Figure 2.1: Illustration of the three principal enlargements in the human brain, including their development.

The period of 24 to 40 weeks GA is a critical time in terms of neurogenesis, neuronal migration, establishment of structural connections, synaptogenesis, gyrification and cortical expansion, as well as pruning [143]. Neurogenesis occurs mainly during the second trimester of pregnancy, when most neurons of the human brain are formed. The exception to this is the cerebellum, which continues to form neurons until after birth, and the hippocampus, which allows neurons to be formed over the lifespan and is linked to memory formation. The cell bodies of neurons are grey in appearance and as a result make up the so called "grey matter", which is responsible for information processing. From 24 weeks of gestation until around four weeks after birth, rapid cell death occurs and reduces the number of neurons in the brain by half (apoptosis) [82].

After neurons are produced they start migrating towards the developing neocortex [143]. In order to do so they make use of basal processes, which form a scaffolding throughout the brain. Migrating neurons attach themselves to and move along this scaffolding to their respective target regions. The first migrating neurons form a structure called the preplate, which is split into two transient layers, the marginal zone and the subplate. The cortical plate is subsequently formed between the marginal zone and the subplate.

After migrating to the cortex, neurons develop afferent outgrowths, axons, which allow them to communicate using electro-chemical signals. During gestation, axons from the subplate penetrate the cortical plate around 24-26 weeks GA to establish connectivity, which plays an important role in the differentiation of the cerebral cortex [79]. The development of the system of axons (structural connectivity) continues into the postnatal period [78]. Around each axon, myelin sheathes act as electrical insulation for the axons in the brain and help to increase the efficiency of neural signalling. The process of myelination

starts before birth from the brain stem around 29 weeks GA [70] and continues into late adolescence [24]. The structural connectivity is commonly referred to as white matter, due to the white appearance of the myelin.

Once the axon has reached its target neuron, a synaptic connection is formed. Synaptogenesis, the formation of synapses, occurs between the third trimester of gestation and two years postnatal age. It should be noted that different brain regions may reach their maximum synaptic density at different time points of development [68]. Additionally, in contrast to the neuronal density, the synaptic density increases rapidly after birth, which is followed by pruning, reducing the synaptic density by approximately 40% over a person's lifetime [69].

In addition to these microscopic changes, the brain also undergoes macroscropic developmental changes in which the grey matter structure of the cortex forms sulci and gyri. Sulcation and gyrification in the human brain starts with the appearance of the sylvian fissure and central sulcus at approximately 15 and 20 weeks GA, respectively [83]. Although some variation between individual brain development can be found, it has been indicated that sulci and gyri develop according to a developmental schedule [34]. Even though sulci are already present by 28 weeks GA, with secondary and tertiary sulci forming afterwards [34], major landmarks are hard to detect in these early stages. Moreover the sulcation and gyrification of the brain continues after birth [83], however, it has to be noted that this process may be delayed in premature babies [11]. Figure 2.2 summarises the time-line of these developmental events during gestation.

2.1.1 Prematurity

In some cases babies are born premature, i.e. before 37 weeks of pregnancy. Based on their GA, premature born babies can be divided into extremely preterm (before 28 weeks GA), very preterm (28-31 weeks GA), moderate (32-33 weeks GA) and near term or late preterm (34-37 weeks). Figure 2.2 illustrates these categories in relation to the developmental processes occuring. World-wide, preterm birth occurs on average in roughly one out of ten pregnancies, with a generally higher incidence rate in developing countries [19]. Moreover it has been indicated that the overall prevalence of preterm births is increasing [57].

The causes for premature birth are not completely understood and may be the result of a combination of multiple factors, such as socioeconomic factors,

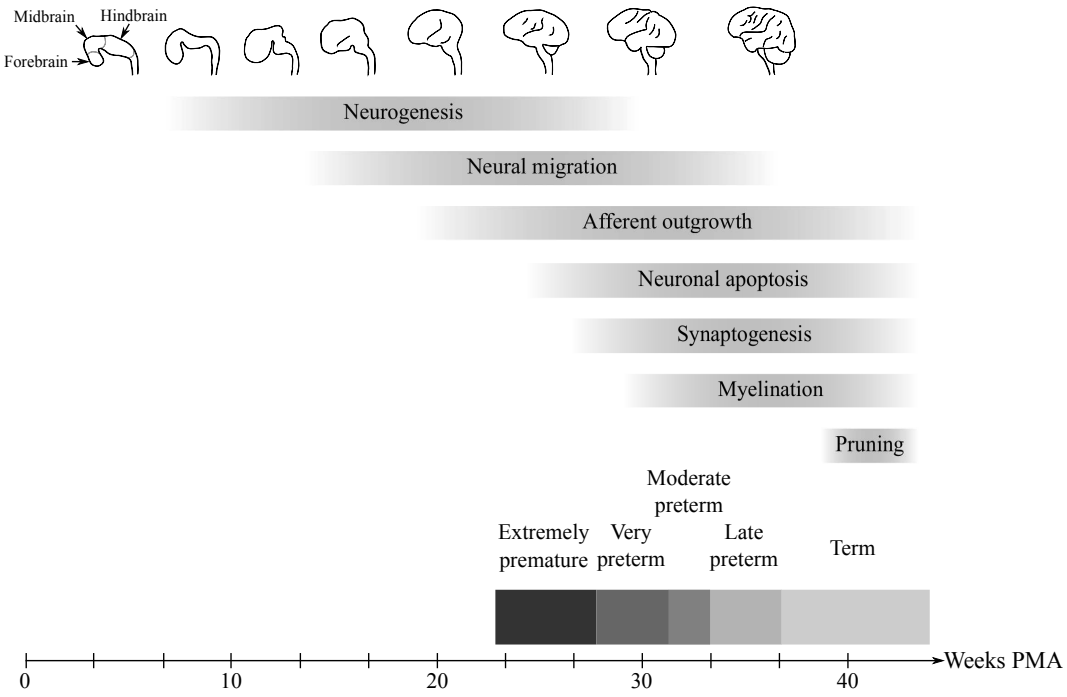

Figure 2.2: Time-line of human brain development in weeks of post-menstrual age (PMA). It illustrates the sequence of neurogenesis, neuronal migration, establishment of structural connections, synaptogenesis and pruning, as well as gyral development.

genetic influences, medical conditions, pregnancy history or due to the use of assisted reproductive technologies to initiate pregnancy [57]. Importantly, there is an increased survival rate of preterm children due to advances in perinatal care [174].

With higher survival rates additional medical care is required, which can result in high physical, psychological and economical costs [19]. In particular it has been indicated that children born prematurely undergo substantially different cortical organisation [78, 79] and are more likely to suffer from neurodevelopmental impairment compared to term born children [40, 57]. Notably, Wood et al. [175] showed that approximately 50% of extremely preterm infants exhibit disabilities at 30 months of age. Clinical disabilities associated with premature birth include motor [94, 95], auditory [94, 125], visual [37, 94] and cognitive impairments [94], where cognitive impairments are more prevalent than motor and sensory impairments [5, 40, 94], as well as mental disorders, such as autism [125] and attention deficit hyperactivity disorder (ADHD) [5]. It should be noted, however, that sensory impairments can lead to secondary problems, including language deficit, as well as impaired social and emotional development [5]. Additionally, behavioural problems such as ADHD may be

associated with lower cognitive score [40] and as such be a confounder in some studies.

2.2 Imaging the Developing Brain

Magnetic resonance imaging (MRI) is widely used for examinations of developing organs in the human body, such as the heart [90], the liver [167], and the brain [70, 82]. The benefit of MRI over other techniques, such as computer tomography (CT) or X-Ray imaging, lies in the fact that MRI does not utilise ionizing radiation and consequently allows for relatively safe and repeatable scans at early stages of life [147].

2.2.1 Magnetic Resonance Imaging

The principle of MRI was originally known as nuclear magnetic resonance and introduced by Rabi et al. in 1938 [116] and further developed by Bloch et al. [26] and Purcell et al. [114] in 1946. Since then significant advances have been made, but the underlying physics remains the same. MRI uses the magnetic moment of non-zero spin nulcei, such as hydrogen (H^1), to generate a detectable signal. Each element's spin direction is usually randomly distributed, however, by using an external magnetic field B_0, introduced by the presence of the magnet of an MRI scanner, the spins align in a preferentially parallel direction at room temperature.

A second magnetic field is applied to the aligned spins, which oscillates at radio frequencies (RF). This RF pulse excites the spins, which rotates them away from their preferred orientation (parallel to B_0). In order to do so, the radio frequency is set to the Larmor frequency which is proportional to the magnetic field strength (see for example [98]). Subsequently the spins start precessing about B_0. The rotation and precession of the spins decay exponentially with tissue specific time constants T_1 and T_2 respectively.

Depending on which type of tissue is of interest, imaging sequences can be optimised to make signals strongly dependent on variations of specific parameters, such as time constants T_1 and/or T_2 (with $T_1 \approx 2.5\ s$ and $T_2 \approx 0.2\ s$ in neonates [173]). In order to do so, two key parameters can be tuned. The first time parameter, related to T_1, is the repetition time (TR), which reflects the time from the application of the first excitation pulse to the application of the next. The other time parameter is called echo time (TE). It refers to the

time between the application of the excitation pulse to the peak of the signal induced in the receiving coil, which relates to the precession decay time T_2.

A final magnetic field may be applied in order to encode spatial information of the signal. This magnetic field is commonly referred to as a gradient, as it is varied according to the spatial location within the MRI scanner. Research on gradient pulse sequences has been conducted in order to improve image quality and reduce imaging time [3, 91, 92, 113, 166]. In particular, by adjusting the gradients one can apply different weighting schemes such as diffusion weighting (see section 2.2.2) or use it for slice selection and image encoding.

When applying gradients, slices can be selected from the volume due to the fact that the precessional frequency of a nuclei in a static magnetic field, the Larmor frequency, is proportional to the magnetic field strength, which varies according to the gradients. That means that it is possible to excite individual slices within the brain by adjusting the RF pulse. By convention the direction of slice selection is denoted by z, whereas the perpendicular xy plane characterises the excited slice.

MR images are acquired in a two dimensional k-space, where k_x and k_y are given by the integrated area of the gradients in the corresponding direction. By manipulating the gradients in x and y, the entire signal of the slice can be collected in k-space and, using Fourier transform, can be mathematically converted into signals in the xy plane. By changing k_x and k_y, the measurement follows a path in k-space. In k-space, measurements around the centre (low values of $k_{x/y}$) correspond to gradual changes in space, i.e. constant or slowly varying areas, whereas high values of $k_{x/y}$ correspond to edges in the resulting image.

Considering this effect of sampling, it is important to define efficient trajectories through k-space. Various trajectories have been proposed. Acquiring k-space line by line, where one shot samples k_x for a single value of k_y and subsequently altering k_y for each shot, is called "phase encoding". This type of sequence is typical for most clinical applications [112]. Instead of acquiring only one k_y value in a single shot, an alternative approach uses an oscillating trajectory, which is consequently able to acquire all of k-space in a single shot [91]. This approach, also known as echo planar imaging (EPI), is much faster than phase encoding. Other sequences have been developed which use, for example, spiral trajectories [2]. Moreover, by using techniques such as compressed sensing and parallel imaging [113, 166], the amount of data required for high quality image reconstruction can be reduced and as a result, the scan

time can be further decreased. One example of these techniques is given by SENSEtivity encoding, which uses the spatial sensitivity information of the receiver coils to reduce scan time [113]. The factor of undersampling can be represented by a SENSE-factor, where, for example, a sense factor of two can be achieved by acquiring only every other line in k-space [113].

This section focuses on reviewing the imaging sequence of EPI, as it is the most common sequence used in diffusion weighted MRI (see section 2.2.2). A typical EPI imaging sequence is shown in Figure 2.3a.

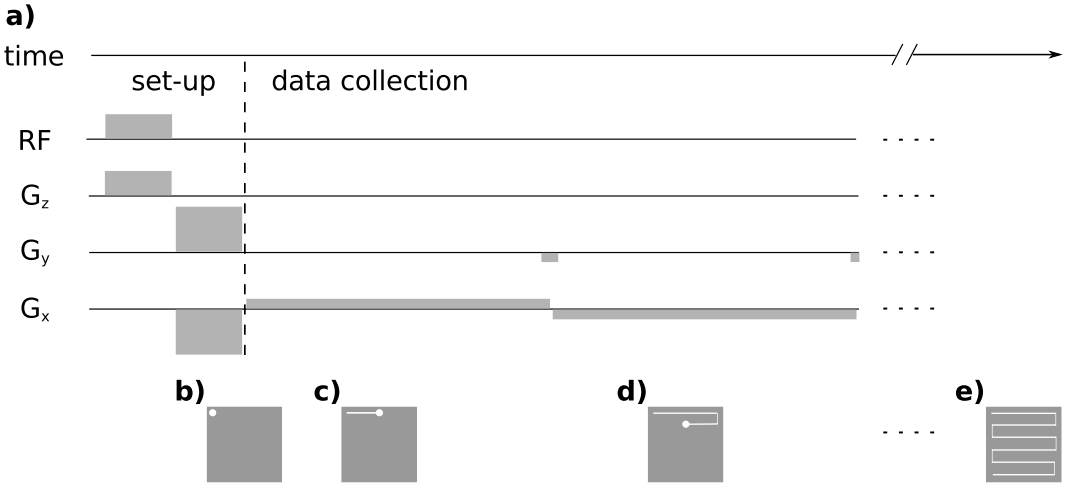

Figure 2.3: Imaging sequence (a) and k-space trajectory (b-e) for echo planar imaging (EPI). In this sequence all of k-space can be imaged in a single shot.

After the initialisation step of the sequence (set-up), which includes excitation (RF), slice selection (G_z) and the initial displacement in k-space (G_y and G_x) to set the starting point of the trajectory (Figure 2.3b), the data collection sequence begins. The non-zero gradient component in G_x moves the acquisition from smaller k_x values to higher k_x values, traversing k-space from left to right in Figure 2.3c. At the maximum value of k_x, a short pulse in G_y moves the trajectory to the next k_y value and with a negative component in G_x, k_x is traversed in opposite direction (Figure 2.3d). This process is repeated until the entire k-space has been probed (Figure 2.3e).

2.2.2 Diffusion Weighted MRI and Tractography

Investigations of structural connectivity within the brain started with the introduction of fibre staining methodology in 1882 [170, 171]. However, fibre staining cannot be done *in-vivo*, necessitating the development of non-invasive techniques to characterise fibre trajectories. With the introduction of diffusion

weighted MRI sequences (dMRI), *in-vivo* imaging of the structural connectivity based on diffusion properties became possible.

The structural connectivity within the brain can be investigated by characterising the diffusion of water molecules along the pathways which connect areas of the brain with each other. In general water molecules within a fluid undergo random displacements (Brownian motion), due to collisions with other water molecules. In case of impermeable boundaries, the motion of a water molecule is restricted. Examples of 2D unrestricted and restricted Brownian motion are shown in Figure 2.4.

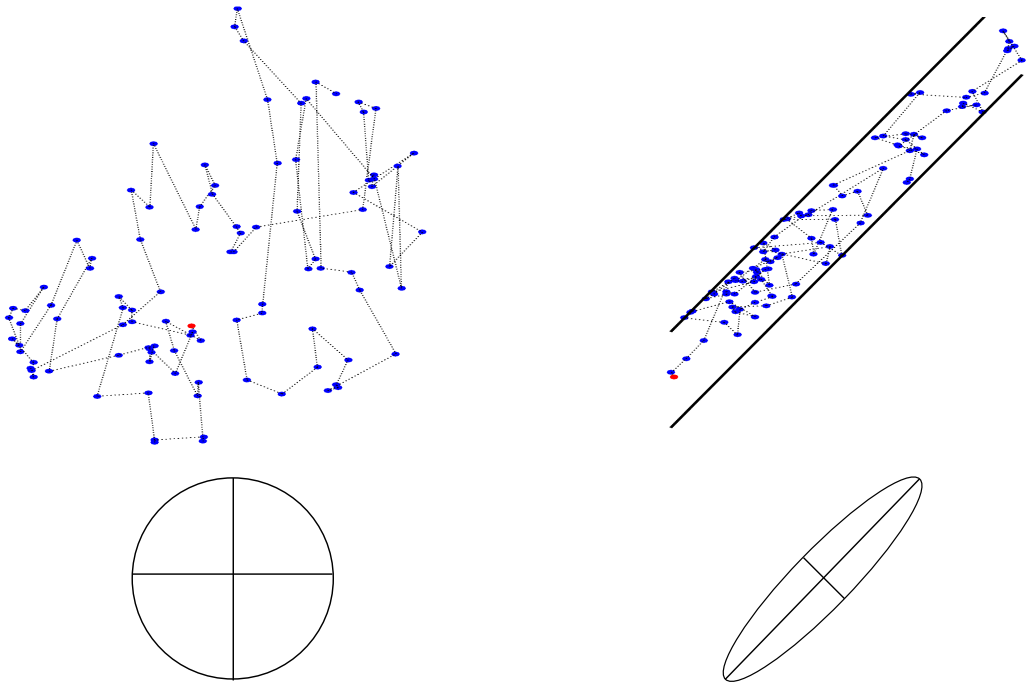

Figure 2.4: Example of unrestricted (top left) and restricted (top right) Brownian motion, with respective 2D representation of the diffusion direction (bottom).

In the brain, it is believed that the 3D movement of water molecules is hindered by the axonal membranes [18]. This means that water molecules undergo a restricted Brownian motion and the extent to which a preferential diffusion direction is present can be described using measurements of anisotropy. The amount of anisotropy has been used to study patients and healthy subjects, where low levels of anisotropy can serve as markers for white matter damage [48, 66]. This is of particular interest, as the level of anisotropy has been shown to correlate with task performance [48].

In order to estimate anisotropy, the MRI pulse sequence needs to be modified to become sensitive to diffusion directions. The principle of adding diffu-

sion weighting to pulse sequences was introduced by Stejskal and Tanner [142], where a bipolar gradient is applied after excitation and before data collection. This gradient successively adds two phases with opposite signs to each spins precession, where the magnitude is dependent on the spin's average position within the body. Assuming that the nucleus/spin does not change its average position between the adding of the two phases, the net effect is zero. This is in general the case for unrestricted Brownian motion, as can be found, for example, in the ventricles. On the other hand, if the motion is restricted, the average position of the nucleus will most likely change in a given time interval and the sum of the two phases can be related to net movement of the nucleus. The modified pulse sequence which incorporates diffusion weighting in one direction is shown in Figure 2.5.

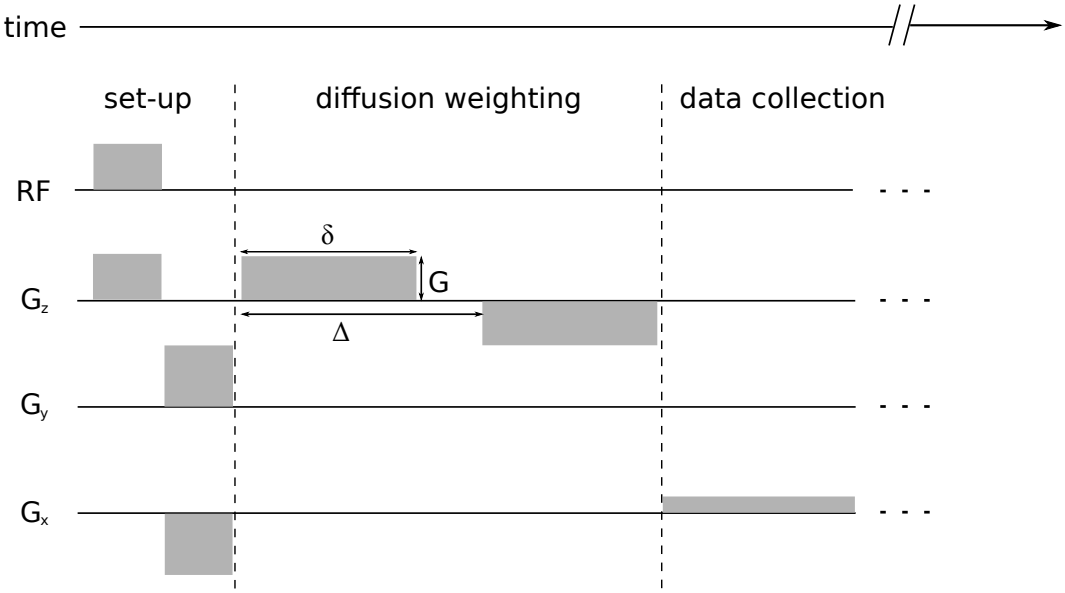

Figure 2.5: Imaging sequence for diffusion weighted imaging in one direction. This sequence can be applied along any direction, i.e. any linear combination of x, y and z.

The correct application of diffusion weighted sequences with appropriate parameters is imperative for image quality [74]. One important parameter which summarises the influence of dMRI sequences is the so called b factor, defined as

$$b = (\gamma \cdot G \cdot \delta)^2 \left(\Delta - \frac{\delta}{3}\right),$$

where γ is the gyromagnetic ratio, G the diffusion weighted gradient's magnitude and Δ and δ the separation and the duration of the applied diffusion weighted gradient, respectively [112, 142] (see Figure 2.5). The optimal value

of the b-factor is problem specific and needs to be guided by the research question at hand, as it involves a trade-off between diffusion information and signal-to-noise ratio [74]. In general, the diffusion sequence is repeatedly applied to acquire a number of volumetric images, each associated with a different non-collinear diffusion direction. The set of all volumetric images subsequently provides a diffusion map including a measure of anisotropy of the imaged brain.

Tractography

With diffusion information available, it is possible to characterise the trajectories of the major pathways in the brain by using tractography, which integrates voxel-wise fibre orientation estimates [20, 80, 102]. Various aspect of the human brain have been investigated using dMRI and tractography, such as asymmetry of white matter structure [135] or to infer structural connectivity for network analysis (see section 3.7). Furthermore it can be used to map the development of structural connectivity non-invasively, for example in the cerebellum [145] and cortex [177], and therefore describe the evolution of the emerging pathways and overall fibre organisation.

As a first step, in order to estimate pathways in the brain using tractography, the diffusion direction needs to be modelled for each voxel. A variety of different compartment models have been proposed [108]. The simplest model represents the direction of diffusion by estimating the diffusion tensor for each voxel, assuming a single compartment model [12]. However, by fitting this diffusion tensor model to a voxel, which may contain extra-axonal and intra-axonal space, i.e. more than one compartment, the resulting directionality information will be a composite of both. This means that the true direction of the white matter pathways may not be detectable, depending on the fitted model [108].

Behrens et al. [22] proposed a model, which assumes a combination of isotropic (extra-axonal space) and anisotropic diffusion in one direction (intra-axonal space). This model is commonly referred to as "ball and stick", as the isotropic diffusion is represented by a sphere ("ball") and the anisotropic diffusion by an cylinder with its principal axis in the direction of highest anisotropy and a radius equal to zero ("stick"). One particular benefit of this approach is that multiple fibre directions, i.e. multiple "sticks", can be estimated within each voxel [23].

Tractography estimates the pathways by using streamlines through the vector field of diffusion directions measured by dMRI. Streamlines can be de-

scribed mathematically as 3-dimensional space-curves [13]. On the other hand, considering that dMRI data are discrete, where diffusion information is averaged across a voxel, streamlines may be represented by a series of connected voxels.

In general one can distinguish between deterministic and probabilistic tractography methods. Deterministic tractography starts from a seed voxel and streamlines are integrated by using the voxel-wise directional diffusion information. In order to do so, a streamline uses the information in its current voxel and takes a "step" in the direction of the primary diffusion direction [20]. The extrapolation of the next point along a streamline can be done in a variety of ways. Mori et al. [102], for example, assumed that each voxel's measurement should be applied over the entire voxel, whereas Lazar and Alexander [80], for example, use a weighted interpolation of the diffusion direction including neighbouring voxel measurements. Regardless of the approach to infer the directionality, the process is repeated until a termination criterion is reached, which can vary depending on the tractography method used [72].

Using deterministic tractography, termination criteria may be defined by a white matter mask, where a streamline is terminated if it leaves the mask, a predefined anisotropy threshold or a curvature threshold. The intuition behind the anisotropy threshold is based on the fact that with lower anisotropy, the next step of a streamline is more uncertain. If the anisotropy in a voxel is below a certain level, subsequent estimation of streamlines may be erroneous and in order to decrease the amount of false positives, the streamline is terminated [20]. Similarly, if the next step of a streamline would involve an abrupt change in direction, unlikely to occur in the anatomy of white matter tracts, a streamline may be terminated, however, it is difficult to justify any given turning angle threshold [16].

A different tractography approach tries to handle uncertainties in voxels for which deterministic tractography would stop, for example, because of low anisotropy [22, 23]. In order to do so, each voxel is assigned a probability density function (pdf) that reflects the uncertainty of fibre orientations. Once a streamline reaches a voxel, the direction of the next step is sampled from the probability distribution of its pdf. This means, however, that the path through a given voxel may not be unique and it becomes necessary to sample multiple streamlines from each starting voxel in order to estimate the spatial pdf of a path connecting a seed point to a target point. Moreover, the confidence in any streamline can be expressed by its compounded probability along the

path [22].

The benefit of this approach, as mentioned above, lies in the possibility of "following" streamlines through voxels of low anisotropy, for example, in the developing brain (see section 2.1). Furthermore probabilistic tractography is more resilient to noise, as errant routes due to a noisy voxel, tend to disperse quickly [20, 22]. Consequently, termination criteria can be very lenient, i.e. no anisotropy and a large curvature threshold. The use of a curvature threshold is mainly to prevent streamlines tracing their steps back and thereby artificially increasing the compounded probability of a path existing [22]. Tracing steps back is generally possible, as the diffusion direction is degenerate with respect to its sign and subsequently cannot distinguish afferent and efferent fibres [13, 72].

2.3 Subject and Imaging Data

This work investigates the development of structural brain connectivity in premature infants. Preterm and healthy term control infants were recruited as part of studies at Queen Charlotte's and Chelsea Hospital. Ethical permission was granted by the Hammersmith and Queen Charlotte's and Chelsea Hospital (QCCH) Research Ethics Committee and written parental consent was obtained for each infant.

Serial dMRI data were acquired for all 28 preterm infants, who were born at less than 32 weeks gestational age (GA). Mean GA at birth was 28.0 ± 2.3 weeks and the mean post-menstrual age at scan (PMA) was 30.8 ± 1.9 and 41.2 ± 1.2 weeks at the first (baseline) and second (follow-up) scans respectively. Table 2.1 summarises the demographic characteristics for all preterm subjects.

A group of fifteen (6 male) healthy term control infants born at 39.3 ± 1.4 weeks GA were also scanned at 42.1 ± 1.7 weeks PMA. All preterm infants at term equivalent age and ten term control infants were sedated ($25 - 50 mg/kg$ oral chloral hydrate) for the scan. At the baseline scan of the preterm cohort, no sedation was administered. During the scan each infant's vital signs, i.e. pulse oximetry, temperature and heart rate, were monitored. Additionally, MRI safe hearing protection was used for each infant (President Putty, Coltene, Whaledent, MiniMuffs, Natus Medical Inc.).

T2-weighted fast-spin echo MRI were acquired on a Philips 3T scanner, using a 8 channel phased array head coil with the following parameters: TR: 8670 ms; TE: 160 ms; flip angle 90°; slice thickness 1 mm; field of view: 220 mm;

Table 2.1: Summary of the demographic information of the preterm cohort.

ID	PMA at scan (weeks)		GA at birth	Weight	Sex
	Baseline	Follow-up	(weeks)	(g)	
P1	29	42	24.43	770	m
P2	25.29	42	24.86	800	–
P3	29	41.86	25.29	800	f
P4	30.14	42	25.57	800	–
P5	28.29	40.71	26	750	f
P6	29.71	41.71	26.14	950	f
P7	27.71	43.29	26.14	810	f
P8	28.14	40.71	26.29	895	m
P9	31.29	39.41	26.43	980	f
P10	32	40.43	26.57	1020	–
P11	31.86	38.86	26.57	955	f
P12	31.14	40.57	26.71	1010	f
P13	31.14	40.57	26.71	930	f
P14	29.86	42.56	26.86	–	m
P15	30	42.43	27.71	900	f
P16	31.14	42.71	28.29	1010	f
P17	31.56	43.14	28.86	–	–
P18	32.56	41.14	29.14	970	f
P19	30.71	43	29.14	1170	f
P20	30.71	39.56	29.43	980	m
P21	33	40.29	30	1740	m
P22	33	41.29	30	1690	–
P23	33	42	30.43	1440	m
P24	32.86	40.71	30.86	1390	m
P25	31.57	39.57	31	1330	m
P26	32.29	41.29	31.29	2020	m
P27	32.71	40.56	31.86	1530	f
P28	32.71	40.56	31.86	1400	m

matrix: 256×256 (voxel size: $0.86 \times 0.86 \times 1\,\text{mm}$).

BET [134] was used to skull strip the T2 brain images. Subsequently, N4 inhomogeneity correction was performed [150] to eliminate intensity inhomogeneity. The corrected images were then aligned with non-rigid registration [123, 129] to age-specific template priors [130]. Age-appropriate tissue probability maps were transformed from template space to the individual T2 images. This allowed the extraction of grey and white matter masks for each infant, which were used in remainder of this work.

32-direction dMRI data were successfully acquired for each infant and each time point. Single shot echo planar imaging dMRI data were acquired in the transverse plane in 32 directions using the following parameters: TR: 8000 msec; TE: 49 msec; slice thickness: 2 mm; field-of-view: 224 mm; matrix: 128×128 (voxel size: $1.75 \times 1.75 \times 2\,\text{mm}$); b-value: $750\,\text{sec/mm}^2$; SENSE factor of 2. A reference volume was also acquired (b-value: $0\,\text{sec/mm}^2$).

Motion artefacts were visually assessed for each gradient volume and affected volumes were removed before preprocessing. Consequently, 17 of 28 subjects of the premature cohort had at least one gradient removed (maximum: 4, mean: 2.35) in their baseline scan. No artefacts were found at term-equivalent age or in the term-born control group. All diffusion volumes were aligned to the reference volume and motion correction was performed. Corresponding b-vectors were then rotated accordingly. Diffusion data were registered to the T2 space and BedpostX [20] (two fibre population) was applied to each subject's diffusion data, which allowed the use of ProbtrackX [23, 119], a probabilistic tractography algorithm, in later chapters.

Chapter 3

Network Analysis

Network theory is a growing area of interest in modern science and has found applications in diverse areas, such as social interactions [43], economics [64], flavours in recipes [3] and gene-disease relations [56]. In particular through the small world phenomenon, sometimes conveyed through the expression "six degrees of separation", network theory was popularised. The small world phenomenon, studied in the famous experiment by Travers and Milgram in 1969, shows that a message to an unacquainted person, by relaying it through the social network from the sender to the receiver, will only take a small number of "hops" to reach its destination [149]. This experiment was repeated more recently by Dodds, Muhamad and Watts with similar results [43].

But what exactly is a network? David and Kleinberg describe it in the most basic sense as a "collection of objects in which some pairs of these objects are connected by links" [45]. The collection of objects may represent, for example, human beings, products, ingredients, diseases or brain regions, whereas the links are relationships or structural connections. Figure 3.1 shows a simple representation of a network, which can also be called a 'graph'.

The objects in a network are called nodes. In Figure 3.1 they are shown as red circles labelled with the letters a-f. The edges are represented as black lines. In general, edges can also encode a weight and a direction of a connection. In the case of a social network, the weight may represent the strength of a friendship, meaning a connection is stronger if two people are better acquainted. In this application of graph theory the graph may also be directed. Two people, though considering each other as friends, might see the strength of the friendship differently. Another example can be drawn from the U.S.

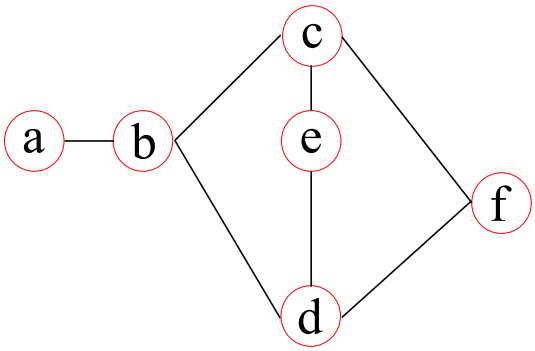

Figure 3.1: Representation of a general undirected graph with six nodes (circles) and seven edges (lines).

airport network, where the individual nodes may represent airports and edges the existence of flights between two airports. The weight of these edges can subsequently be defined, for example, as the number of seats per day available on the flights connecting different airports [107]. Figure 3.2 shows one possible weighted and directed representation of the graph seen in Figure 3.1.

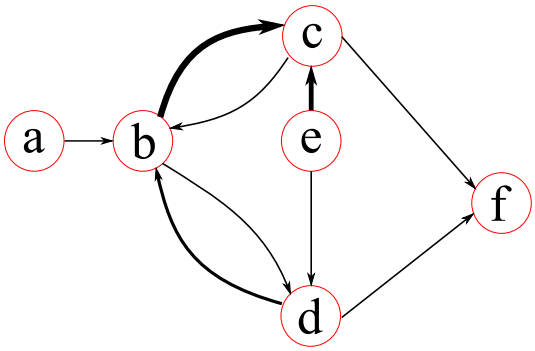

Figure 3.2: Representation of a general directed and weighted graph with six nodes. The weight is represented by the thickness of the connection, while the direction is represented by arrows.

In this work, a graph is denoted by $G = \{V, E, W\}$, where V is the set of vertices/nodes, E is the set of edges and W the set of assigned weights. Additionally, an edge between two nodes $i, j \in V$ is denoted by $ij \in E$ and $w_{ij} \in W$ represents the corresponding edge weight. The weight matrix W represents the connectivity matrix, which is usually derived from data. A matrix A, with $a_{ij} = 1$, if $ij \in E$ and 0 otherwise, is called an adjacency matrix. The neighbourhood N_i of node i is given by the set of its edge-wise neighbours $\{j \in V : j \neq i, ij \in E\}$ and it is assumed that graphs are simple, i.e. that they have no multiple edges or self-loops.

In general a graph can be either binary and undirected (bu), binary and

directed (*bd*), weighted and undirected (*wu*) or weighted and directed (*wd*). Real-world networks often fall into the category of *wd* graphs. However, under certain circumstances *wd* graphs may be converted to another category [121], thereby simplifying the problem.

The rest of this chapter will introduce the basic terminology for networks, as well as some underlying principles. An introduction to these concepts can also be found in [103]. In the following the most commonly investigated network measures, organisational principles associated with network structures and random graph models are discussed (sections 3.1– 3.6). In addition, the contributions of network theory to neuroscientific investigations are outlined in section 3.7.

3.1 Degree

The degree of the individual nodes is a simple but important measure on graphs. In a directed graph, one can divide the degree into in- and out-degree. The in-degree k_{in} of a node is the number of links with direction towards the node, whereas the out-degree k_{out} of a node is the number of links leaving the node. Figure 3.3 shows a representation of a node in a directed network and the distinction between in- and out-degree.

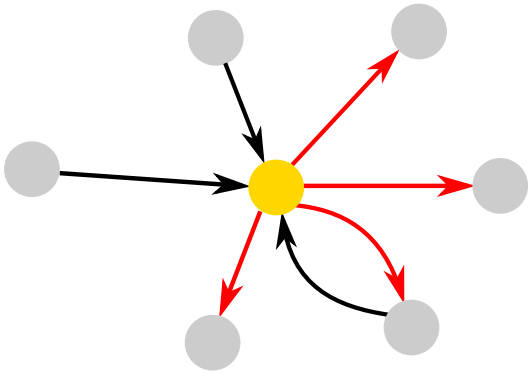

Figure 3.3: Distinction between in and out-degree. The image represents the in- (black) and outgoing (red) edges of a node s (gold).The in- and out-degree of s is $k_{in}(s) = 3$ and $k_{out}(s) = 4$, respectively.

In case of *wu* and *bu*, links are bi-directional. Therefore the in- and out-degree of a node become a single degree measure, $k(s)$, and the adjacency and weight matrices become symmetric. In case of the binarised graphs the degree represents the count of links, whereas in weighted graphs the degree may be defined as the sum over the weights of the corresponding links. The average

degree, where the average is taken over all nodes in the network, can serve as a summary measure for the network investigated.

3.2 Distance

Some network measures require the calculation of shortest paths between sets of nodes. Calculating all pairwise shortest distances efficiently is a well known problem in graph theory. One of the most commonly used algorithms to calculate pairwise distances between nodes in a weighted graph was developed by Dijkstra in 1959 [42]. A description of the algorithm can be found in [103]. The Dijkstra algorithm takes initial distance values for each edge $ij \in E$ of a given graph $G = \{V, E, W\}$ as input. These distances may be problem specific distances, as they can be found, for example, in transport networks, where distances represent physical distances such as road length, or flight distances. In other areas the weight of edges may not be related to physical distances, necessitating a method for converting edge weights into distances. Areas where this may apply are, for example, friendship or brain networks. Two nodes, meaning two friends or two brain areas respectively, may be considered "closer", if the edge connecting the two nodes has a higher weight compared to others in the network. The intuition behind this is that if a connection between nodes i and j is strong, information will take less time to travel along ij and the topological distance will be shorter. In this case a mapping from strength to distance is required, which maps high edge weights to small distances. Distances within a graph may be set, for example, to the reciprocal connection strength [121].

3.3 Network Measures

In terms of network analysis, there are two intrinsic levels at which measures can be compared [99]. Local metrics within a graph represent measures which are either associated with individual nodes or with pairs of nodes, whereas global metrics characterise the entire network as a whole. A summary of network measures commonly used to characterise brain networks is given by Rubinov and Sporns [121]. This section describes the network measures which are used in the following chapters.

3.3.1 Clustering Coefficient

The clustering coefficient is one of the most important network metrics that has been used in a wide range of studies and was first introduced by Watts and Strogatz in the context of small world networks [169] (see section 3.4). It can be seen as the probability that neighbours of a node $i \in V$ are also neighbours of each other. In a friendship network it can therefore be interpreted as a measure of how many friends of a person's friends are also friends themselves and thus measures the extent of how cliquish friendship circles are.

The clustering coefficient $C(s)$ of a node s represents the ratio of triangles containing s to the maximum number possible [50] and is given by

$$C(s) = \frac{2\, t_s}{k(s)\,(k(s)-1)}, \tag{3.1}$$

where t_s is the number of triangles around node s and $k(s)$ is its degree. If a node has less than 2 neighbours, it's clustering coefficient is set to 0. The clustering coefficient C of a network can then be calculated as the average of $C(s)$ over all nodes s. It can be interpreted as the predominance of clustered components around nodes.

Figure 3.4 shows the clustering coefficients of nodes in a small network. Only when the neighbourhood of a node is fully connected will the clustering coefficient be equal to one. This contrasts with the network in Figure 3.1, in which all nodes have a clustering coefficient of zero.

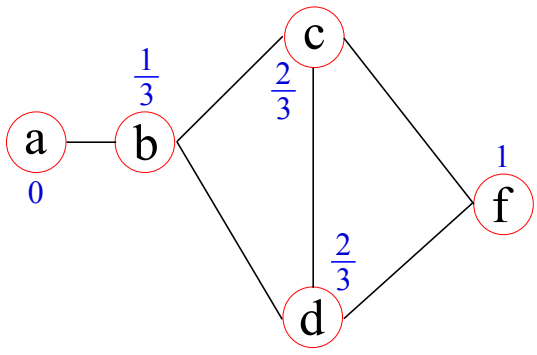

Figure 3.4: Sample graph with corresponding clustering coefficients of each node given in blue. Node f has the highest clustering coefficient, as its neighbourhood is fully connected. In contrast, for nodes c and d, there is one connection among their neighbours missing ($bf \notin E$), resulting in a reduced coefficient. For node a the clustering coefficient is zero by definition.

3.3.2 Transitivity

A common criticism of the average clustering coefficient is that it places more weight on nodes with low degree, compared to high degree nodes. Therefore it has been argued that the average of the clustering coefficient, as suggested by Watts and Strogatz [169], might not be representative of the amount of closed triangles in a network due to the dominance of the low degree nodes. This issue is illustrated in Figure 3.5.

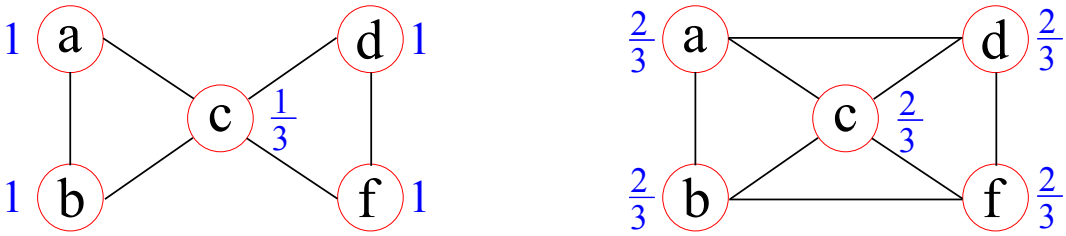

Figure 3.5: Graph to illustrate a shortcoming of using the average clustering coefficient to represent a network. The average clustering coefficient is 0.87 and 0.67 for the graph on the left and right respectively. This example shows that the average clustering coefficient of the network can be reduced by closing additional triangles in the graph.

An alternative definition of a global clustering coefficient which eliminates this bias, usually referred to as transitivity is given by [106]

$$T = \frac{\sum_{s \in V} 2\, t_s}{\sum_{s \in V} k(s)\,(k(s)-1)}. \tag{3.2}$$

In contrast to the average clustering coefficient, where each nodal clustering coefficient is normalised individually and then averaged, the transitivity of a network is normalised collectively, i.e. that the total number of closed triangles is normalised by the total number of closed and open triangles in the network. Transitivity therefore reflects the ratio of closed triangles in the network to the total number of closed triangles possible. When comparing the graphs shown in Figure 3.5 the average clustering coefficients/transitivity are given by 0.87/0.60 and 0.67/0.67 for the left and right graph respectively, which means that transitivity can accurately reflect the closing of additional triangles in the network. Both measures are widely used in the literature, however, one needs to be aware of the difference in their meaning.

3.3.3 Modularity

Modularity tries to determine how well a network can be separated into individual modules or communities. In a graph with two modules labelled ± 1, modularity can be calculated by [104]

$$Q = \frac{1}{4m}\mathbf{s}^T\mathbf{B}\mathbf{s}, \tag{3.3}$$

where s_i is the module label to which node i belongs and $\mathbf{B}$ the so called modularity matrix. $\mathbf{B}$ is defined as

$$B_{ij} = A_{ij} - \frac{k(i)k(j)}{\sum_{i \in V} k(i)}, \tag{3.4}$$

which represents the number of edges between nodes i and j minus the expected number of edges, if all edges in the graph were randomly distributed. Commonly networks contain more than two modules, and subsequently this approach is recursively repeated for each subnetwork defined by a module, where the incremental modularity for the subnetwork is estimated. When Q is maximised, the algorithm stops. In general modularity Q is estimated for non-overlapping modules [38]. Figure 3.6 shows an example graph and its partition into two modules.

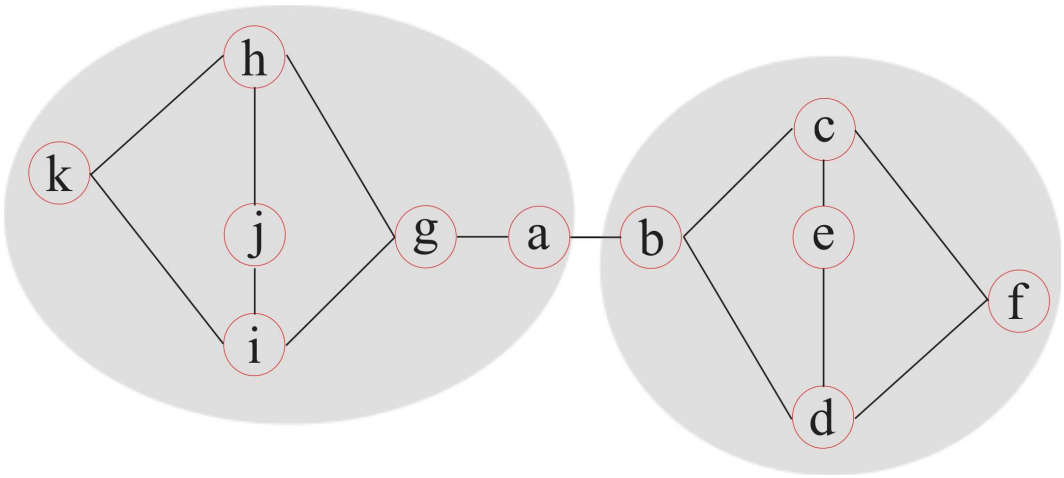

Figure 3.6: Sample graph which illustrates the definition of modules in a network.

It should be noted that the definition of modules is not always unique. Node a in the example in Figure 3.6 can be assigned to either module without altering the value of Q.

3.3.4 Characteristic Path Length

The characteristic path-length, $\lambda(s)$, of a node s is defined as average shortest path-length between s and all other nodes in the network. It can be interpreted as a measure of integration of a particular node in the network and is given by

$$\lambda(s) = \frac{1}{|V| - 1} \sum_{t \neq s} d_{st}, \tag{3.5}$$

where d_{st} is the shortest distance between nodes $s, t \in V$ and $|V|$ is the total number of nodes. The mean measure, λ, taken over all nodes s, is referred to as global characteristic path-length.

3.3.5 Efficiency

The efficiency $E(s)$ of node s is computed similarly to the characteristic path-length. In this case, however, the average is taken over the reciprocals of the shortest paths. The advantage of efficiency over characteristic path-length lies in the meaningful computation for multi-component networks, as infinite paths between nodes in disconnected components have zero efficiency. The overall efficiency of a network can be expressed by the mean of $E(s)$ over all nodes s, where $E(s)$ is given by

$$E(s) = \frac{1}{|V| - 1} \sum_{t \neq s} d_{st}^{-1}. \tag{3.6}$$

3.3.6 Eccentricity and Diameter

The eccentricity of a given node is defined as the longest of all the shortest paths connecting it to the remaining nodes in the network. The diameter of a network is given by the maximum shortest path distance within the network, or the maximum of all per node eccentricity measures, and is representative of the size of the network. In case of information flow, assuming a constant transmission speed, a global eccentricity measure, given by the average of all nodal eccentricity values, can therefore represent the average time it takes for information to spread from one node to the remainder of the network. Subsequently, the diameter is representative of an upper bound for the time it may take for information to reach any node from any other node. Both measures are calculated based on extreme values within the network structure and are therefore susceptible to outliers or small perturbations.

3.3.7 Betweenness Centrality

Betweenness centrality provides a measure of a node's importance by counting how many of all shortest paths, not starting or ending at that particular node, pass through the node. A node s in a graph has $BC(s)$ given by

$$BC(s) = \frac{1}{(|V|-1)(|V|-2)} \sum_{r,t:r\neq s\neq t} \frac{\kappa_{rt}(s)}{\kappa_{rt}}, \tag{3.7}$$

where κ_{rt} is the number of shortest paths from r to t and $\kappa_{rt}(s)$ is the number that pass through s. The betweenness centrality of the network can be characterised by the mean of $BC(s)$ over all nodes. In case of multiple (n) shortest paths having equal length, a fraction $(1/n)$ will be assigned to each node for each of the multiple paths passing through the node. The principle of betweenness centrality was first published by Freeman in 1977 [54]. For a recent analysis including the computational costs, see for example [77].

In a network with a flow of information or messages from node to node along its edges, betweenness centrality is a measure which relates to the amount of information passing through a certain node, assuming that information travels along the shortest paths. In contrast to centrality measures like degree, betweenness centrality considers the load of a node, instead of how well it is connected, and therefore represents a measure of importance with respect to network functionality. Consequently, a node with just two connections might have a high betweenness centrality in a network, for example, if it connects two communities of the network (see Figure 3.7).

3.4 Small-World Networks

Almost three decades after Travers and Milgram identified the small-world phenomenon [149], Watts and Strogatz described the underlying principles of small-world networks [169]. A network which exhibits the small world property lies between completely random and completely ordered (lattice) networks. In a completely random network the existence of an edge may be independent of the nodal properties. An approach for generating such networks is described in section 3.6.1. The lattice network on the other hand only connects nodes that are considered close with each other. One can achieve such a network by, for example, arranging nodes in a circle and adding edges between the neighbours along its circumference.

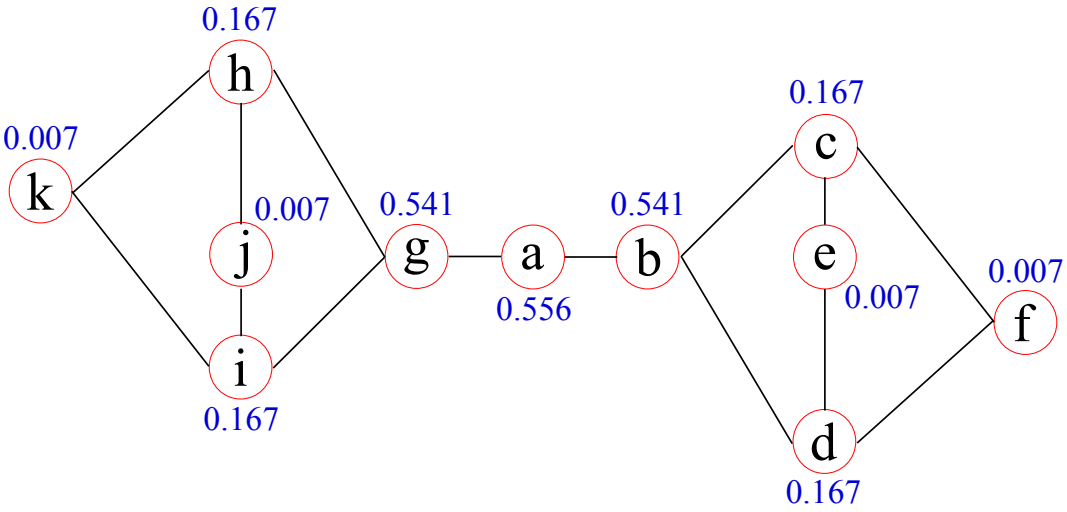

Figure 3.7: Sample graph with corresponding betweenness centrality values of each node. Node a has the highest betweenness centrality value, as it is the node that connects the two communities. If node a were eliminated, the network structure would break down into two smaller networks.

Small world networks share properties of both random and ordered networks. They generally exhibit large local clustering like the lattice network, combined with short path lengths found in random graphs. One way of generating networks with small world characteristics is by starting out from the lattice network and rewiring local connections (edges connecting a node to its neighbourhood) to form long-range connections (edges among nodes that are not part of the same neighbourhood), in order to create short-cuts. Watts and Strogatz [169] showed that the small world phenomenon already emerges after rewiring only a small fraction of the edges and over the years it has been shown that many real-world networks, for example those found in the brain (see section 3.7), exhibit a small-world structure.

One of the attributes which make small-world networks an attractive network model is their efficiency. Information transport can proceed very rapidly, due to the short path lengths and the high clustering. Additionally this network structure allows for a cost-efficient way of creating a network, allowing large networks to keep up a high processing speed, with orders of magnitude fewer edges [169]. Two ways to characterise the small-worldness of a network is either to individually look at the clustering coefficient, characteristic path length and efficiency (compared to random networks), or by using the small world coefficient σ, introduced by Humphries and Gurney [67]. The small-world coefficient is given by

$$\sigma = \frac{C_{norm}}{\lambda_{norm}}, \tag{3.8}$$

where C_{norm} and λ_{norm} are the observed network measures normalised by values taken from random realisations of the network.

3.5 Rich-Club Organisation

Another organisational principle focuses on the subnetwork consisting of nodes with a large percentage of connections within the network (hubs), which are densely inter-connected [180]. This subnetwork is "rich" in edges and is subsequently termed rich-club. In general the rich-club can be seen as a highly interconnected set of nodes which forms a backbone of the network structure [162] and its network-theoretical importance was shown with respect to nodal specialisation, functional integration and resilience to attacks [35, 36, 97]. In order to determine the rich-club members in a given graph $G(V, E, W)$, first nodes are ranked according to some nodal richness coefficient r, which is usually set to the nodal degree (weighted or unweighted). Subsequently a subnetwork $G_{r_0}(V_{r>r_0}, E_{r_0}, W_{r_0})$ is defined containing all nodes in the original graph with a richness parameter greater than a given value r_0, where E_{r_0} is the remainder of the edges E connecting all nodes $V_{r>r_0}$ with weights W_{r_0}. In a next step, a rich-club parameter is estimated, which is defined as the sum over W_{r_0}, divided by the sum over the $\|E_{r_0}\|$ highest weights in the original graph, where $\|E_{r_0}\|$ defines the number of edges in E_{r_0} [107]. In unweighted graphs on the other hand, the rich-club parameter is equivalent to the edge density, i.e. the number of existing edges divided by the maximum possible number of edges in the subnetwork G_{r_0} [180]. This process is repeated for all possible values of r_0 and the set of all rich-club parameters should then be compared to those of randomised versions of the observed networks [35], which can be generated, for example, as described in the following section. A simple example of rich-club organisation is shown in Figure 3.8.

After defining the rich-club within a network, edges can be categorised depending on the connectivity profile [162]. In Figure 3.8 rich-club edges are shown in gold. Edges that connect a non-rich-club member to a rich-club node are defined as 'feeder' (red), which feed information to the rich-club. All other edges are 'local'. Similarly nodes may be classified as rich-club (gold), feeder (red) and local (black) nodes.

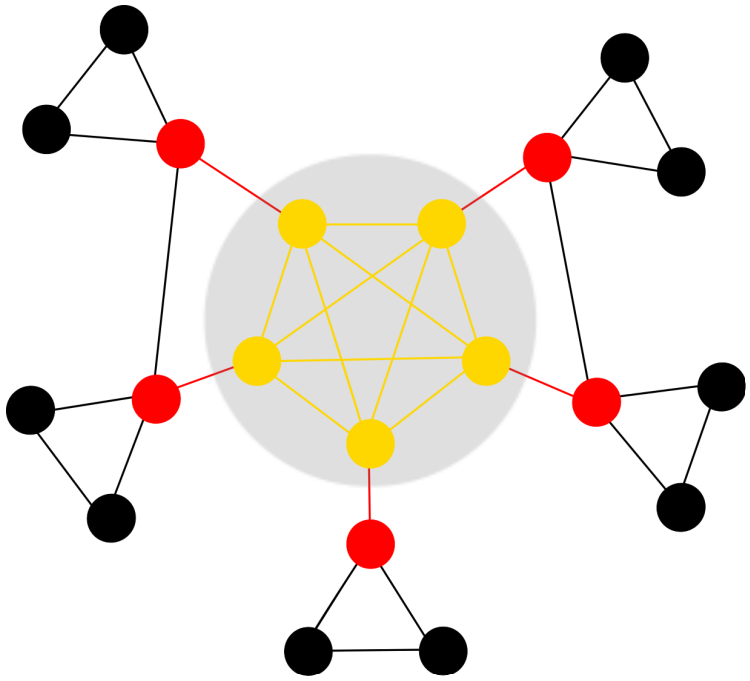

Figure 3.8: Sample graph with rich-club organisation. The set of the central nodes (grey circle) form a rich-club, as they are densely inter-connected. Nodes can subsequently be categorised as rich-club (gold), feeder (red) and local (black) nodes.

3.6 Random Networks

Generating random graphs can be very useful for analysing network structures. They allow for a simple representation of complex networks which helps to analyse properties and dynamics of networks in general. In particular, when analysing complex networks, it is important to assess if the observed quantities are just random, or if there is some underlying process which shapes these measures. Random realisations of networks may therefore provide data for null hypotheses, for example whether a measure is simply random, and allows to estimate the significance of a measure in the observed networks. Additionally, one may use network measures on a random realisation of a network as means of normalising the observed network measure. This enables a meaningful comparisons across networks on an intra- and inter-subject level (see chapter 4).

There are many methods for generating random surrogate networks from a graph. The first binary random graph model was presented by Erdös-Rényi in 1959 [47] and will be discussed in more detail in section 3.6.1. Other models have been proposed in order to recreate some aspects of observed networks,

such as degree distribution [96] (see section 3.6.2) or the small-world property as described in section 3.4. Another set of random graphs based on the recreation of properties of an observed network are called exponential random graph models (ERGM). The user can define specific graph parameters, such as the network measures described in section 3.3, and ERGM draw graphs randomly from the distribution of all graphs which share these parameters (see [133] for an application of ERGMs in relation to brain networks). These methods describe static network models, i.e. the number of nodes (and edges) are predefined and do not allow an easy incorporation of new nodes based on growth. However, Barabàsi et al. [9] noted that real world networks incorporate new nodes over time and created a network model based on evolutionary changes over time. In their model, also referred to as preferential attachment model, a new node n_n is introduced to the network and connected to an existing node n_e based on a probability which is related to the degree of n_e. One example of such a network can be found when investigating citation networks for scientific publications [9].

This section will focus on reviewing the basic properties of the Erdös-Rényi model (ER) and the pairwise switching algorithm (PS), due to the simplicity and historical significance of the former [103] and, according to Rubinov and Sporns [122], the prevalence in the literature of the latter.

3.6.1 Erdös-Rényi

An ER random graph relies on the assumption that the existence of an edge is independent of all node and edge properties. It can be generated, for example, by specifying the total number of edges and then adding edges at random, until the target number is reached. An alternative definition of ER graphs relates to a probability p of an edge existing in a graph of n nodes. In this definition, however, it is difficult to fix the total number of edges and subsequently the density in the network. For this reason the former model will be referred to as ER graph for the remainder of this work.

A basic property of the ER graph is the binomial degree distribution, which represents the probability distribution of the nodal degree for each node over the entire network. Unfortunately, unlike real-world networks, the ER model does not generate hubs, where a few nodes have many more edges than the average in the graph, due to the uniform probability of the edge assignment. Another interesting property of the ER model is the emergence of a giant component. When the average number of edges per node of the graph reaches one,

a very large portion of the graph will be connected creating the so-called giant component. In particular, with respect to information (or disease) transfer, the giant component allows for an extensive spread.

3.6.2 Pairwise Switching

The generation of random realisations of a graph is often carried out while aiming to preserve some of its network properties. In particular pairwise switching of the edges generates random graphs while keeping the unweighted degree of the nodes constant, thereby preserving aspects of the underlying graph structure [96, 117].

For pairwise switching, nodes r and s are picked randomly from V and nodes t and u are chosen randomly from the neighbourhoods N_r and N_s respectively. The edges rt and su are removed from E and ru and st are added if the graph remains simple, i.e. fully connected without multiple edges between any pair of nodes and without self-loops. For weighted graphs, it is possible to switch the weights together with the edges [121]. In this case, although the weighted degree distribution is not preserved, the average weighted degree and the number of edges connected to each node remain constant. The principle of pairwise switching is shown in Figure 3.9.

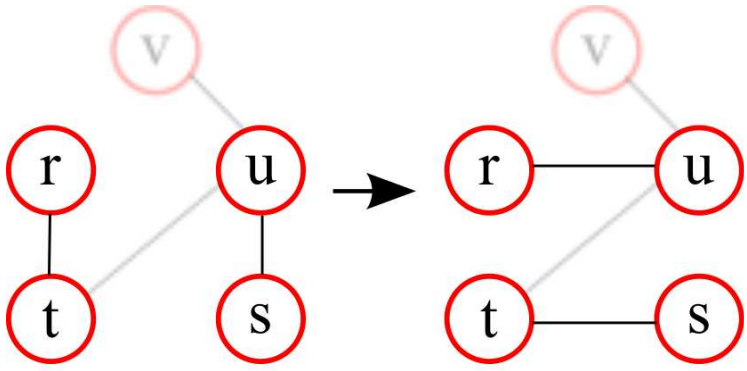

Figure 3.9: General principle of pairwise switching for generating random realisations of a given network.

3.7 Network Analysis in Brains

There has been a rapid expansion in applications of network theory to a variety of scientific fields, enabling simple representations and analyses of complex

systems. Viewing the human brain as a network, i.e. as regions/nodes connected by structural pathways, originated at the end of the 19th century [172] (for a recent review see for example [33]). However, neuroimaging applications of network and graph theoretical techniques are comparatively recent (for an overview see [138]). The nodes of a graph or network can represent brain structures across a range of levels, from synapses to entire brain regions [21]. Once brain nodes are defined, the edge structure or connectivity between them can model structural connectivity (axonal fibres or fibre-bundles) or functional connectivity (based on statistical or causal associations among functional signals) [141].

Network theoretic analyses of brain imaging data increased after it was shown that the brain exhibits small-world characteristics, combining local segregation with global integration [15]. Further organisational principles have since been characterised and analysed, such as rich-club organisation [8, 36, 163] and differences in hub organisation between species [86]. It has also been proposed that network-based analyses may be used to reveal biomarkers for neurodevelopmental and neurodegenerative diseases [62, 87, 165, 168]. In this part, the challenge of defining nodal scales and edge weights in the human brain are discussed, followed by a review of the literature describing brain topology, the application of network measures to determining disease states, the evolution of network metrics in the developing brain, as well as multi-scale analyses in brain networks.

3.7.1 Nodal Scales

One of the challenges when applying network theory to brain image data is the definition of nodes. Over the past few decades a variety of macroscopic definitions of regions of interest were developed based on anatomical landmarks and functional coherence (atlases such as Automated Anatomical Labeling [155]) or stochastic approaches that define regions based on criteria such as equal region size [7, 59, 154].

The developing brain however is particularly challenging with respect to a definition based on atlases due to developmental processes such as myelination and cortical folding [93], as described in section 2.1. Subsequently, some pipelines developed to parcellate the adult human brain, such as Freesurfer, may not work in the neonatal brain [58]. The following section reviews atlases and random parcellation schemes with a focus on Poisson disk sampling.

Atlases

In general, a brain atlas is a map of the human brain which divides it into regions of interest. The most prominent was defined by Brodmann in 1909 [28], which divides the brain into about 50 regions based on their cytoarchitecture. Studying cytoarchitecture is traditionally an invasive process, however, current research on identifying cytoarchitectonic units within the brain using MRI is being conducted [120]. These analyses, though allowing for in-vivo examination, are limited by the spatial and temporal resolution of MRI sequences [120] and therefore the inference of cytoarchitecture remains a challenge, especially in very young subjects.

Another approach to define regions of interest in the brain is by using its functional activation, which may be measured using functional MRI. One atlas which is based on functional activation patterns was introduced by Tzourio-Mazoyer et al. in 2002 [155]. In their work, they defined an Automated Anatomical Labeling (AAL) approach to delineate 45 functionally coherent regions of interest (ROIs) in each hemisphere using the underlying sulcation patterns of the brain.

Various studies have used anatomical templates such as the AAL atlas to investigate brain networks in typical and atypical development [17, 41, 52, 178]. However, most brain atlases are defined for adults and thus the mapping of the considerable changes in the developing brain is problematic. Manually segmenting MR images can be time consuming and lead to inter- and intra-observer variability, which motivated the development of neonatal brain atlases (see e.g. [89, 105]). However, there is a lack of consensus on which parcellation scheme should be used [153].

Random Parcellations: Poisson disk sampling

The biological changes of the developing brain furthermore raises the fundamental question of whether the relative size and position of the regions in the developing brain are equivalent to those defined on the adult brain [153]. Additionally, due to the incomplete sulcation in the developing brain (see section 2.1), the difficulties in registration poses a limitation on using atlas based segmentations in developmental studies [153]. These challenges and the before mentioned lack of consensus on which parcellation scheme to use, motivates the application of random parcellation schemes such as Poisson disk sampling. Poisson disk sampling defines regions based on a distance threshold between region centres and can be applied to any surface or volume [27]. The princi-

ple for generating Poisson disk sampled regions in two dimensions is shown in Figure 3.10.

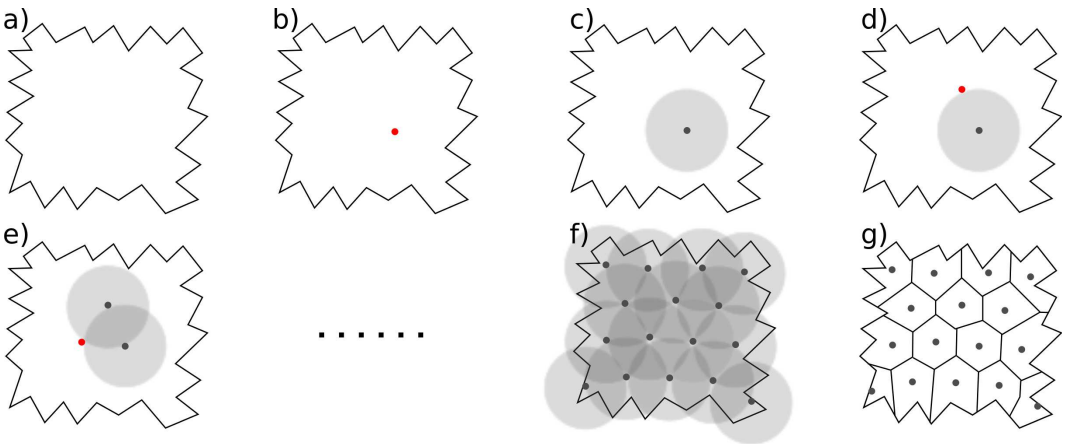

Figure 3.10: Principle of Poisson disk sampling in two dimensions. The surface (a) is divided into approximately equal sized regions (g) by randomly picking a first region centre (b). Subsequent region centres are placed with the condition that they cannot be closer than a minimum distance (indicated by grey circles) from all previously placed region centres (c-f). After all region centres are placed all points of the surface are assigned to their closest region centre, resulting in a random parcellation of the given surface (g).

In the brain, Poisson disk sampling can be applied to the grey matter structures. All grey matter voxels are stored in a list and initially considered as possible region centres. First a distance threshold r_{min} is defined and an initial region centre c_1 is randomly selected from the set of all grey matter voxels. Each voxel i with a distance $d^i_{c_1} < r_{min}$ to c_1 is removed from the list of possible region centres. The next region centre is then randomly selected from the set of voxels $\{j\}$ with $r_{min} < d^j_{c_1} < 2\, r_{min}$. This process is repeated until there are no voxels in the list of possible region centres remaining. Subsequently, each voxel in the grey matter structure is assigned to its closest region centre, resulting in a random parcellation of the grey matter volume into approximately equal sized regions. The framework is illustrated in Figure 3.11.

One benefit of this parcellation scheme lies in the fact that it does not rely on anatomical features or landmarks and can thus be easily applied to neonatal grey matter structures, where the sulcation is incomplete and landmarks are difficult to determine. However, with Poisson disk sampling, the resulting number of nodes may vary due to the random nature of the approach. Figure 3.12 shows a histogram of the number of region variation for $N = 100$ repetitions of a single grey matter mask parcellated with a target number of 500 regions.

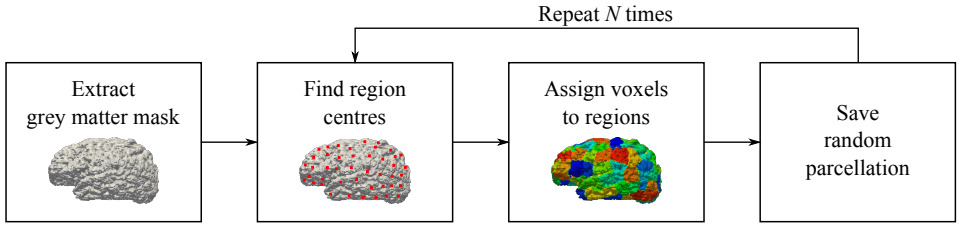

Figure 3.11: Framework of applying Poisson disk sampling to the grey matter structures of the human brain. The process of generating random parcellations is repeated N times.

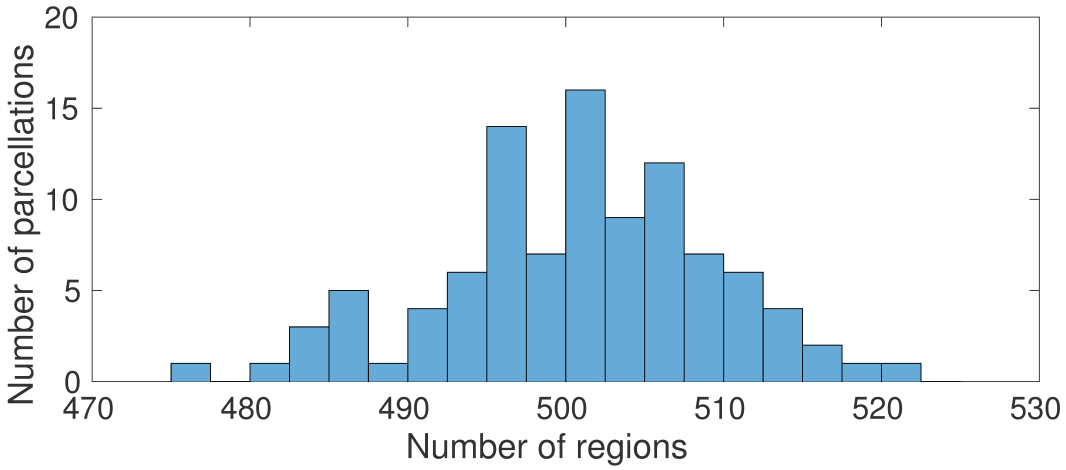

Figure 3.12: Histogram of Poisson disk sampling, repeated 100 times on the same grey matter mask with a target number of 500 regions. This shows the variation in the total number of regions.

Other random parcellation methods have been proposed. Hagmann et al. [59] used a similar two step approach, where they randomly choose a voxel on the grey/white-matter boundary and assign its nearest neighbours (voxels) to the first region of interest until it reaches a specified size. This procedure is repeated with region centres close to the previously defined ROIs until the entire boundary is assigned. In a second step they reassign all voxels to their closest region centres, which are given by their centre of mass. A different approach was presented by Tymofiyeva et al. [153], where they treat the brain as a sphere, parcellate the sphere into equally sized regions and apply the mask to the cortex. This approach however does not distinguish between hemispheres and may lead to regions defined across hemispheres, meaning it is possible for a single region to belong both to the left and right hemisphere of the brain.

3.7.2 Edge weights

Networks may have weights assigned to their edges, where the weight corresponds to the strength of the connection. There are a variety of methods with which the weights of an edge in the human brain can be determined, however, there is no consensus on which approach is the most appropriate. Weights in structural brain networks are associated with, for example, fractional anisotropy [87, 157, 161], fibre count [59, 87, 157] or measurements of myelin content [161], whereas functional networks may use correlations between regions as weights [165].

These measurements, however, are difficult to interpret when using probabilistic tractography. Two regions within the brain may be connected by two streamlines inferred from probabilistic tractography with different probabilities (see section 2.2.2) [20]. The question that arises is how the individual streamlines should be weighted, considering that the low probability streamline may be erroneous. One way to incorporate the probability information from the probabilistic tractography with biological features, such as anisotropy, was proposed by Robinson et al. [119]. Applying probabilistic tractography between two regions in the brain results in a set of sampled voxels. Subsequently each sampled voxel's anisotropy in the direction of the streamline can be weighted by the number of times the voxel was sampled, divided by the total number of samples. The sum of all the measurements in the voxels that are traversed when inferring a tract can then be assigned as weight of the tract. This approach for creating weights in networks is used in the remainder of this work.

3.7.3 Degree distribution and hubs

Networks can be assessed according to their degree distribution - a histogram of the number of connections each node in the network has [10]. In particular in brain networks it has been shown that this degree distribution follows a heavy-tail pattern [59, 159], as illustrated in Figure 3.13.

This pattern emerges due to the existence of a small number of nodes which are integrated in the network with a relatively large proportion of edges (hubs). In general, hubs within a network may be identified using a variety of network theoretical measures beyond nodal degree, such as high betweenness centrality and short characteristic path-length [14, 139, 160, 161]. It has to be noted that no single measure may be sufficient for defining network hubs [158] and subsequently a combination of multiple measures may be used to define a

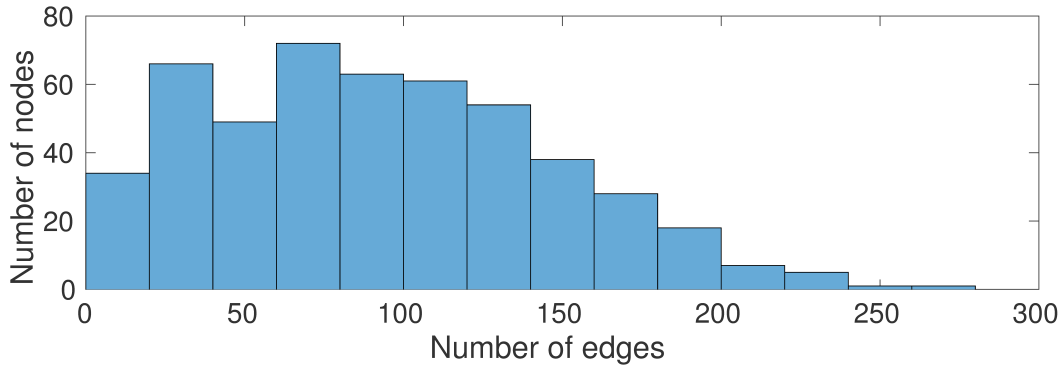

Figure 3.13: Heavy-tail degree distribution of a structural network in a premature baby scanned at 29 weeks post menstrual age. To define the regions Poisson disk sampling was used (see section 3.7.1; target: 500 regions). The heavy-tail on the right side indicates that there is a small number of regions/nodes with a large number of edges connecting them to the rest of the network (hubs).

hub-score (see for example [161]).

Network hubs have been of key interest while investigating brain networks, in particular with respect to their importance to network architecture and function (for a recent review see [158]). Sporns et al. [139], for example, analysed structural and functional networks in both cat and macaque monkey networks and related the structural role of hubs to their functional role. Their work suggests that these hubs play a central part in the overall brain network organisation and function, in particular with respect to local segregation and global integration.

3.7.4 Rich-Club Organisation

The brain is thought to conserve wiring costs as an important selection pressure [29]. The formation of highly connected rich-club nodes, which represents a high-cost architectural feature [36, 148], may seem surprising at first, however, the cost has to be offset against its cognitive value [30, 36]. It has been suggested that rich-club organisation has important consequences for efficient communication and functional integration across the brain [148, 157, 158].

Rich-club organisation has been shown to exist across species, starting with relatively simple brain architectures as found in C. elegans [148]. Further studies have been conducted in cat [39] and macaque monkey [63] brains with similar results, suggesting that the rich-club organisation is a general architectural principle for brain network organisation. Moreover van den Heuvel and Sporns [157] showed that the identification of the rich-club was possible in hu-

man structural brain networks on two scales (82 and 1170 regions) suggesting that the organisational principle is retained across scales.

3.7.5 Small-World Networks

The small-world phenomenon has become an interesting research topic in the human brain. The human brain is likely to exhibit small-world characteristics, as it is a complex network on multiple levels and over time, supports segregated and distributed information processing and has most likely evolved to maximise efficiency while minimise wiring cost [15]. In a study applying small-world topology to a neural network machine learning algorithm, it has also been shown that small-world networks allow for high rates of information processing and learning [132].

Structural networks. In 1998, Watts and Strogatz investigated the network structure of C. elegans, the first brain network to be fully mapped. By calculating the clustering coefficient and characteristic path length of this network, they determined that the C. elegans' brain network exhibited small-world characteristics [169]. Similar experiments were conducted in the brain of the macaque and the cat, showing small world architecture [65]. The small-world topology of the human brain was further investigated by Hagmann et al. [59] in a diffusion spectrum study. They revealed small-world structures in the human brain, as well as the existence of central hubs and a structural core [59, 60].

Functional networks. Various studies have investigated the small-world architecture of functional connectivity in the human brain. These properties were shown, for example, by Salvador et al. [124]. In a fMRI study with 90 cortical regions, they showed that functional human resting state networks exhibit small-world topology. Similar results have been shown to be present at the voxel level [159]. Overall, the small-world architecture of human brain networks allows simultaneous segregated and distributed information processing, while making the functional network more resilient to targeted attacks on their hubs, i.e. their underlying grey matter regions [1].

3.7.6 Injury and Disease

Head injuries are considered a major health issue [73] and subsequently it would be beneficial to understand the underlying effects of these types of injuries on brain networks. One type of head injury that can affect network function in the brain is traumatic brain injury (TBI; see for example [131]). Pandit et

al. [109] studied the effect of TBI on network topology in the human brain. They showed that the functional networks of TBI patients shift away from a small-world configuration through an increase in average path-lengths and no significant change in clustering coefficients. Moreover they suggest, by using dMRI data, that TBI and related traumatic axonal injuries are related to the impairment of long-range connections. Fagerholm et al. [49] further showed that the nodes impaired by traumatic axonal injuries are central hubs within the brain networks and that betweenness centrality of these nodes may be affected due to (partial) disconnections.

In order to improve diagnoses of diseases it is highly desirable to identify suitable biomarkers. In this context, network theory has been applied in studies for conditions such as Alzheimer's disease (AD) and attention deficit hyperactivity disorder (ADHD), where most studies focus on functional brain networks [14]. In general, the most prominent candidate as a biomarker seems to be the small-world coefficient and the correspondingly related network measures, such as clustering coefficient, characteristic path length and efficiency.

The first study in children of pathology-related variations in brain network topology considering ADHD was presented by Wang et al. [168]. They investigated 90-node networks generated using the AAL atlas (see section 3.7.1; [155]) and the functional connectivity matrices were symmetrised and binarised over a wide variety of thresholds. They investigated small-world architecture and efficiency in ADHD patients compared to a control group and suggested that the network structure becomes more lattice-like by increasing the local efficiency. This supports the idea of an increased disease tolerance, which can be interpreted as a defence mechanism [168]. Despite these changes the overall degree distribution remained the same and the small-world topology in ADHD patients, even though reduced, did not vanish.

In comparison with other diseases, research on AD is more prevalent. Supekar et al. [144] utilised a 90-node undirected functional network, based on regions defined by anatomical templates, in order to test the effects of AD on the small-world characteristics and efficiency of the network. They found that the clustering coefficient of the functional network provided a good biomarker, as patients showed a general decrease compared to the control group, while the characteristic path length stayed roughly the same, resulting in a decreased small-world coefficient [144]. Lo et al. [87], on the other hand, investigated the structural networks of AD patients. They constructed networks with 78 nodes and connections were considered to be present, if fibre bundles either passed

through or ended in one of these regions. Weight was assigned to each connection by multiplying the number of fibres with the mean fractional anisotropy along the way. They showed that both AD and control networks exhibit prominent small-world topologies. However, due to the increased characteristic path length, the small-world coefficient and global efficiency of the AD patients were lower than in the control group, while the local efficiency was increased [87].

3.7.7 Human Brain Development

There are relatively few studies of the developing brain, as they face challenges, such as poor data quality due to movement, small head sizes and lack of a standard scheme for parcellating the cortex (see section 3.7.1). Nonetheless the network analysis of the developing brain is of great interest as it is clinically and neuroscientifically important to characterise the "normal" developmental trajectory. This will ultimately help with the detection and diagnosis of pathological development and diseases at an early stage. For a recent review on the development of brain networks see [151].

In general it has been shown that the developing human brain shows interesting characteristics, such as an asymmetry between the left and right hemisphere in respect to their network measures, as well as differences related to the sex of the subject [41, 178]. The results for the latter are still inconclusive as there are only a few studies focusing on that particular aspect, but studies suggest that females have a higher global and regional efficiency, as well as a higher clustering coefficient, resulting in a higher small-world coefficient compared to males [41, 178].

One interesting area of analysis is the determination of the network structure of the cortical network. However, the exact network type of the brain has not been determined yet. Nonetheless, studies suggest that the degree distribution follows either a power-law decay [141], a power-law decay with a sharp cut-off [178] or an exponential decay [59], allowing for small-world characteristics and resilience to random failure.

Community structure. It has been suggested that brain networks develop from a local to distributed organisation [51, 178]. Long-distance connections are generally rare in biological networks [141]. However, they allow for short-cuts within the network and are essential for efficient information transport. Starting from a local anatomical network, the architecture becomes more distributed during development, evolving from a more segregated to a more integrated network structure [141, 178]. While structural modules remain com-

posed of spatially adjacent regions, their interconnectivity with distant regions strengthens with the maturation of long fibre paths [178]. This is most likely due to the change of connection strength during the myelination process, as it has been indicated by post-mortem studies that there is no new fibre creation after birth [178].

It has also been suggested that the structural modules of brain networks do not undergo major reorganisation after two years of age [61]. However, Dennis et al. [41] suggested that the structural clustering coefficient decreases with age. Similar to the structural network analyses, it has been suggested that there are no major changes in functional modularity over the range from 8-25 years [52]. Further studies and better community structure finding algorithms are necessary in order to reveal the general trend during development, in particular in the early stages.

Rich-Club Organisation. A first investigation of the development of the rich-club organisation in the developing human brain was presented by Ball et al. [8]. They showed that the rich-club already existed in premature born babies at 30 weeks post menstrual age and that the connections between the members of the rich-club were already present at that time. This suggests that rich-club organisation is established before normal birth. On the other hand, feeder and local connections were still developing.

Small-World Networks. Studies agree on the existence of small-world topology in neural networks over all developmental stages [51, 52, 178]. However, it has been shown that the efficiency increases with age [52, 178]. This is most likely due to the myelination process within the brain, which allows the impulse propagation speed to increase. On the other hand, the structural clustering coefficient appears to decrease with age [61]. Combining various studies, it seems that the small-world phenomenon in the human brain becomes more pronounced up to an age of two [178] and then decreases at later developmental stages of life [41, 61], suggesting a plateau during development. These results agree with the determined cost efficiency of the studied networks, which seems to reach its most efficient point at the age of two [52].

3.7.8 Multi-scale analysis

This work distinguishes between the mapping of the connectome over multiple levels such as micro- and macroscopic scales as discussed by Leergaard et al. [81], and the multi-scale analysis based on varying the number of regions defined over grey matter as discussed in section 3.7.1. In most of the previously

mentioned studies, networks are defined over a single scale, by using for example an atlas template. However, the resulting networks are strongly dependent on the number of nodes/regions over which they are defined [153], which makes comparisons across studies difficult. In particular, it has been shown that network measures vary according to the networks scale, which poses challenges for comparisons within a study that uses various scales [127, 164, 179] or across different studies that use different atlases with varying number of regions [46, 99, 127, 146]. Figure 3.14 illustrates this dependence for a commonly used network measure (characteristic path-length) in weighted brain networks of a single preterm neonate (see section 2.3). Most recent studies acknowledge this dependence, however, a consensus on how to address this challenge is yet to be established, necessitating further investigation in the context of neuroimaging studies of a range of cohorts. Network normalisation has been proposed to alleviate this challenge and will be further discussed in chapter 4.

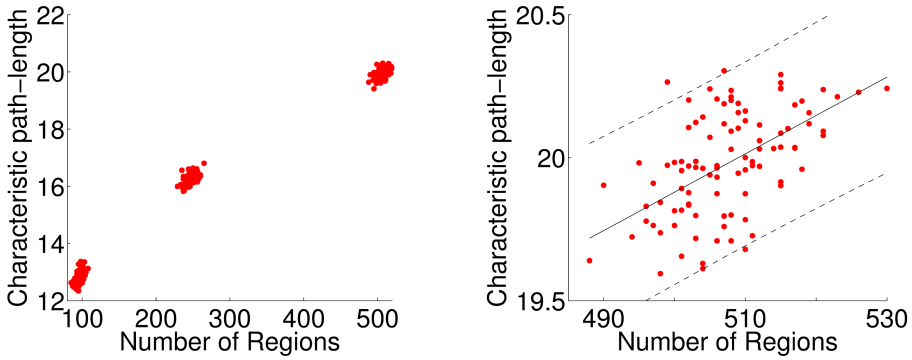

Figure 3.14: Dependence of the characteristic path-length on the number of regions in weighted brain networks of a single neonate (33 weeks GA). Left: Sets of different parcellations of the same subject with around 100, 250 and 500 regions. Right: Detailed view around 500 regions, with a fitted linear regression and 95% confidence intervals.

The application of nodal multi-scale approaches has also become of interest. Cammoun et al. [31] introduce a multi-scale framework using an atlas based segmentation of the grey matter with 66 regions and subdivided these regions further into four additional sets of about 125, 250, 500 and 1000 regions with approximately equal region size. By doing so they aimed to define representative connectivity matrices over multiple scales, however, they did not investigate changes of network measures as introduced in section 3.3. Additional studies have compared networks defined over multiple scales in both structural and functional data in adults and the developing brain [53, 157, 176, 179]. These studies mainly investigate whether the conclusions based on network

measures are stable across scales and emphasise that a comparison of results across studies should be made with reference to scale.

Other multi-scale approaches applied to the macroscopic level include, for example, a wavelet representation of a line graph [76], a graph where the role of edges and vertices are switched, in order to find a representation for each vertex in form of a multi-scale descriptor. In this case however, the term multi-scale is based on the effect of bandpass filters applied to the wavelet transformed line graph and thus not on the definition of the number of regions. Another definition in the framework of community detection stems from the use of Markov random walkers [25], which have an intrinsic time scale after which the walker stops. Betzel et al. [25] define multi-scale as variation of random walker time scales in order to separate communities on local (small) and global (large) scales within a network.

Chapter 4

Random Parcellations for Network Analysis

4.1 Motivation

Network analysis of brain imaging data typically begins by defining a set of regions within the brain, which serve as nodes. A variety of approaches may be used to define these regions, as described in section 3.7.1. In case of structural connectivity, the corresponding edges in the graph can be determined and possibly weighted based on tractography analyses of diffusion MRI (dMRI) data [44, 60, 140].

This work applies methods for the analysis of structural connectivity in the developing brain. This field of research is of particular interest, as it has been shown that preterm birth is associated with adverse neurocognitive outcome in later life (see section 2.1.1). Understanding the development and formation of structural connectivity after preterm birth is therefore an important goal, however, there are particular challenges in structural network analyses for neonatal groups. The acquisition of high quality dMRI data in neonates is difficult, because their brain sizes are much smaller than in an adult and additional care has to be taken for temperature maintenance, monitoring and immobilisation to reduce motion [147]. A particular challenge lies in the absence of a standardised anatomical delineation, which can be used to define network nodes (see section 3.7.1). The lack of such a standard is partly related to the significant morphological changes that the neonatal brain undergoes (see section 2.1). This makes the use of randomly generated parcellations as

described in section 3.7.1 an attractive alternative, as these approaches rely on fewer assumptions regarding the presence and boundaries of functionally coherent regions [7, 8, 151, 152].

4.1.1 Poisson disk sampling

A common criticism of applying random parcellation schemes to brain imaging data is the potential reduction of functional coherence within a defined region. This is assumed to be present, for example, in the Automated Anatomical Labeling (AAL) atlas (see section 3.7.1). To motivate the analysis of brain data using random parcellations, a comparison of global structural brain network measures obtained using Poisson disk sampling (see section 3.7.1) and using the AAL was carried out.

In a preparatory analysis, a set of global network measures calculated for networks generated using Poisson disk sampling were compared with those generated using the AAL atlas of the cortex. Figure 4.1 shows the comparison of all network measures evaluated for Poisson disk sampling and for AAL. Each data point represents a global network measure either generated using Poisson disk sampling (green) or AAL (blue). Considering that AAL defines 78 cortical regions (39 per hemisphere), it was ensured that the parcellations obtained using Poisson disk sampling generated comparable numbers of regions and investigated scales between 68 and 88 regions.

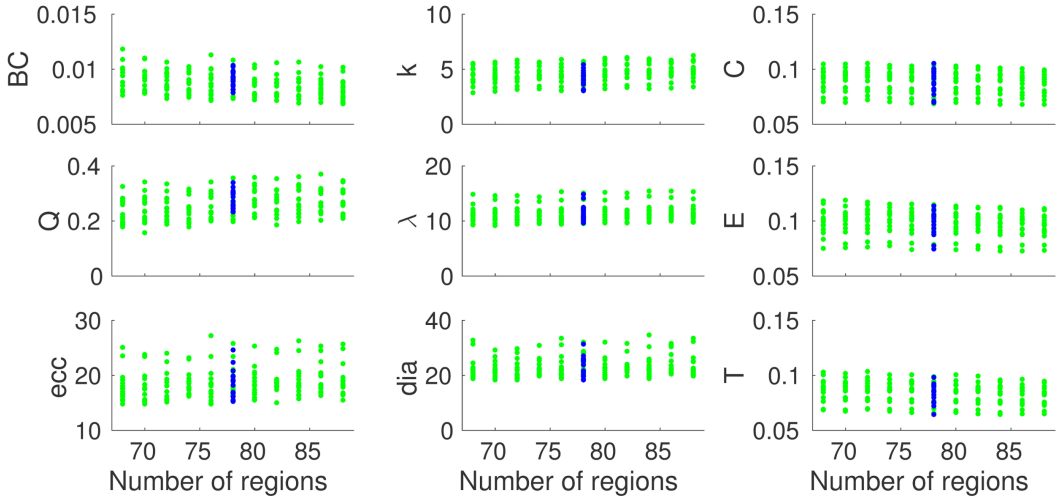

Figure 4.1: Comparison of global network measures generated using Poisson disk sampling (green) and AAL (blue). The results show that global network measures calculated from AAL parcellations fall in the same range as those calculated from Poisson disk sampled parcellations.

Figure 4.1 shows that networks created using Poisson disk sampling show similar global characteristics to those created using AAL. The results created using Poisson disk sampling fluctuate due to the stochastic nature of the approach and only one parcellation has been used per scan at each scale. By analysing random parcellations over a range of scales around the atlas scale, it was possible to demonstrate the comparability of the network measures. A subsequent comparison of the results at the atlas scale (78 nodes) using a paired t-test for each measure and all subjects shows p-values of $p > 0.1$ for all global network measures, indicating the comparability of global network measures obtained from both parcellation schemes. A more extensive analysis could use multiple random parcellations per scan at each scale to characterise fluctuations of the Poisson disk sampling more fully.

Using a set of 16 brain networks, five random parcellations per subject at the AAL scale are compared with results generated using the atlas, as shown in Figure 4.2. Values calculated from Poisson disk sampled parcellations broadly agree with those calculated from AAL parcellations.

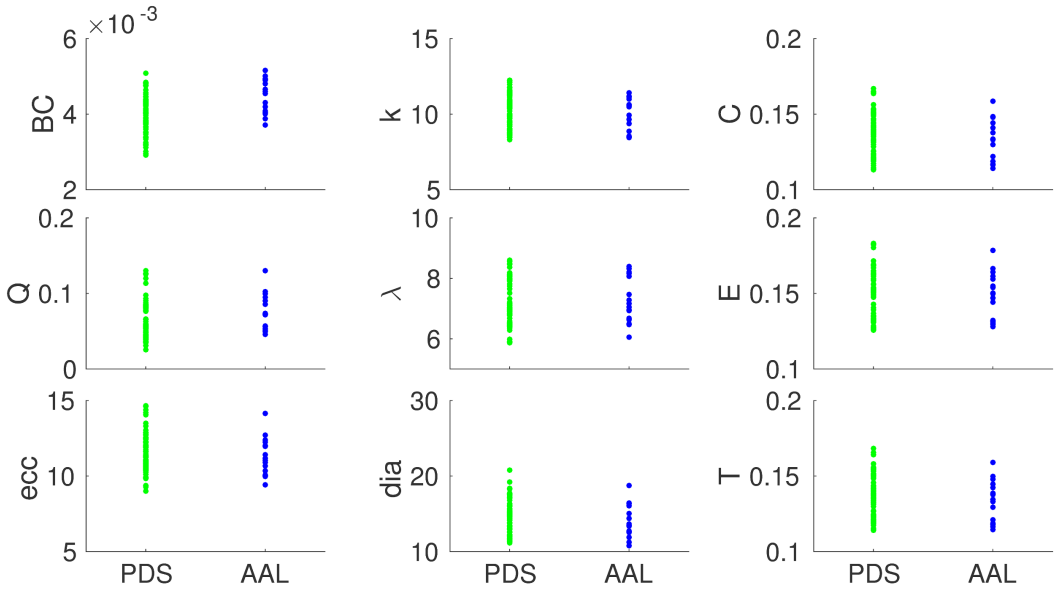

Figure 4.2: Comparison of global network measures generated using multiple instances of Poisson disk sampling (PDS) per subject at the atlas scale and the AAL atlas. Global network measures calculated using Poisson disk sampling broadly agree with the measures calculated from AAL parcellations.

The comparison of the results using a paired t-test for each measure and all subjects shows p-values of $p \geq 0.1$ for all global network measures, except for betweenness centrality ($p < 0.01$). This could be explained due to changes in betweenness centrality that could occur if the definition of regions does not

correspond with the underlying connectivity profile, as illustrated in Figure 4.3. These changes may result in a smaller betweenness centrality value as shown in Figure 4.2.

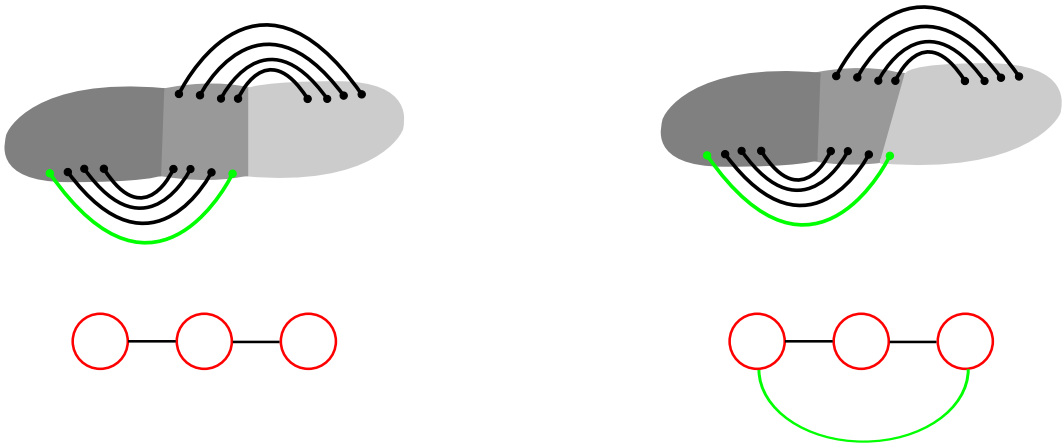

Figure 4.3: Small changes in the definition of the regions of interest (top) can lead to different topology of the estimated network (bottom). Reassigning the edge shown in green causes a reduction of global betweenness centrality.

The results shown in Figure 4.2 allow the use of two-sample t-tests for each subject with respect to the results generated using AAL and Poisson disk sampled parcellations. Table 4.1 summarises the results of the paired t-tests into number of significant and not significant tests. Non-significant results indicate that there is no benefit of using an atlas based parcellation over the use of Poisson disk sampled parcellation.

Table 4.1: Number of significant t-tests when comparing each subject's global network measure based on its' AAL parcellation to the distribution estimated using five Poisson disk sampled parcellations.

	BC	k	C	Q	λ	E	ecc	dia	T
not significant	7	10	10	7	13	14	15	16	10
significant	9	6	6	9	3	2	1	0	6

The results show that for each network measure most comparisons on the subject level are not significant, except for betweenness centrality (BC) and modularity (Q). Only five random parcellations were used to represent the distribution of measures and subsequently the distribution may not be well estimated. Additional network measures generated using Poisson disk sampled parcellations could be used to achieve a better estimate. In general, generating multiple parcellations for network analysis has to be set off against the computational costs and needs to be guided by the research question at hand. In

case of extracting a single network measure for each subject at a given scale, multiple parcellations are recommended to ensure that the obtained measure is an acceptable representative of the distribution generated by random parcellations.

Importantly, Poisson disk sampling allows for a relatively easy generation of brain parcellations at arbitrary scales, while still being able to capture global network properties at the atlas scale. This furthermore allows comparisons of networks generated at different scales. When using probabilistic tractography however, higher scales can lead to an increase of erroneous connections. Recent papers, which explore networks over multiple scales as described in section 3.7.8, investigate scales with more than 1000 nodes in adult data (see for example [53, 157, 179]). However, considering the small brain sizes and incomplete myelination of the subjects of interest in this work, a middle ground between the AAL atlas scale and the highest scales in the literature was deemed empirically to be most suitable. Under these considerations, the work in this chapter was carried out using around 500 brain regions per parcellation.

4.1.2 Network Measures: Normalisation and Correlations

It has been shown that the number of nodes in a parcellation influences the resulting network measures of the brain and subsequently a comparison between studies may be influenced by the definition of nodal scales (see section 3.7.8). Network normalisation may be utilised to compare subjects or groups in a manner which is assumed to be less biased by the number of nodes on which a graph is defined. Such an approach can normalise a measure $m(G)$ for an observed graph G against the value of $m(G')$, where a graph G' is generated from G by randomly perturbing its edge structure and/or its edge weights. Although these randomised networks may not represent physiologically plausible networks, their network measures act as a reference point for the observed measure $m(G)$. This chapter evaluates the suitability of different normalisation approaches, including established methods, and quantifies their effectiveness over a range of around $470 - 530$ nodes/regions. The range of regions was a result of using Poisson disk sampling to generate parcellations with a target number of 500 regions per parcellation (see Figure 3.12). In this chapter it is also shown that established random graph approaches that rely on rewiring can lead to unsuitable normalisations for measures such as characteristic path-length by considering the non-linear correlation between the number of regions

and the network measures of interest.

The aim of this work is to obtain a single measure for a structural network, which is effectively sampled through a variety of parcellations with different numbers of regions generated randomly using Poisson disk sampling. In contrast to previous studies [164], which state the dependence of the results on the number of nodes and the degree in network analyses, this work tries to solve the number of node dependency for the case of Poisson disk sampling, by generating a random network which shares some properties of each sample. This approach is in contrast to the comparison of independently generated networks with the same topology at multiple scales, as the topology of observed networks may change, when varying the scale [164].

Furthermore, associations have been shown among many common network measures obtained from brain data, and therefore they may have overlapping representations of the underlying network topology [71, 85]. This motivates the definition of a maximal set of independent network measures in order to describe an observed network. The majority of analyses of network measure inter-dependence rely on linear correlation (see for example [88]). However, some of the analytic solutions for network measures in binarised networks exhibit non-linear relationships and it has been suggested that the inter-measure relationships for weighted networks are also non-linear [85].

In order to determine a meaningful subset of measures, the non-linear correlations among the network measures themselves is investigated and strong associations among a set of commonly used network measures are confirmed. Based on these results, a compact set of network measures is propsed to characterise brain development. This chapter concludes by validating the proposed method by applying it in an investigation of the change of network measures over time in a serial dMRI dataset of 28 premature neonates.

4.2 Methods and Material

4.2.1 Subject and Image Data

Multiple random parcellations of each cortex of the preterm cohort, as described in section 2.3, were obtained at both time points using Poisson disk sampling (see section 3.7.1). The use of a probabilistic parcellation method is well motivated as an established number of brain regions in neonatal network analyses is not determined. For all parcellations, a probabilistic diffusion trac-

tography algorithm (ProbtrackX [23, 119]) was applied in order to generate structural networks (see section 2.2.2). An edge between a pair of regions in the structural networks was assumed to be present if at least one streamline reached a target region from a source region. Streamlines were excluded if they left the brain mask, entered voxels containing cerebrospinal fluid or exceeded a curvature threshold.

Each edge was weighted by the average of the integrated anisotropy along the streamlines connecting the two regions [119] (see secton 3.7.2). In general, this approach returns a directed graph without multiple edges and/or self-loops, which is then symmetrised. To remove the direction dependence between two nodes r and s, the mean of their connection weights $w' = (w_{rs} + w_{sr})/2$ is assigned to both edges, creating a weighted and undirected graph.

4.2.2 Network randomisation

This section summarises the methods used to generate random networks in this chapter, based on methods to determine the edge structure and edge weights.

Edge structure

In the following, two established algorithms to create random surrogate networks for comparison are investigated, using either an Erdös-Rényi model (ER) [47] or pairwise switching of the edges (PS) [96], an algorithm which keeps the number of edges connecting each node constant (see section 3.6). Keeping the edge structure without alteration will be referred to as 'edge preserving' (EP). The principle of "altering" the edge structure during randomisation is shown in Figure 4.4.

Weight assignment

As this work is based on weighted graphs, it is necessary to define methods for assigning weights to the edges of a randomised graph derived from an observed graph. The original weights set (OW) may be redistributed naturally in case of PS and ER by carrying them along with the edges [121], or randomly permuted for EP [107]. In case of PS the switching of edges can also be restricted by preserving individual weighted degrees (WDP). A switch in the PS algorithm is then only executed if the resulting switch will preserve the weighted degree of the nodes involved. In order to improve the amount of randomisation using

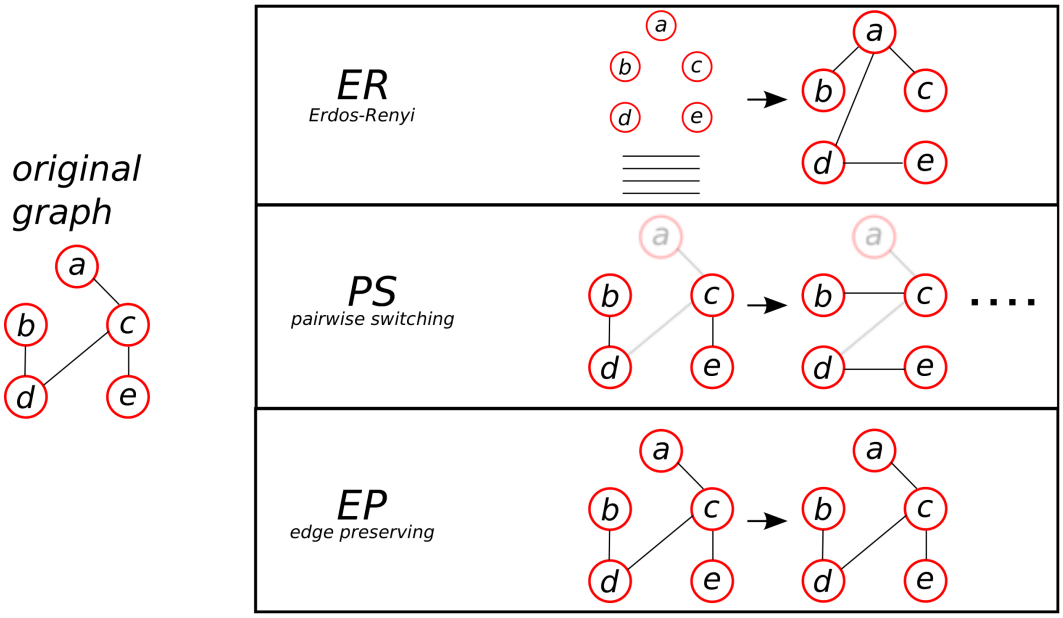

Figure 4.4: General principle of the three possible edge structure adjustment methods used to generate randomised realisations from an observed network G. In case of EP, the randomisation step is solely due to the randomisation of the edge weights.

a weighted degree preserving pairwise switching scheme, an alteration of up to 5% of the original weighted degree is permitted.

Weights are also drawn uniformly (UNI) from the interval $(0, w_{max}]$, where w_{max} is the maximum weight in the original graph. Finally weights are drawn at random from the weight set calculated from the shortest path distances between all node pairs in the original graph, which are calculated using the Dijkstra algorithm (D) (see section 3.2). For the last method, distances along each edge $\{ij\}$ may be represented by $1/w_{ij}$ [121]. The resulting shortest distances between all node pairs are then converted back to weights, again as reciprocals, to generate a complete weighted graph matrix. The elements of this matrix are randomly drawn for assignment to the randomised version of the graph. The abbreviations for all the network randomisation schemes used are summarised in Table 4.2.

Table 4.2: Abbreviations of the random network generation schemes used.

	Original weights	Uniform	Disjkstra	Weighted nodal degree preserving
Pairwise switching	PS-OW	PS-UNI	PS-D	PS-WDP
Erdös-Rényi	ER-OW	ER-UNI	ER-D	
Edge preserving	EP-OW	EP-UNI	EP-D	

4.2.3 Network measures

This study uses global network measures commonly thought to represent local segregation, global integration and the prevalence of important nodes (see chapter 3). Table 4.3 broadly subdivides the measures investigated into these categories. All measures were calculated using the Brain Connectivity Toolbox [1].

Table 4.3: Categories of investigated network measures.

Category	**Measure**
Local segregation	Clustering coefficient (C), Transitivity (T)
Global integration	Charactersitic path-lenth (λ), Efficiency (E) Diameter (dia), Degree (k)
Node importance	Betweenness centrality (BC)

4.2.4 Graph normalisation

The presented methods normalise a measure $m(G)$ on a graph G against the value of $m(G')$, where G' is obtained by randomly perturbing the structure of G, modifying its edge structure and/or edge weights, as described above. These randomised networks may be seen as a reference point that can be used to assess the significance of network measures obtained from observed data according to their departure from this point. The normalisation framework is schematically illustrated in Figure 4.5.

4.2.5 Measure correlations

Previous analyses have focused only on linear correlation [85], however, in order to allow for non-linear correlations Spearman's rank correlation coefficient is used. In addition, the inter-measure correlation before and after normalising the network measures is assessed to see the effect of the normalisation. This helps to characterise how the dependence on the number of regions affects the observed inter-measure correlations.

[1] BCT [121], `http://www.brain-connectivity-toolbox.net`

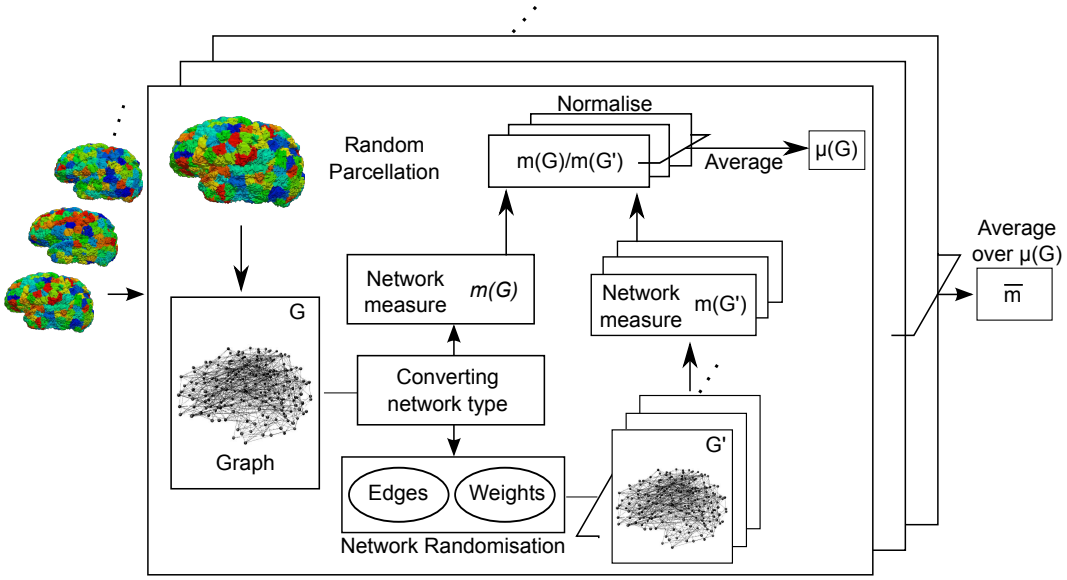

Figure 4.5: Processing pipeline for removing the number of region dependence for one subject. The normalisation of a network measure $m(G)$ for a particular parcellation may be carried out using multiple randomisations of the network it defines. This is then repeated for all the parcellations for the subject.

4.3 Results

4.3.1 Region dependence of network measures

The performance of the different normalisation schemes, each comprising a method for modifying the edge structure and a method for assigning weights (see Table 4.2), is assessed in a series of experiments. Using Spearman's rank correlation coefficient, the correlation of each measure with the number of regions is calculated for parcellations around 500 regions (target: 500; range: $470 - 530$) in eight of the subjects (mean age at scan: 30.5 ± 1.5 weeks PMA). The normalisation process was repeated ten times and the result for each process were recorded. The average correlation coefficients for all measures analysed for all randomisation combinations using eight subjects with 100 networks each are given in Table 4.4.

The normalisation schemes which draw weights from a uniform distribution between zero and the maximum weight of the original matrix performed generally well, compared to the other weight assigning methods. In particular, for clustering coefficient and characteristic path-length, the uniform weight assignment out-performed the commonly used ER-OW and PS-OW schemes.

The results suggest that preserving the edges, while drawing weights from

Table 4.4: Spearman rank correlation coefficient of measures with the number of regions. Bold numbers mark the correlation coefficient closest to zero, indicating the greatest reduction of the correlation between network measure and number of regions.

		BC	k	C	λ	E	dia	T
	Before	0.90	0.08	-0.66	0.57	-0.62	0.10	-0.59
ER	OW	0.44	0.06	0.60	0.30	-0.33	0.04	0.64
	UNI	0.53	-0.08	0.18	0.12	-0.11	0.06	0.18
	D	0.21	0.43	0.59	-0.16	0.26	-0.03	0.60
PS	OW	0.36	0.06	0.62	0.34	-0.40	**-0.01**	0.67
	WDP	-0.63	0.08	-0.67	0.57	-0.63	-0.60	0.15
	UNI	0.49	-0.08	**0.08**	0.11	-0.10	0.04	0.09
	D	0.19	0.42	0.63	-0.19	0.31	-0.06	0.62
EP	OW	0.09	**0.05**	**-0.08**	0.15	-0.19	-0.04	0.14
	UNI	0.29	-0.08	**-0.08**	**0.08**	**-0.08**	**0.01**	**-0.07**
	D	**0.00**	0.43	0.40	-0.32	0.40	-0.10	0.39

a uniform distribution between zero and the maximum weight of the original graph (EP-UNI) achieved, on average, the greatest reduction in correlation of the measures with the number of regions. Further analyses therefore focuses on randomisation schemes based on uniformly drawn weights, while preserving the edge structure. The normalisation scheme was applied to a serial dMRI dataset of 28 subjects with 100 parcellations at a target number of 500 regions each by generating one random realisation of the observed network. Repeating the normalisation multiple times with varying random graphs did not yield major improvements.

Using the EP-UNI scheme, the correlation of network measures with further properties of the networks, the number of edges and the network density (defined as the ratio of number of existing edges to the number of possible edges), were assessed. Spearman's rank correlation coefficient was calculated for all subjects and for each measure and subsequently averaged over all subjects. The results are given in Table 4.5 and show a substantial reduction in correlation between all network measures and numbers of edges (equivalent to $66 \pm 23\%$), as well as network density (equivalent to $76 \pm 14\%$), further underlining the potential of the proposed approach.

Additionally, a breakdown threshold was estimated, below which the normalisation approach does not yield major improvements, starting from around 500 nodes. To do so, one subject was parcellated 100 times over a range of around $100 - 530$ regions (steps of five, with one repetition at each step). Subsequently, a quality factor q was assessed. The quality factor was

Table 4.5: Average Spearman rank correlation coefficient of measures with the number of edges and with network density. The average was calculated over 28 subjects at two time points with 100 networks each for all measures analysed using EP-UNI.

	Number of Edges		Density	
	Before	After	Before	After
BC	-0.80	0.29	0.25	-0.13
k	0.52	-0.09	0.60	0.10
C	-0.50	-0.08	0.55	0.11
λ	0.26	0.09	-0.68	-0.11
E	-0.31	0.09	0.77	0.10
dia	0.04	0.04	-0.18	-0.06
T	-0.44	-0.10	0.59	0.08

defined as

$$q = 1 - \|corr_n\|/\|corr_r\|,$$

where $\|corr_r\|$ and $\|corr_n\|$ are the absolute values of the correlation before and after normalisation, respectively. If the correlation after normalisation reaches zero, the quality factor reaches 1, whereas if there is no change in correlation after normalisation, the quality factor will be 0.

Number of regions were estimated for which the quality factors were below values in the range of $q \in [0, 1]$ for each measure. The results are shown in Figure 4.6. In case of a quality factor of $q = 0.5$, the number of regions at

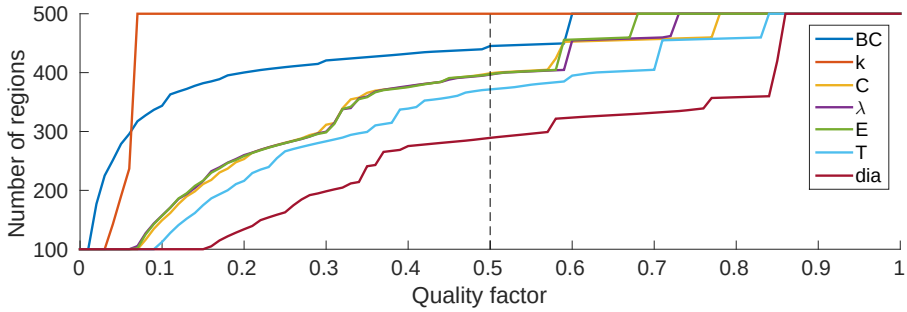

Figure 4.6: Number of regions estimate at which the normalisation scheme breaks down, depending on the quality factor. In the graph 500 regions means no improvement beyond the quality factor.

which the normalisation scheme breaks down, calculated as the average over all measures, was determined to be 400 regions. In case of network degree, it should be noted that there is only a small improvement after normalisation, as indicated in Table 4.4.

4.3.2 Inter-measure correlations

In order to determine a useful set of network measures to help characterise changes in the developing brain, correlations among the measures of all subjects were verified by calculating the Spearman rank correlation coefficient between each pair of measures. To assess the effect of the number of region dependence, the data set was analysed before and after applying normalisation, using the EP-UNI scheme. Group-wise correlation coefficients are summarised by calculating the mean over all subjects. The results are given in Table 4.6. Standard deviations before and after normalisation were on average below 0.1.

Table 4.6: Average inter-measure correlations before (top) and after (bottom) the normalisation, where the average was taken over 28 subjects at two time points with 100 networks each using the EP-UNI scheme.

Before	**k**	**C**	**λ**	**E**	**T**	**dia**
BC	−0.8	−0.6	0.8	−0.7	−0.6	0.7
	k	0.9	−1.0	1.0	0.9	−0.9
		C	−0.9	0.9	1.0	−0.8
			λ	−1.0	−0.9	0.9
				E	0.9	−0.9
					T	−0.8

After	**k**	**C**	**λ**	**E**	**T**	**dia**
BC	−0.1	−0.1	0.1	−0.1	−0.1	0.1
	k	1.0	−1.0	1.0	1.0	−0.4
		C	−1.0	1.0	1.0	−0.4
			λ	−1.0	−1.0	0.5
				E	1.0	−0.5
					T	−0.4

These results show that the correlation among the measures is high before normalisation. After normalisation the inter-measure correlation between degree, clustering coefficient, characteristic path-length, efficiency and transitivity increases to values close to ± 1.0 in each case. However the correlation of betweenness centrality and diameter with all other measures decreased, indicating that both measures genuinely represent contrasting aspects of the network topology. The general trends between pairs of measures before and after normalisation are shown in Figure 4.7.

In general, these results suggest that commonly used measures in the literature provide overlapping information on the topological features of brain networks. Furthermore, based on the trends in Figure 4.7, this analysis shows

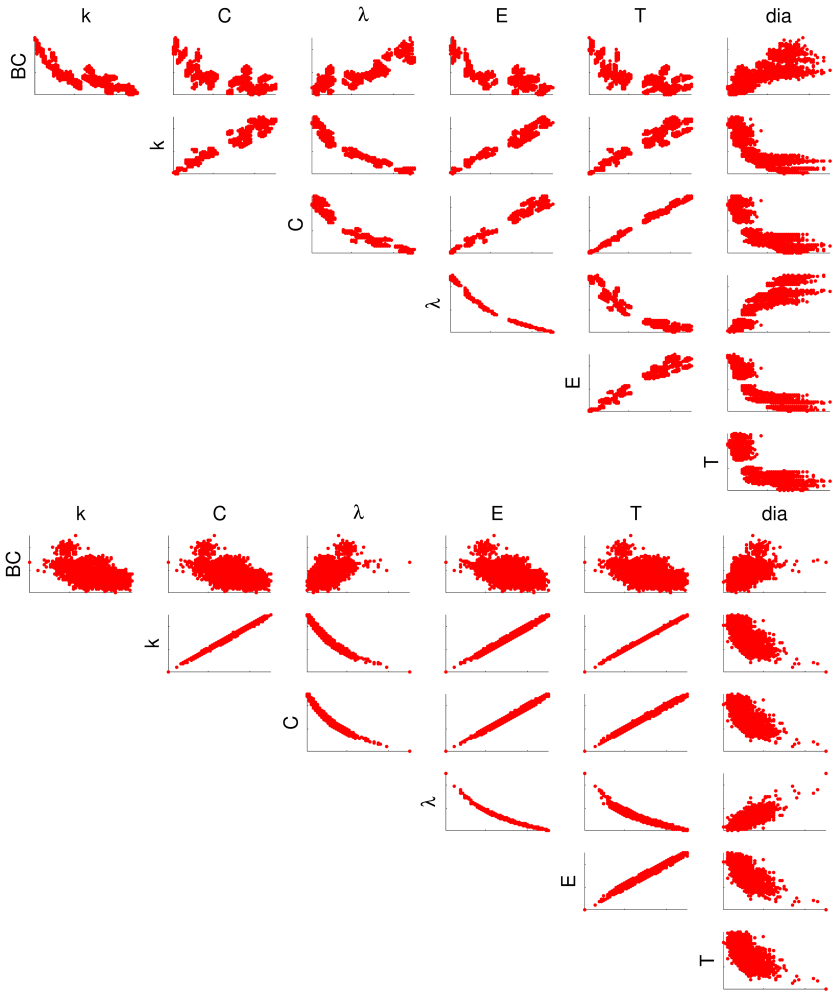

Figure 4.7: Plots of pairs of measures taken on all networks from 28 subjects with two time points and 100 networks each against each other before (top) and after (bottom) normalisation. Each data point corresponds to a measure taken from one network of one subjects.

that some relationships are non-linear, as suggested, for example, by Li et al. [85]. The accentuation/attenuation of the correlations after normalisation are likely due to the elimination of the shared number of region dependence.

In view of the correlations among degree, clustering coefficient, characteristic path-length, efficiency and transitivity, it is unnecessary to calculate all measures individually, as they can be summarised by any one measure. Considering that the degree of a network is the least computationally expensive, the remaining analysis focuses on the subset of measures consisting of degree, betweenness centrality and diameter.

4.3.3 Change of network measures with age

EP-UNI was applied to a serial dMRI dataset of 28 subjects with 100 parcellations each at each time point with a target number of 500 regions. Figure 4.8 shows the changes over time for all measures after normalisation. The results are assessed in terms of their change over time by calculating the corresponding p-values, based on paired t-tests. From about 30 to 40 weeks of age, the degree increases ($P < 0.01$), whereas betweenness centrality and diameter decrease ($P < 0.001$).

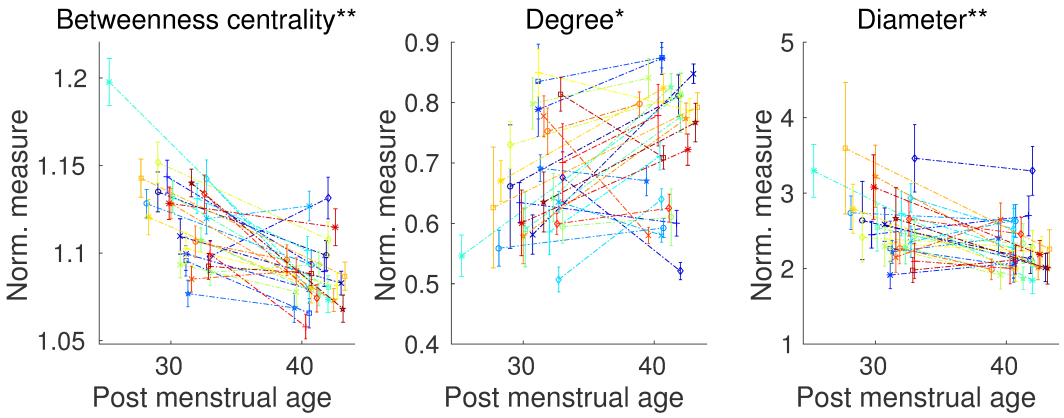

Figure 4.8: The figures show the median normalised values of network measures determined from 100 parcellations per subject at two time points plotted against the subjects PMA. Each colour-marker combination represents one infant with the distribution of measures from multiple randomly parcellated networks connected by a dashed line. Measures with a P value of $P < 0.01$ and $P < 0.001$ are indicated by one and two stars respectively. All measures show a significant change over the age interval studied.

4.4 Conclusion

4.4.1 Network normalisation

This work presented methods for generating random graphs for normalising network measures derived from weighted and undirected brain connectivity graphs. The results indicate that preserving the edge structure, while drawing the weights from a uniform distribution between zero and the maximum weight w_{max} in the observed graph (EP-UNI) can outperform other proposed approaches, such as ER-OW and PS-OW, with respect to the reduction in the number of region dependence of various topological measures. On average the absolute value of the correlations after normalisation is below 10% (compared

to an average of approximately 50% before normalisation), indicating that a more meaningful summary measure for each network measure can be determined around 500 regions. It should be emphasised though that some of the other normalisation schemes, such as EP-OW, perform similarly to EP-UNI.

Notably, there exists a larger variability of random network measures for EP-UNI compared to the other randomisation methods, which may cause a reduction or masking of the signal of interest (see section 7.1). Furthermore, by determining the most appropriate normalisation scheme based on the reduction of number of region dependence alone, it is possible that further masking may occur. Due to the lack of an appropriate null model for brain networks the assessment of the extent to which this occurs is challenging. A comparison of changes in network measures with expected biological changes may be used on a qualitative level to indicate if the signal of interest remains, however, the quantitative characterisation remains an open challenge. Nonetheless, the results suggest that a randomisation in the weights beyond altering the edge structure may form an important part of generating random networks for normalisation of weighted graphs.

In contrast to the work presented here, the approach of Van Wijk et al. [164] investigates the number of region dependence by analysing sequences of lattice, random and small-world networks of different sizes. In particular, although the networks within each sequence are of the same type, they are independently generated from one another, albeit using the same underlying process. Importantly, their work shows that the number of node dependence will not be eliminated using standard normalisation schemes, even if the topology is kept the same over multiple scales. As for the application to observed networks, a comparison over a range of scales is desirable, especially in the case of neonatal brain data. In this case, however, differences in scale may lead to changes in the topology of the networks, which contrasts to the comparison of a single network topology over multiple scales. In the proposed scheme for generating random graphs, by preserving the adjacencies of the observed network at each scale, changes in network topology due to scale may be reflected in the random graphs to some extent. This may be another important aspect in normalising observed networks and would be an interesting topic for future work.

The reduction of correlation between the number of regions and the network measures, as presented in this work, allows for a better local comparison for measures taken from graphs with around 500 regions. It should be noted that, with fewer regions, the variation in both observed and normalised network

measures increases. This emphasises the difficulty of comparing results based on the different scales, as they are commonly used in atlas-based methods [164]. This work focuses on, but is not limited to, solving inherent challenges with random parcellation schemes. In the case of neonatal cohorts, where the "true" number and location of regions is difficult to determine, random parcellation approaches may provide a less biased (with respect to number and location of regions) inference of changes in network measures.

Calculating a "breakdown criterion" showed that some dependence on the number of regions remains over a larger scale of 100-500 regions. This criterion with a starting point around 500 regions is only a first estimate for the point at which the random graphs generated for normalisation lose some of their representational power. In general, reducing the dependence on the number of regions enables network measures to be compared, not only across subjects and over time, but also across studies using different parcellation schemes, which is an important aspect of network analysis. Furthermore, it should be noted that there exist other methods for generating random surrogate networks than those discussed in section 3.6, however,the widely used Erdös-Rényi and pair-wise switching methods were chosen due to their historical significance and prevalence in the literature. A more comprehensive analysis is an appropriate topic for further investigation. Nonetheless, the normalisation schemes presented, besides allowing for an intra-/inter-subject comparison, may furthermore assist in determining the reproducibility of results based on network measures in case of atlas based work, in which atlases with varying number of regions are used [146].

4.4.2 Measure Correlations

This work highlights the inter-measure dependence between commonly used measures in network-based brain analyses which, in turn, demonstrates the difficulty of measuring the underlying topological features of a network. Based on the definitions of network measures, correlations are to be expected, regardless of any normalisation scheme. One assumption in weighted network analysis is that stronger connections correspond to shorter path-lengths which enable more efficient information transport. Taking this into consideration, an increase of average weighted degree (k) within a graph naturally leads to greater average efficiency (E). Similar reasons, again based on the network measure definitions, can be argued to underpin at least part of the observed correlations among them. It would be beneficial, for computational and analytic reasons,

to find a maximally independent set of network measures to characterise the brain. The selection of an independent set of network measures may be carried out using techniques such as independent component analysis or the analytical derivation of the relationships between weighted measures. However, the presented results allowed for a set of measures to be proposed, which can be used to describe features of early brain development. This set may then be used in second order analyses at the population level.

4.4.3 Developmental changes within structural brain networks

The application of the EP-UNI normalisation scheme to a serial dMRI dataset of 28 subjects agrees with previously suggested increase of network integration [141, 178] (see section 3.7.7). The increase in degree can be interpreted as an increase in connection strength, due to an increase in anisotropy with age. Although myelination is not apparent in the developing telencephalon during the preterm period, this time represents a period of significant development during which a number of maturational processes alter white matter organisation over time (see section 2.1). A strengthening of the connections during development is desirable, as it allows more efficient information exchange between brain regions. Similarly the decreasing diameter in both network types suggests an increased global integration of all network nodes/regions and thus more rapid information transport throughout the entire network. These results suggest that the brain develops towards a higher efficiency with respect to information flow on a local and global scale within the first few weeks after birth.

Chapter 5

Multi-Scale Network Analysis

5.1 Motivation

Network theoretical approaches for brain image analysis rely on the definition of edges and nodes in order to generate graphs. As mentioned in section 3.7.1, in adults these nodes may be defined as brain regions (or parcels), which are commonly assumed to be functionally coherent or anatomically correspondent across subjects. However, recent studies have proposed the use of multi-granular parcellation methods, where the number of regions can be varied (see for example [100]). In particular in neonates, the lack of a standard parcellation and the unknown (and possibly varying) number of regions in the developing brain strongly motivates the use of random parcellation approaches across scales (see section 3.7.1).

Changes in global network measures have served as a basis to compare networks, however, the dependence on the network size makes quantitative comparisons of such measures across studies difficult (section 3.7.8). Figure 5.1 shows this dependence for betweenness centrality as the number of regions varies over a range of 100-550 regions for two subjects, each scanned at 31 weeks post menstrual age (PMA) and 41 weeks PMA.

Figure 5.1 demonstrates potential pitfalls, when the number of region dependence is ignored. It suggests that determining which subject or which time point has the higher value for betweenness centrality is dependent on the network size. A possible approach for trying to eliminate such dependence is by normalising a measure obtained from an observed network with a network measure gained from a randomised surrogate network (see chapter 4). How-

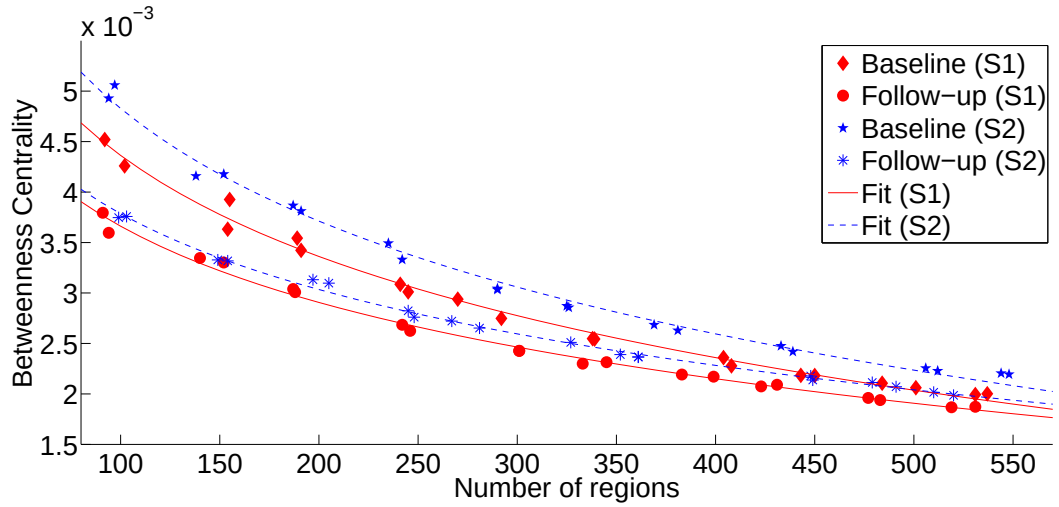

Figure 5.1: Betweenness centrality taken from multiple brain networks defined over a range of 100-550 regions/nodes for two subjects S1 and S2, each with a baseline scan ($\sim$ 31 weeks post menstrual age (PMA)) and a follow-up scan ($\sim$ 41 weeks PMA). The fit for each subject at each scan is based on a logarithmic function.

ever, as shown in Figure 5.1, the betweenness centrality of individual subjects at individual time points seem to have a different behaviour as the scale on which they are calculated is varied [128]. This might reflect a change in network topology, as different types of networks exhibit different behaviour (see section 7.3). Additionally, a possible change in network topology raises the question of whether normalisation, when using the same null-model for each subject, is suitable to eliminate a network's dependence on the scale (see chapter 4). These aspects show the importance of analysing networks over multiple scales and further raises the question of whether these differences can be used to distinguish between groups in a network analysis.

The idea of investigating brain connectivity across scales has gained more attention in recent years (see section 3.7.8). Multi-scale studies try to either find representative connectivity matrices over multiple scales [31, 76] or analyse multiple networks individually to confirm that results are stable over various scales [53, 176, 179]. However, these studies only investigate predefined scales of parcellations and do not characterise the changes in network measures as a function of scale (see section 3.7.8). Furthermore it has been suggested that brain networks undergo basic topological changes, such as subtle randomisation, and that these changes may be indicative of disease where structural changes are likely to occur, for example in schizophrenia [122]. Significant structural changes which are likely to be reflected in the brain's structural

network topology also occur during mid to late gestation (see section 2.1), raising the question of how to quantify such change.

This chapter proposes the use of a multi-scale framework for commonly used network measures in order to describe changes in the developing brain. This form of multi-scale analysis characterises networks by the *dependence* of their measures on the number of regions. It is shown that certain changes in structural brain networks can be investigated independently of a specific parcellation of the brain by describing the dependence of the network measures over varying numbers of regions. Applying the framework to serial dMRI data acquired from preterm subjects, where the subjects were scanned after birth and at term equivalent age, as well as a healthy control group, its potential to differentiate between groups is demonstrated. Moreover, the proposed framework allows the characterisation of changes in early development without the bias due to the number of regions, employing both parametric and non-parametric comparisons.

5.2 Methods and Materials

5.2.1 Subject and Image Data

Baseline (B) and follow-up scan (F) of the preterm dataset, as well as the term control cohort (Con) were used for this analysis (see section 2.3). For each scan, random parcellations $\Pi_{r,s}$ of the cortex at multiple scales ($s \approx 100, 150, ..., 550$) with two samples at each scale ($r \in [1, 2]$) are generated, where regions within a segmentation are kept to an approximately equal size and the size is varied across segmentations. Poisson disk sampling is particularly useful for this task, as it allows distinct parcellations across a large number of regions to be readily generated and produces comparable results at the atlas scale (see section 4.1.1). Networks were then estimated as described in section 4.2.1.

5.2.2 Network measures

This analysis focuses on three types of weighted network measures, commonly thought to describe local segregation, global integration and the prevalence of important nodes (see chapter 3). Table 5.1 broadly subdivides the measures investigated in this chapter into these categories. The measures were calculated using the Brain Connectivity Toolbox[1] [121].

[1]BCT, `http://www.brain-connectivity-toolbox.net`

Table 5.1: Categories of investigated network measures.

Category	**Measure**
Local segregation	Clustering coefficient (C), Transitivity (T), Modularity (Q)
Global integration	Characteristic path-length (λ), Efficiency (E), Diameter (dia), Eccentricity (ecc), Degree (k)
Node importance	Betweenness centrality (BC)

5.2.3 Multi-scale analysis

The multi-scale analysis begins by estimating weighted structural networks, based on the tractography and dMRI data for each subject and each parcellation (see section 2.2.2). Subsequently, global network measures are calculated in these weighted networks (see Table 5.1), which provide connectivity information at a variety of different scales. In the following, the complete set of values for a measure at the different scales for an individual scan will be referred to as a 'trajectory'. Examples of these trajectories are given by Figure 5.1. In order to characterise differences between subjects, trajectories may be compared using non-parametric and parametric approaches. The multi-scale framework is illustrated in Figure 5.2.

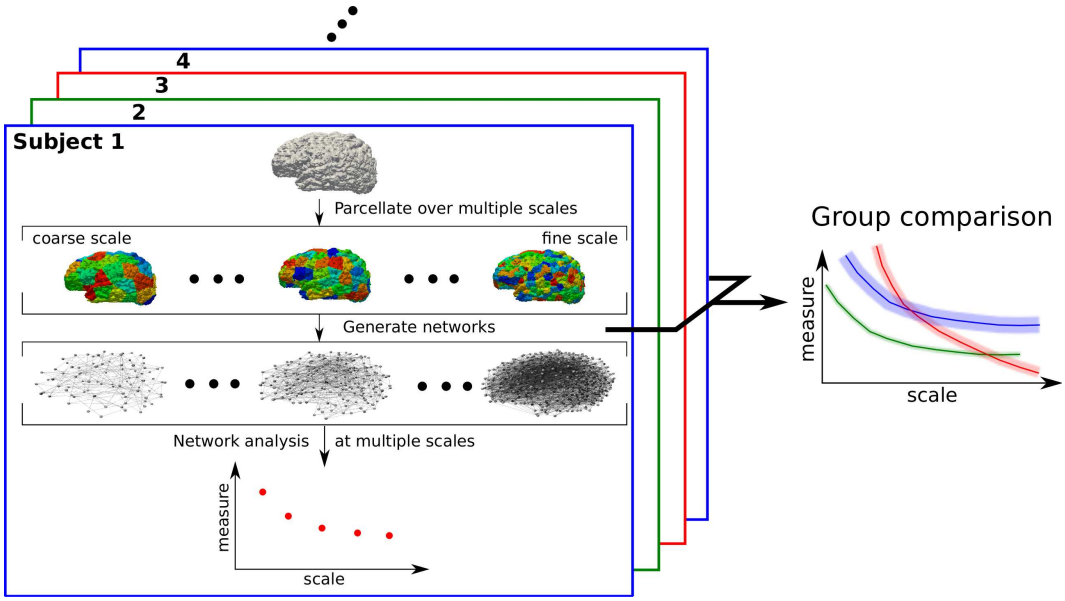

Figure 5.2: A framework for multi-scale analysis. Brain images are parcellated at multiple scales from a coarse (low number of regions) to a fine scale (high number of regions). Structural networks are estimated based on the subject's dMRI data and subsequent network measures are calculated across scales to give a trajectory for the subject. After repeating this for all subjects the trajectories can be used in a group level analysis.

Non-parametric comparison

Non-parametric comparisons use features of the trajectories directly, which can then be used for group analysis. For each network measure (see Table 5.1), the set of trajectory features, given by Table 5.2, consists of the sum (S) and standard deviations (σ) of the network measure and its first (d) and second (d^2) derivative, as well as the maximum value (max), the curvature of the trajectory (c) and the arc-length (a). However, due to the random parcellation process, not every subject has parcellations at the same scale. In order to compensate for potential biases due to these differences, the calculated trajectory values are linearly interpolated onto a regular grid at numbers of regions from 125 to 500 in steps of 25. After calculating the trajectory features a multivariate analysis of variance (MANOVA) is applied for group comparison.

Table 5.2: Trajectory features for non-parametric comparison. These features were calculated for each measure and subsequently used for group comparison.

Feature	**Description**
S	Sum of trajectory values
S_d	Sum of first derivative of trajectory values
S_{d^2}	Sum of second derivative of trajectory values
σ	Standard deviation of trajectory values
σ_d	Standard deviation of first derivative of trajectory values
σ_{d^2}	Standard deviation of second derivative of trajectory values
c	Curvature
a	Arclength
max	Maximum of trajectory values

Parametric comparison

Parametric comparisons can be achieved by fitting a model to the trajectory. This approach can readily accommodate different choices of models, which can retrospectively be evaluated based on the quality of fit. The function

$$m(n) = a_m \cdot \log(n) + b_m \tag{5.1}$$

was found to be appropriate for describing the trajectory of each measure, where $m(n)$ is a network measure calculated for a set of graphs, with varying numbers of nodes n. In this case a_m and b_m are the model parameters for measure m that can be estimated by standard fitting algorithms. Instead of using the network measures for a subject directly, parameters a_m and b_m can

serve as summary features, characterising a subjects network measures over all scales. This leads to a set of model parameters a_m and b_m, which are then used as multi-scale features for subsequent group level analysis.

Moreover, utilising the results of the parametric comparison allows the investigation of the consistency of differences in network measures across scales. This can be done by inquiring about intersections between trajectories from each scan and each group for each network measure. If, for a given pair of scans, i and j, the conditions

$$b_m^j < b_m^i \qquad \text{and} \qquad a_m^i < a_m^j. \tag{5.2}$$

are satisfied, then the measure trajectories for this pair intersect for a positive number of nodes. This is illustrated in Figure 5.3.

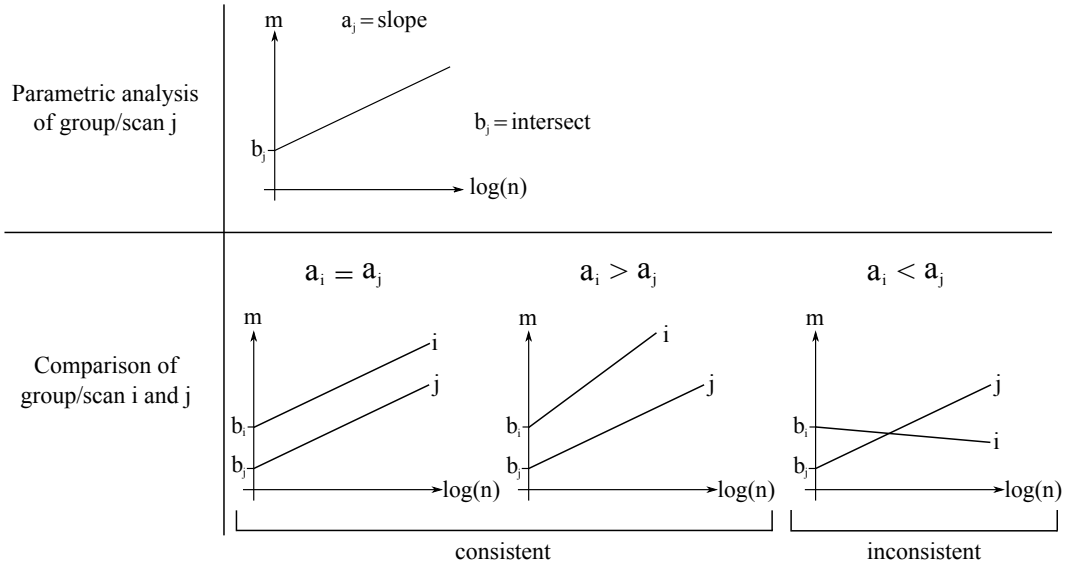

Figure 5.3: Illustration of consistency condition. Under the assumption that the number of nodes n is nonnegative, one can differentiate between the cases of $a_i = a_j$, $a_i > a_j$ and $a_i < a_j$. For $a_i \geq a_j$ group/scan i returns a measure $m_i > m_j$ for all nodal scales n. For $a_i < a_j$, however, the relationship between m_i and m_j is dependent on n.

In terms of single scale analysis this means that it is possible to find two scales for which comparisons show opposing results. Therefore this result is described as *inconsistent*, as it can subsequently lead to opposing results between studies. If these conditions are not satisfied, the result is called *consistent*, i.e. the comparison between scans/groups will stay the same across scales.

5.3 Results

5.3.1 Non-Parametric Comparison

Before applying the proposed non-parametric comparison to the data, global network measures are estimated for the regular spaced sequence of regions between 125 and 500 with a spacing of 25 using linear interpolation. Trajectory features, as described in Table 5.2, are then calculated, thereby generating sets of nine features per network measure and subject. Some of the features used to perform MANOVA are correlated. Figure 5.4 shows, for example, the relationships between the trajectory features, as well as their individual distributions for all groups investigated in case of betweenness centrality.

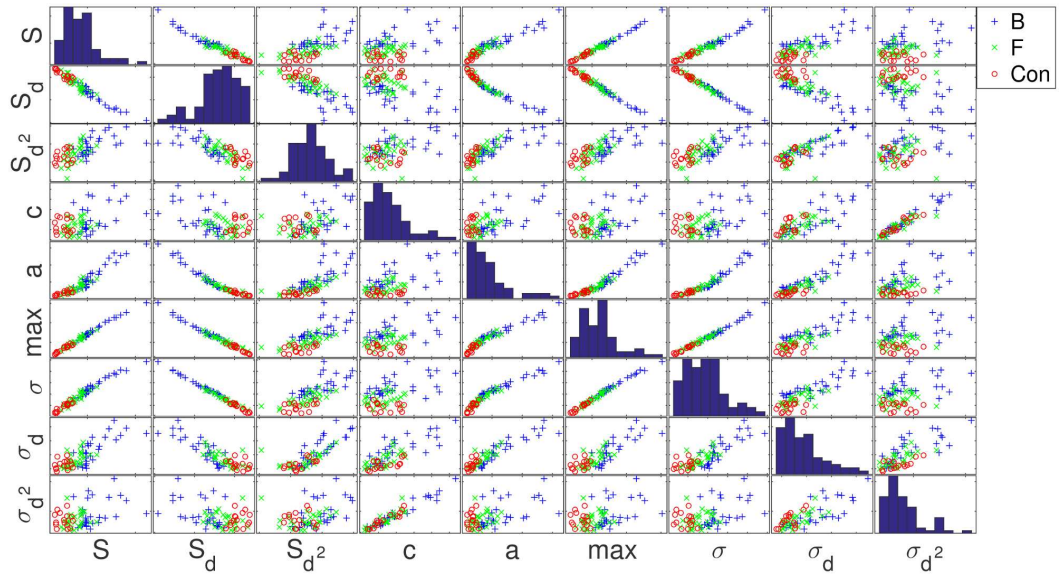

Figure 5.4: Scatter plots of the trajectory features taken from trajectories of all subjects plotted against another for betweenness centrality. The diagonal shows the histograms of each feature.

One of the assumptions of MANOVA is that the dependent variables investigated exhibit medium correlations among each other. In order to ensure this, the average absolute value of the correlation among the trajectory features was investigated, where the average was taken over all network measures. The average correlations are given in Table 5.3 and show that some features are strongly correlated, necessitating the definition of a subset as input for MANOVA.

A subset of trajectory features was determined for which the absolute value of the inter-measure correlation was between 0.3 and 0.9. One possible combi-

Table 5.3: Average absolute value of the inter-measure correlation for trajectory features, where the average was taken over all network measures.

	$\mathbf{S_d}$	$\mathbf{S_{d^2}}$	**c**	**a**	**m**	$\boldsymbol{\sigma}$	$\boldsymbol{\sigma}_d$	$\boldsymbol{\sigma}_{d^2}$
S	0.71	0.40	0.62	0.68	0.98	0.79	0.70	0.55
	$\mathbf{S_d}$	0.46	0.53	0.74	0.77	0.93	0.67	0.48
		$\mathbf{S_{d^2}}$	0.28	0.44	0.42	0.40	0.46	0.28
			c	0.70	0.66	0.62	0.81	0.93
				a	0.75	0.83	0.94	0.78
					m	0.85	0.76	0.59
						$\boldsymbol{\sigma}$	0.76	0.58
							$\boldsymbol{\sigma}_d$	0.86

nation of features is given by (S, S_d, c, a). This subset was subsequently used as input for MANOVA, where Pillai's trace was evaluated in each case to determine statistical significance. All tests showed $p < 0.001$, indicating that the differences among the three groups are highly statistically significant with respect to every network measure.

Stability assessment

The stability of the non-parametric approach was assessed by recalculating the p-values 100 times using subsets of the original data for re-estimating the trajectory features. The data for each subject consists of parcellations $\Pi_{r,s}$, where $r \in [1, 2]$ represents the index to the samples of the repeated parcellation at each of the ten target scales $s \approx 100, 150, ..., 550$. This allowed the definition of subsets M_i. Each M_i consists of a set of 10 data points, one for each scale, with r chosen randomly from $\{1, 2\}$. Each subject can then be represented by the trajectory features of its subset M_i, which is then used as input for MANOVA. This was repeated for $i = 1, \ldots, 100$. All p-values were less than 0.001, suggesting that the group comparison remains highly statistically significant. Taking these results into account suggests that the approach does not rely on any given parcellation directly and that no parcellation is favoured over any other. This suggests that the non- parametric comparison is parcellation independent.

5.3.2 Parametric Comparison

The differences between the groups were further investigated by applying the proposed parametric comparison to the described dataset. This required fitting the model given by equation 5.1 to the global network measures, which allowed

an estimation of the parameters a_m and b_m for the baseline and follow-up scan of the preterm group, as well as the control group. The combined results are shown in Figure 5.5.

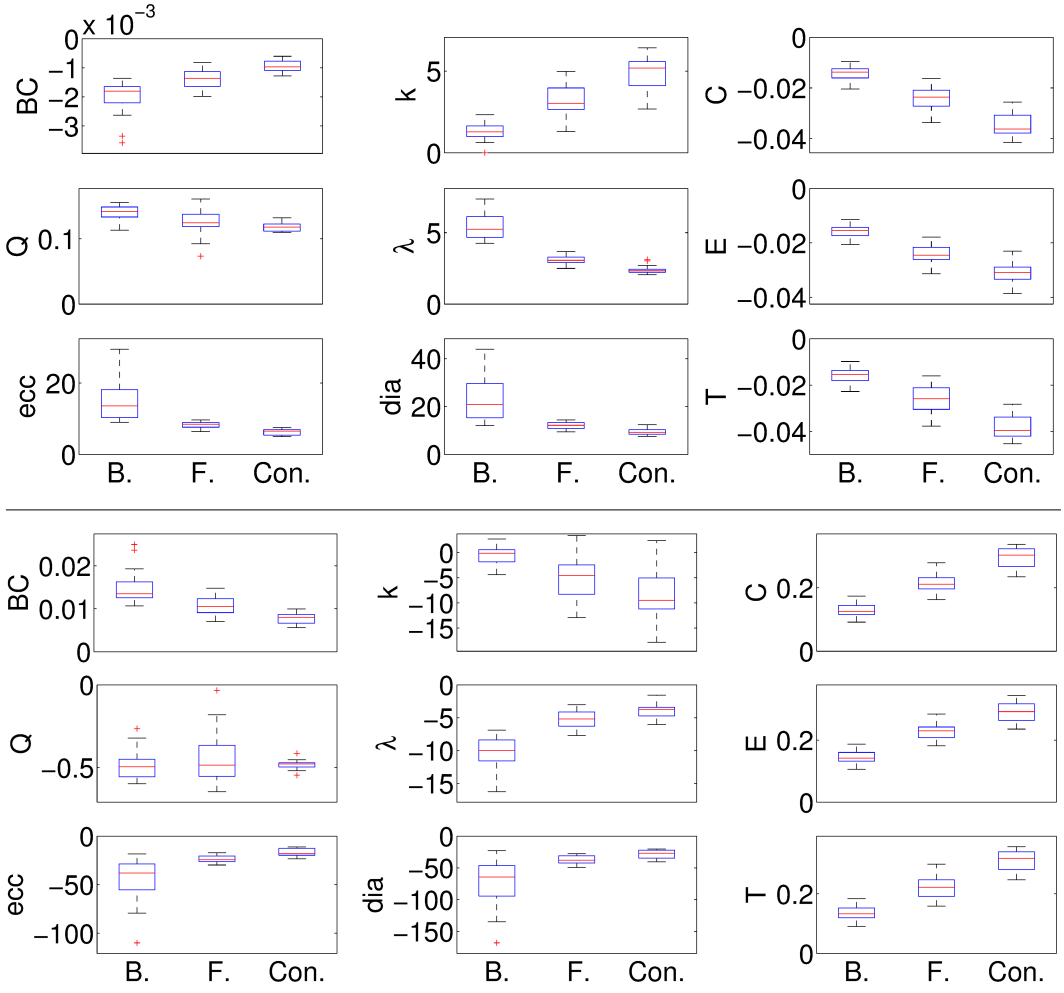

Figure 5.5: Box-plots for the model parameters a_m (top) and b_m (bottom) for each measure for the baseline (B), follow-up (F) and control (Con) group. Values represent the group at each scan, where the subjects of the baseline, follow-up and control group were scanned at 30.8±1.9, 41.2±1.2 and 41.9±1.7 weeks PMA, correspondingly.

Paired and two-sample t-tests were performed for each combination of the groups with each parameter, where paired t-tests were used for the results of the baseline and follow-up scan of the preterm group. All p-values were below $p < 10^{-4}$, except for parameter b_m in case of degree ($p < 0.05$ for follow-up and control), characteristic path-length ($p < 0.001$ for follow-up and control) and modularity Q (not statistically significant for all combinations). In case of modularity Q, differences in parameter a_Q were found not statistically significant when comparing the follow-up and control groups, but had a

p-value below $p < 0.01$, when comparing the baseline and follow-up scans of the preterm group.

In order to assess the quality of the fit, the coefficient of determination R^2 was calculated for each measure and each subject. $R^2 \in [0, 1]$ represents the amount of variation in the data explained by a given model. The results are given in Table 5.4 and show that the logarithmic model accounts on average for 96% of the variation within the data for a trajectory, where the average was taken over all subjects and all measures.

Table 5.4: Coefficients of determination R^2 and corresponding interquartile range IQR after model fitting for each network measure averaged over all subjects.

	BC	k	C	Q	λ	E	ecc	dia	T
R^2	0.98	0.91	0.99	0.99	0.98	0.99	0.90	0.88	0.99
IQR	0.01	0.07	0.01	0.01	0.01	0.00	0.07	0.06	0.00

Stability assessment

The stability of the parameter estimation can be assessed by using a sampling approach similar to the one used for the non-parametric comparison. Considering that there are two samples at each of the ten scales ($\approx 100, 150, ..., 550$), parameters a_m and b_m were estimated for all 2^{10} combinations that use one sample at each scale, i.e. a total of ten data points per fit. This analysis creates parameter distributions for a_m and b_m for each subject. As an example, the individual distributions for betweenness centrality are shown in Figure 5.6, where each box corresponds to the parameter distribution of one subject. Each group was ordered with respect to their age, plotting the youngest subject of the group to the left and the oldest to the right.

For each group the variance within each group was calculated by using the mean values of each subjects' distribution, as well as the average within subject variance of all subjects belonging to the group. The results for each group were summarised by calculating the ratio of the average within subject variance to the within group variance and are shown in Table 5.5.

On average the ratio was determined to be 0.08 ± 0.07 and 0.12 ± 0.11 for parameters a_m and b_m, respectively, where the average was taken over all groups and all measures investigated. This suggests that the uncertainty of parameters a_m and b_m of individual subjects from sampling are small compared to their variance within the group, suggesting that the parametric analysis at

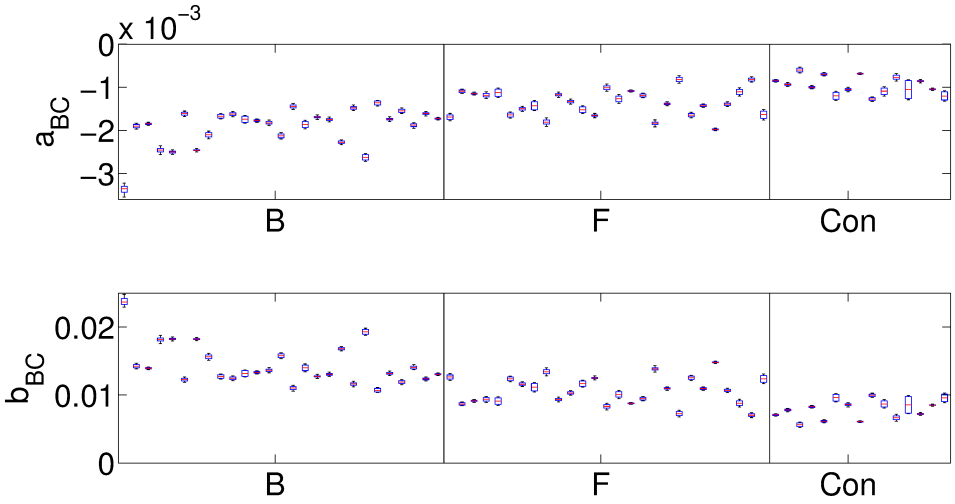

Figure 5.6: Parameter distributions for all subjects in case of betweenness centrality based on a leave-N-out approach. At each scale ($s \approx 100, 150, ..., 550$) one of two sample points was selected for fitting, resulting in 2^{10} possible combinations. Parameters a_m and b_m were then estimated for each of the combination resulting in a parameter distribution for each parameter and each subject. Each box represents the parameter distribution of an individual subject and the subjects within the groups were sorted ascending with age (left to right).

the group level is to a certain extent independent of individual parcellations. Note that for eccentricity (ecc) and diameter (dia) the within subject to within group ratio are relatively large compared to other measures (0.36 ± 0.04 and 0.54 ± 0.06 for parameters a_m and b_m, respectively). However, both measures are sensitive to small disturbances in the network structure (see section 3.3), which are to be expected using random parcellations. The effect might be mitigated by using more than ten data-points when calculating the fitting parameters.

Consistency assessment

With the results from the parameter estimation for each group, as shown in Figure 5.5, it is possible to evaluate the consistency of the differences between groups by using the groupwise averaged values for a_m and b_m. Applying the consistency test based on the conditions 5.2 to the groups investigated suggests that separate single scale analyses may be *inconsistent* for all measures and all combinations of groups. This means that it might be possible to find two scales of parcellations at which the determined network measure differences in a group analysis will provide opposing results, emphasising the need for multi-

Table 5.5: Ratio of average within subject variance to within group variance for parameters a_m (top) and b_m (bottom) for all measures and each group, where the average was taken over all subjects within each group.

a	BC	k	C	Q	λ	E	ecc	dia	T
Baseline	0.01	0.02	0.02	0.09	0.02	0.02	0.06	0.06	0.02
Follow-up	0.03	0.01	0.01	0.02	0.03	0.02	0.42	0.35	0.01
Control	0.12	0.02	0.01	0.10	0.05	0.02	0.34	0.32	0.01

b	BC	k	C	Q	λ	E	ecc	dia	T
Baseline	0.01	0.04	0.01	0.06	0.08	0.01	0.09	0.10	0.01
Follow-up	0.02	0.02	0.01	0.01	0.06	0.01	0.62	0.48	0.01
Control	0.09	0.04	0.01	0.16	0.10	0.01	0.55	0.52	0.01

scale analyses, such as the ones described in this and the following chapter.

5.4 Conclusion

This work introduced a multi-scale framework for analysing network measures which can be used to characterise changes in brain networks, helping to reduce the bias due to a parcellation scale. Network analyses commonly estimate measures at a single scale when comparing subjects or groups, implicitly assuming that the network measure is constant over a variety of number of regions. Instead of comparing network measures calculated at a single scale, i.e. specific number of regions, the framework allows for analyses that use a parametric and a non-parametric approach.

Applying the non-parametric analysis using MANOVA showed the potential to differentiate between groups using a set of trajectory features. The inclusion of other measures may furthermore improve the ability of the multi-scale framework to differentiate between the groups, if required. One challenge using the non-parametric approach lies in the assumption of smoothness for the measure trajectories, which is required by the linear interpolation of the global network measures to generate a regular spaced sampling. Visually inspecting the behaviour of the individual trajectories for each subject suggests that this is an appropriate assumption. Uncertainties due to the interpolation can be prevented by using the same number of regions for each subject, however, this is more time consuming due to the random parcellation approach, which often needs multiple executions before the target number is reached (see section 3.7.1). Future developments in regards to multi-granular brain atlases might help to alleviate this challenge and reduce the uncertainty due to the

interpolation.

The parametric approach allows for an analysis in two ways using a logarithmic model. First, the offset parameter b_m can be viewed in a similar way to traditional global network measure analyses, assuming $a_m = 0$, however, the benefit of this approach lies in the independence to changes in parcellation scale. The second model parameter, a_m, on the other hand may provide insight into the underlying network type. Results presented by Van Wijk et al. [164] show graphs describing the changes in clustering coefficient and characteristic path-length in random, small-world and lattice networks, when the number of nodes is altered. These graphs indicate that the trajectories of different network topologies exhibit different shapes (see section 7.3), which may be described by parameter a_m in the framework and subsequently help to identify changes in network topology. A more comprehensive analysis of the model parameters will be the aim of future work and is outlined in section 7.3.

Investigating the stability of the proposed multi-scale framework showed that it offers reproducible results when varying the parcellations used for estimating the model parameters, making the approach effectively parcellation independent. Furthermore, by analysing the data using the consistency conditions from equation 5.2, the results suggest that it might be possible to produce inconsistent network measure results using single scale analyses in the dataset. This further emphasises the need for a multi-scale framework when analysing brain networks.

Using the presented multi-scale framework on a preterm serial dMRI dataset, as well as a control group, it was possible to show group differences with the non-parametric approach, as well as both parameters of the parametric approach for commonly used network measures. Moreover, the results suggest that the differences in network measure trajectories are indicative of developmental differences in structural brain networks. These developmental differences seem to be dependent on both age and environment, as indicated by the group differences between the baseline and follow-up, as well as the follow-up and control group. In particular the changes in a_m suggest differences in topology, as outlined in section 7.3, indicating that the network type is altered in the preterm group compared to the control group. This agrees with results suggesting that the connectivity pattern of brain networks changes with age [178]. Further investigation is necessary to show in more detail if these changes in the parameters can be used as biomarkers to detect differences in brain networks in development or disease.

Chapter 6

Learning Coarse Scale Information from Fine Scale Networks

6.1 Motivation

Various challenges face the use of global network measures for network analysis. This work already discussed the dependence of measures on the number of nodes in a given network and how it can be reduced using normalisation (chapter 4) or utilised in a multi-scale framework (chapter 5). The latter, however, necessitates the generation of networks at multiple scales, and therefore the execution of multiple tractography steps which can lead to a high computational cost. It would be beneficial to use only a small number of networks, which allows the derivation of multi-scale information for network analysis. One possible approach is to estimate properties at a coarser scale from a fine scale network.

Merging nodes has been investigated in relation to creating random binary networks. Kim et al. [75] and Alava et al. [4], for example, generate random networks based on the preferential attachment model (see section 3.6), allowing for two nodes in the network to merge. Due to the simultaneous introduction of new nodes, however, the size of the network is maintained. Importantly they show that in this model properties, such as a power-law degree distribution and the existence of hubs, are a result of merging nodes, however, they did not use this framework to compare networks over multiple scales. The idea of merging nodes is illustrated in Figure 6.1.

As indicated in Figure 6.1, network properties and measures can change

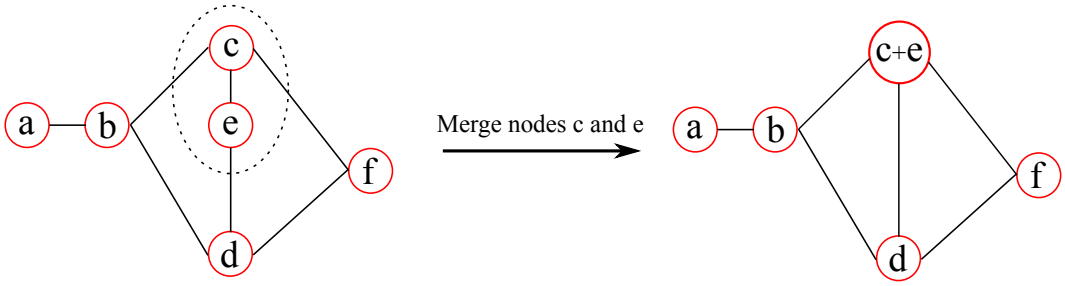

Figure 6.1: Principle of merging nodes, where nodes c and e are merged into a combined node.

after a merge of two nodes. In this network, for example, the average clustering coefficient increases from $C = 0$ to $C \approx 0.53$. Changes also occur for other network measures. By successively merging pairs of nodes, one can create a set of networks with decreasing numbers of nodes. For each of these networks, network measures can be calculated and subsequently collected over the range of regions considered. Additionally, multi-scale analyses, as presented in chapter 5, may be applied to the resulting data.

This chapter proposes the use of a node merger approach in order to collapse a binarised network with a high number of regions to a lower number of regions. A benefit of the approach is the need for only one observed network, from which all lower scale networks can be derived. The approach allows for subjects to be compared over a large number of regions, revealing aspects of the network for which there might be insufficient information at a local scale. The framework's potential in describing changes in network characteristics with age is shown by analysing a serial dMRI dataset of prematurely born infants, scanned after birth and at term equivalent age, as well as a control group scanned at term.

6.2 Methods and Materials

6.2.1 Network measures

This chapter focuses on a set of three network measures commonly thought to describe local segregation, global integration and the prevalence of important nodes (see chapter 3). Table 6.1 broadly subdivides the measures investigated into these categories. The measures were calculated using the *graph-tool* python library[1] [111].

[1]graph-tool, `https://graph-tool.skewed.de`

Table 6.1: Categories of investigated network measures.

Category	**Measure**
Local segregation	Transitivity (T)
Global integration	Efficiency (E)
Node importance	Betweenness centrality (BC)

6.2.2 Network collapse

The proposed approach begins with the binarised and undirected structural network with s nodes, estimated from the tractography of the dMRI data for each subject and Poisson disk sampling. At each step of the node merger a hemisphere and a base node b within that hemisphere are selected randomly. Subsequently the spatial neighbourhood of b, $\mathcal{N}_b$ is determined, i.e. the regions which share a border with b in the parcellated brain image (see Figure 6.2).

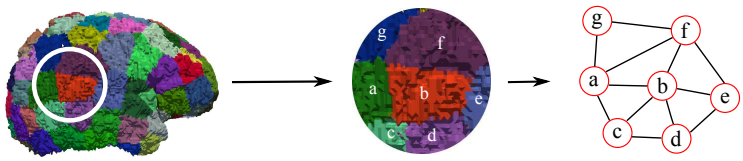

Figure 6.2: Spatial neighbourhood of a node b in a brain parcellation, given by $\mathcal{N}_b = a, c, d, e, f$.

The smallest node from the nodes in $\mathcal{N}_b$ is then picked as the merge partner. This choice is motivated by the principle that smaller nodes are unlikely to occur, when using fewer regions with Poisson disk sampling. The process returns a network of size $s-1$ and serves as a new input to the next node merger step. Edges are determined based on a logical *or* decision and it was enforced that the resulting networks remain simple, i.e. without multiple edges or self-loops. This provides a number of networks at each scale from the original size s down to a user-defined lower limit and thus a number of measures of network connectivity can be derived over all scales for the subject. As this approach relies on the random selection of nodes, the network collapse is repeated for each subject 100 times, resulting in a *distribution* of network measures for each scale and each subject. The framework of the network collapse is shown schematically in Figure 6.3.

In order to simplify comparisons, the trajectory for each subject is defined using the mean network measure of the 100 repetitions at each scale. It should be noted that the variability in network measures increases, the more the generated network size departs from the original size, i.e. as more merge steps

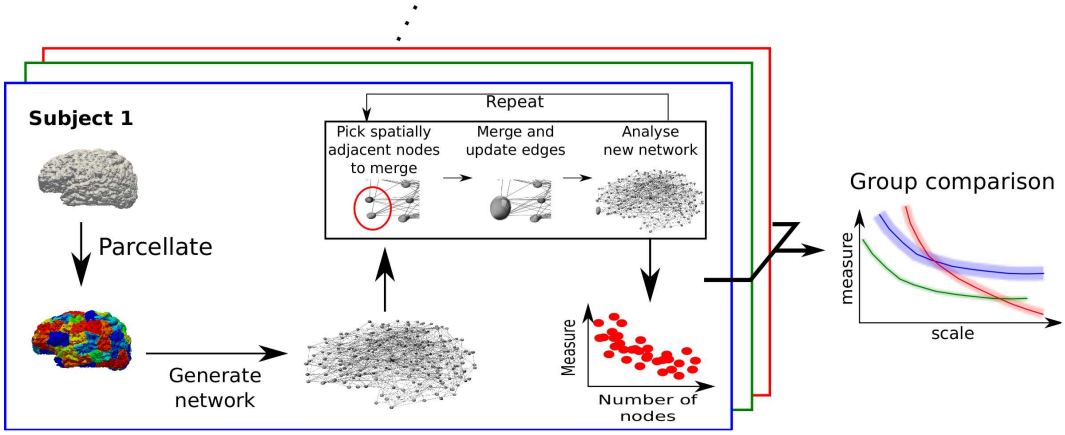

Figure 6.3: Framework for network collapse analysis. Each brain image is parcellated at a high number of regions and the structural network is estimated. Within the structural network two spatially adjacent regions are picked for merging, creating a new network with one node less than the observed network and which serves as new input to the node merger. This process is repeated until the user specified lowest number of nodes is reached.

are carried out. This is illustrated in Figure 6.4.

6.2.3 Data

This chapter uses the same data as described in section 5.2.1. These consist of preterm infants scanned shortly after birth (B) and at term equivalent age (F), as well as a control group (Con). For each subject parcellations were created at multiple scales ($s \approx 100, 150, ..., 550$) with two samples at each scale. Additionally one subject was parcellated at five scales below 60 regions, where networks were estimated as described in section 4.2.1.

Additionally the behaviour of synthetic networks is studied, models in which each hemisphere is represented by the surface of half a sphere with a radius and width of 160 and 1 voxels respectively. Each voxel is assigned a value of one and treated as a grey matter voxel for parcellations. The surfaces are subsequently parcellated using Poisson disk sampling with a target number of 500 regions, resulting in a total of 499 regions with average size of 15 voxels. Connectivity is subsequently estimated by connecting each region to its direct spatial neighbours. The graph density is then increased by calculating the shortest path distances in the binarised spatial neighbourhood graph among all regions and connections are added to each region's n-neighbourhood, where n is the number of steps (see for example Figure 6.2, where node g is part of the 2-neighbourhood of node b). This generates two independent lattice networks

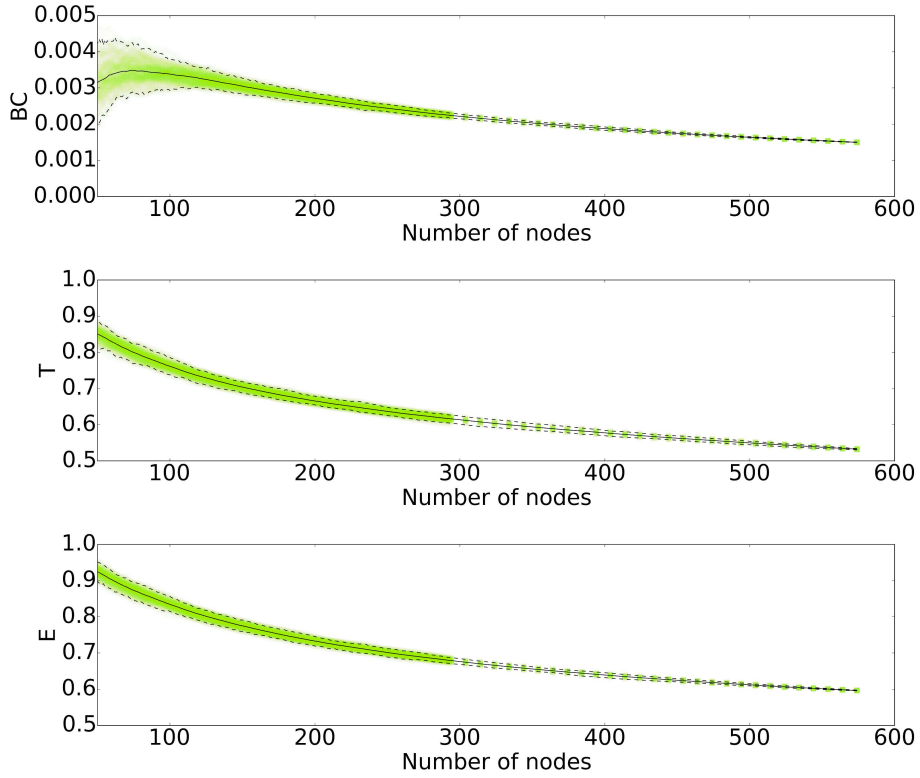

Figure 6.4: Distribution of network measures after successive mergers starting from a 584 node network of one subject. Here, different step-sizes for sampling were used to reduce the computational cost, resulting in gaps at higher number of regions. Each point of the 100 repetitions was assigned an opacity value of 0.01, resulting in a shading of the distribution. The average measure at each scale (solid black line) is used for comparison between subjects. The 5-th and 95-th percentile of the measures are indicated as dashed lines.

for each hemisphere. Subsequently $p\%$ of the existing connections are then randomised, allowing for the existence of long-range connections. In this study the parameters n and p were chosen to be $n \in [2, 3, 4]$ and $p \in [1\%, 10\%, 100\%]$, where the values of p represent lattice-like, small-world and Erdös-Rényi (ER) random network topologies. The principle of generating synthetic networks is shown in Figure 6.5.

6.3 Results

6.3.1 Network Collapse in Brain Networks

In order to assess the consistency of the framework with tractography results, each subject's brain image was parcellated 20 times with regions ranging from

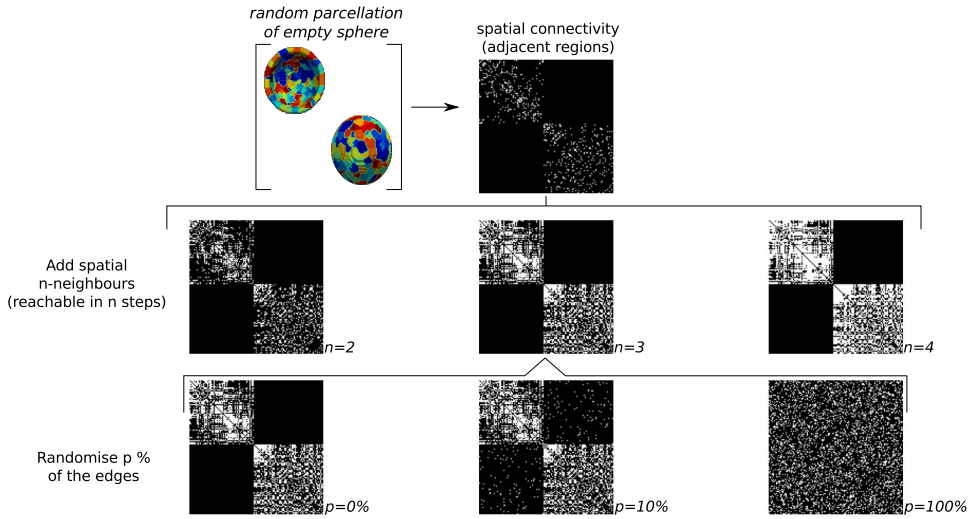

Figure 6.5: A framework to generate synthetic networks. Two surfaces of half spheres, each representing a brain hemisphere, are randomly parcellated using Poisson disk sampling. Spatial adjacency serves as an initial connectivity profile, representing a 3D lattice network. Density may be increased by adding edges to regions which are n steps away from a given region, calculated using the spatial adjacency. Subsequently p% of the edges are randomised.

around 100 to 550 regions and the network measures shown in Table 6.1 were calculated at each scale. In addition, starting from the network with the highest number of regions in the parcellations used for tractographic analysis, the proposed network collapse was applied and 100 data points at each number of regions considered were generated for each subject. To reduce computational cost, a variable step size was used, i.e. the number of mergers that were executed before network measures were calculated. In general, there was less variance at higher numbers of regions and subsequently network measures were calculated after every 10 mergers, until the resulting network had fewer than 300 regions, where the step size was set to 1. The results derived from the network collapse were then compared with those calculated using tractography at the parcellated scales. Figure 6.6 shows the results of the collapse for one subject, compared to results based on tractography, and indicates good agreement between measures estimated using the collapse framework and those obtained from tractography.

All subjects showed similar trends between measures derived from the collapse framework and tractographic computation, suggesting that one network obtained from tractography at a high number of regions can be used to derive measures for fewer numbers of regions. In the following the results based on

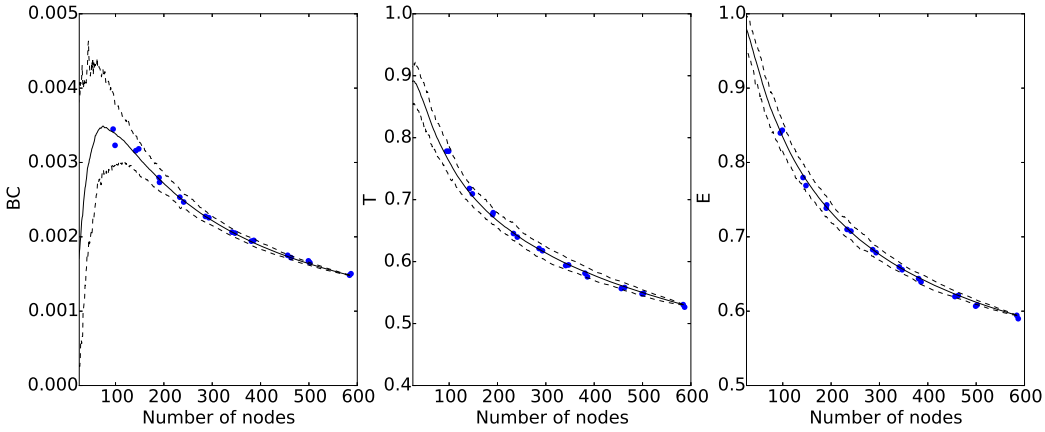

Figure 6.6: Results based on the network collapse (black lines) in comparison to tractography (blue circles). The results of the collapse are summarised by the mean (solid line) and 5-th and 95-th percentile (dashed lines) of the network measures, respectively.

the 100 executions of the network collapse for each network measure at each scale will be summarised by its average, as illustrated in Figure 6.4. Figure 6.7 shows the average measure trajectories for all subjects investigated.

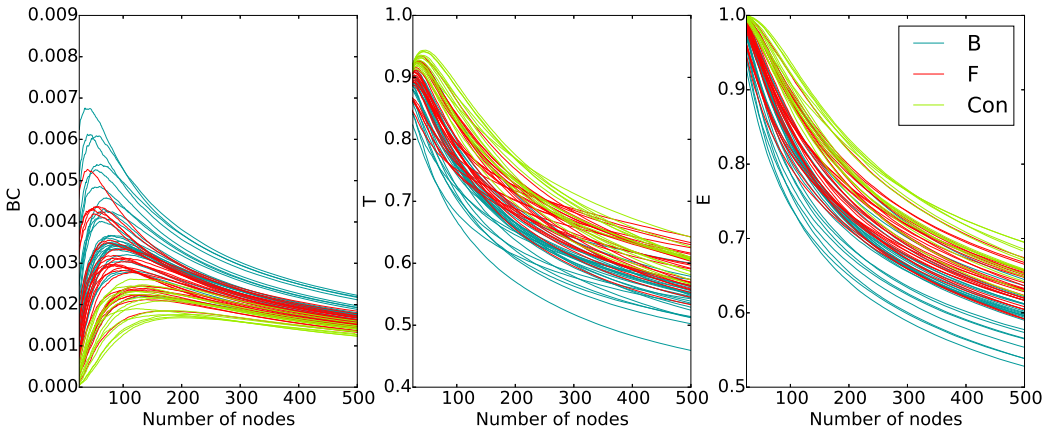

Figure 6.7: Average network measure trajectories for each measure and each subject derived using the node merger. The colours represent the preterm cohort scanned at birth (B), term equivalent age (F) and the control group (Con).

The results show that there are differences between all groups, and results for the follow-up scan of the preterm cohort generally lie between the preterm baseline (B) scan and the control group data. Applying a non-parametric multi-scale comparison, as described in chapter 5, indicates statistically significant differences between the three groups ($p < 0.001$). The per group

average curves with corresponding standard deviations ($\pm 1 std$) are shown in Figure 6.8.

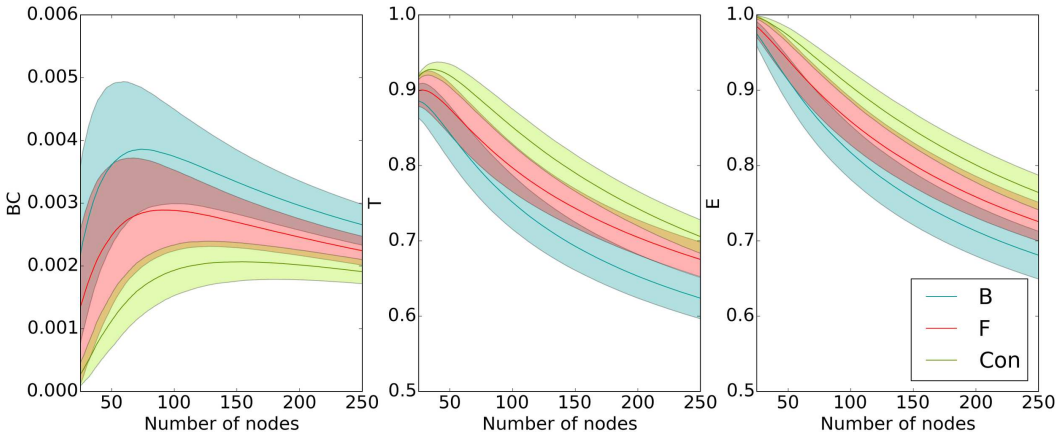

Figure 6.8: Group-wise average trajectories for each measure with corresponding standard deviation ($\pm 1 std$) for the baseline (B) and follow-up (F) scan of the preterm cohort, as well as the control group (Con).

Figure 6.8 indicates the presence of a peak for betweenness centrality. The existence of a peak in betweenness centrality in the tractography based results is investigated by additionally parcellating one subject at five scales below 60 regions. Figure 6.9 shows the comparison of results based on tractography with the results of the network collapse at scales between 25 and 300 regions.

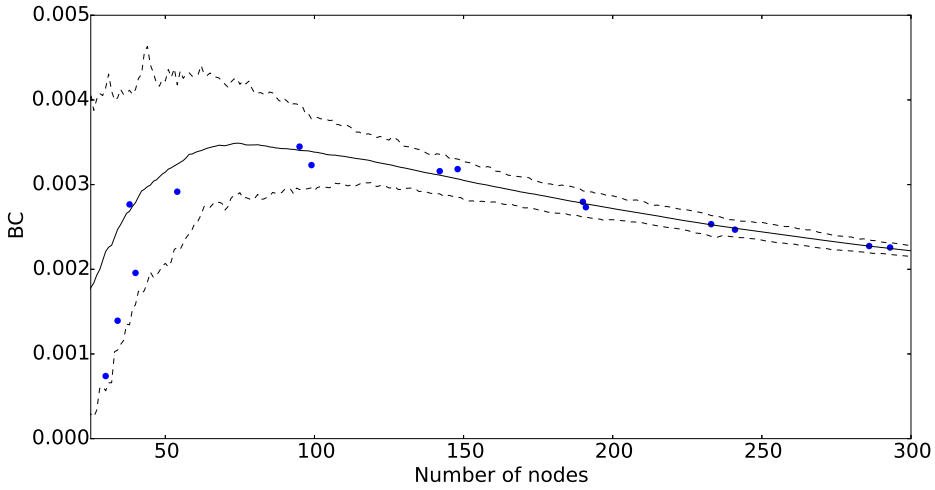

Figure 6.9: Detailed comparison between tractograhy based results and network collapse for betweenness centrality at scales between 25 and 300 regions. Both tractography and network collapse results indicate a peak in betweenness centrality.

6.3.2 Network Collapse in Synthetic Networks

In order to investigate the behaviour of the three network measures, synthetic networks are created to represent lattice, small-world and random topology at three different densities (see section 6.2.3). Figure 6.10 shows the results of applying the collapse framework to these networks with 100 repetitions each.

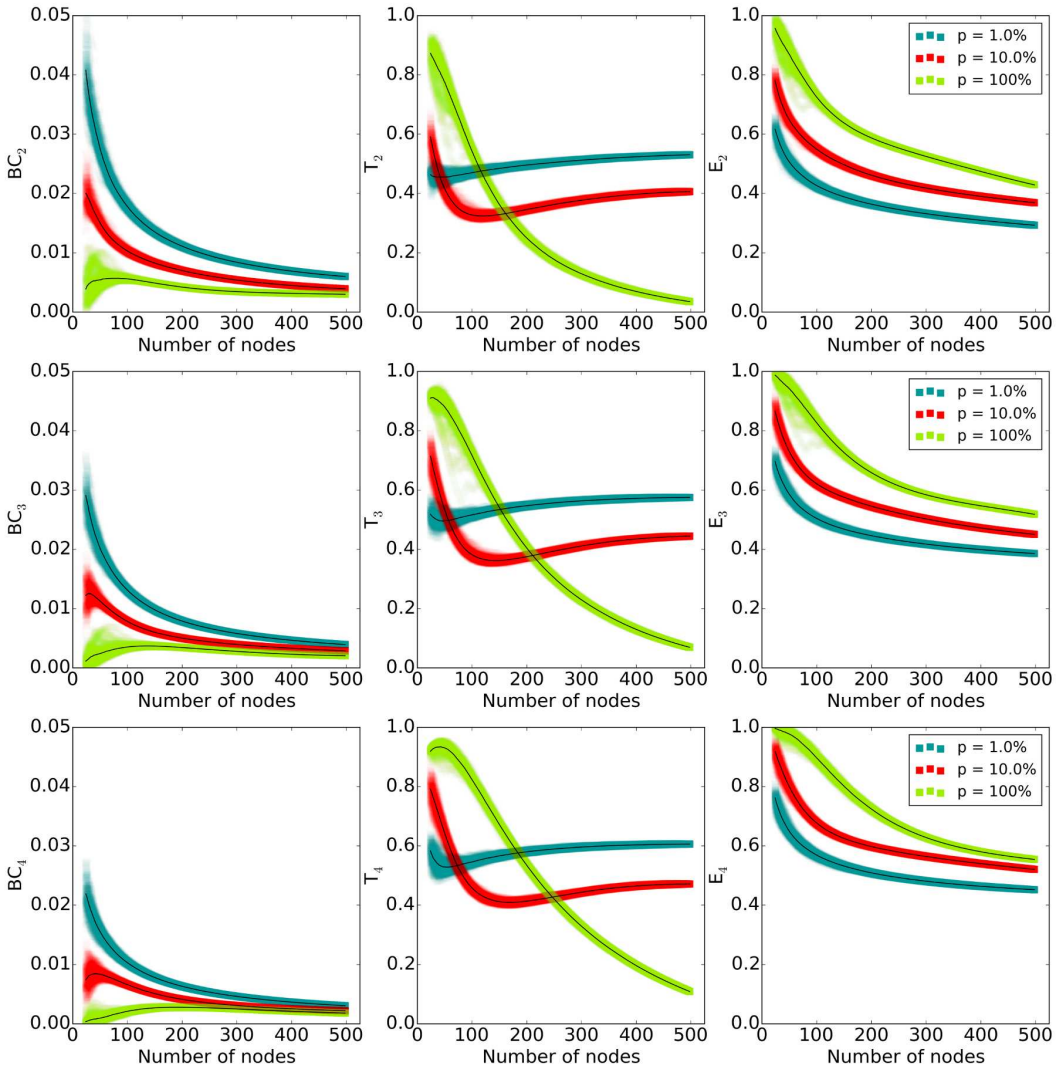

Figure 6.10: Results of applying the collapse framework to synthetic networks representing lattice, small-world and random topology at three different densities. The subscript at each network measure indicates the order of spatial neighbourhood connected before $p\%$ of the edges were randomised.

6.4 Discussion

6.4.1 Network Collapse in Brain Networks

The results presented in Figure 6.8 suggest that, on average, the control group exhibits lower global betweenness centrality, higher transitivity and higher efficiency than the other groups. Furthermore, when comparing the preterm baseline scan and the control group, it indicates over all scales that the brain may develop to reduce the average betweenness centrality, while increasing transitivity and efficiency. This development seems to be altered as an effect of premature birth, as shown when comparing the follow-up scan of the preterm cohort and control group.

One striking feature in Figure 6.8 and Figure 6.9 is the existence of maxima for the trajectories of betweenness centrality. Comparing the three groupwise trajectories, the maxima occur at different numbers of nodes for each group. One possible reason for this behaviour could be an effect of sampling. Given a network of size s_o, it is possible to represent this network with $s_{over} > s_o$ or $s_{under} < s_o$ nodes. This representation can be interpreted as an over- or undersampling of the network. The idea of sampling a network is represented in Figure 6.11, where possible sampling schemes of a given topology (middle) at a lower and higher number of nodes are shown, assuming that each subunit of a region shares the connectivity profile of the region itself (see Figure 6.12).

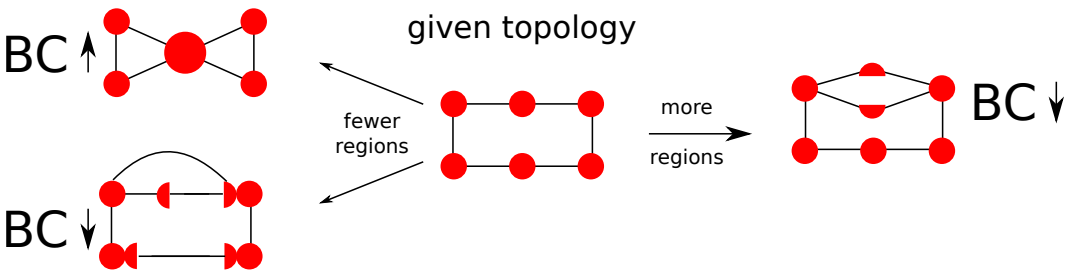

Figure 6.11: Possible effects on betweenness centrality of over- and undersampling, i.e. changing the number of nodes used to represent a network. Given a network (middle) one can over-/undersample this network by increasing/reducing the number of nodes or regions. Subsequently the average value of betweenness centrality will change, with a general decrease, for higher numbers of nodes and a possible increase or decrease for lower numbers of nodes.

This suggests a possible reason for the maxima in the case of betweenness centrality. In order to assess this effect, seven synthetic "ground truth" networks, as shown in Figure 6.5, were created at scales between 90 and 180 nodes

and oversampled the networks at scales of 499 and 762 nodes. In order to oversample these networks, it was assumed that every voxel within a region shares the region's connectivity profile. The principle of oversampling is illustrated in Figure 6.12.

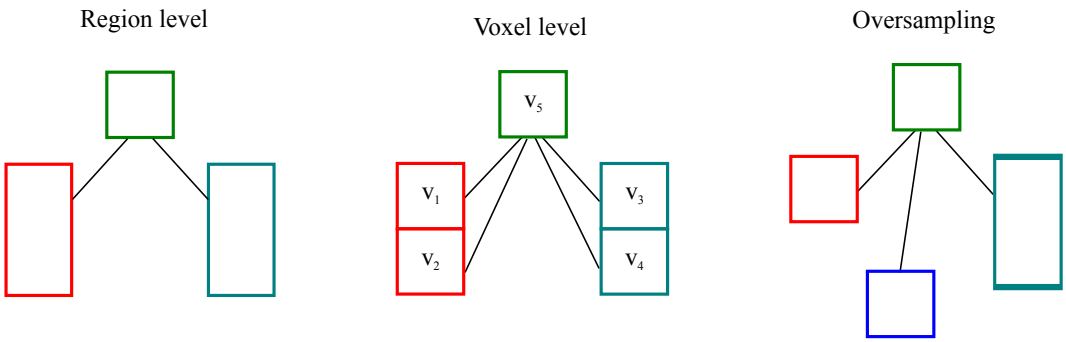

Figure 6.12: Principle of oversampling a network (left), where the region shown in red is represented by two independent regions in the oversampled network (right). It assumes that each voxel v_i in a region shares the global connectivity profile of the region itself and does not include intraregional connections. This approach can be used to model oversampling in synthetic networks.

Subsequently the node merger is used in order to collapse the oversampled networks to a number of nodes below the "ground truth" network size. This procedure is repeated 100 times and the location of the peak of the average collapse trajectory is recorded. Figure 6.13 shows the results of plotting the number of nodes of the ground truth against the location of the peak found from the network collapse.

The results show a clear correlation between the number of nodes of the ground truth and the location of the peak. This means that it might be possible to infer a native scale of the network by investigating the behaviour of betweenness centrality over multiple scales. Many other factors, however, may contribute to the shape of the curves as seen in Figure 6.8, such as network density and network type. The next section investigates these effects further based on synthetic networks which are thought to represent lattice, small-world and random topology at a variety of densities.

6.4.2 Network Collapse in Synthetic Networks

The results in Figure 6.10 show that the average betweenness centrality, for high densities and high number of regions is almost equal in all synthetic network types. The differences between the individual models is only apparent at lower scales. However, it supports the intuition that completely random

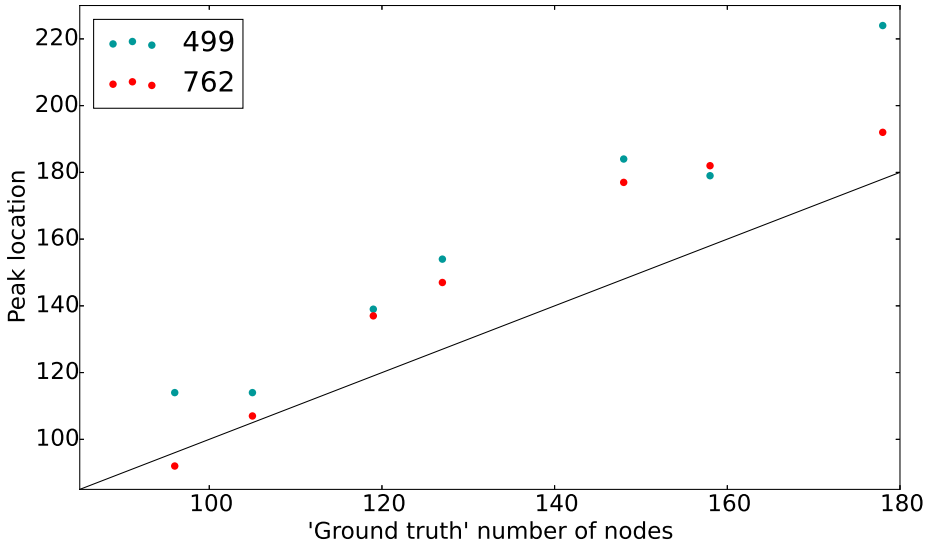

Figure 6.13: Plot of the number of regions on which the ground truth was defined against the location of the peak determined by the network collapse for betweenness centrality. The black line indicates the line of equality between the peak location and the ground truth.

networks ($p = 100\%$) will have the lowest prevalence of important nodes. Similarly, efficiency shows the expected behaviour, where lattice-like networks have a lower average efficiency over all scales, compared to small-world and ER random networks.

Transitivity, the global clustering of the network, shows the expected behaviour at the higher scales, where random networks have a low transitivity, whereas the highest value can be found in lattice-like networks. Importantly the results show, that after collapsing the network below 200 regions, the random networks exhibit a higher transitivity than lattice-like or small-world networks. In particular, the random graphs retain high efficiency, resulting in the highest efficiency and highest transitivity of all networks below 100 regions. This further emphasises the importance of taking the scale at which a network is observed into account, as the lower scales effectively correspond to a coarser parcellation scheme and subsequently random graphs could be interpreted as having small-world topology.

The results show that, in case of binarised networks, different network types exhibit different trajectories in their network measures as a function of scale. Consequently, it may be possible to use these trajectories themselves to investigate the type of an observed network in more detail. A possible approach will be outlined in section 7.3.

Furthermore, with respect to the peak for the betweenness centrality, the results shown in Figure 6.10 suggest that it occurs and becomes more pronounced at higher levels of network density and is dependent on the network type, i.e. the percentage of randomisation. This suggests that the peak is not simply a function of the "ground truth" network scale, but that other factors may play a role in the trajectories exhibiting this feature. Consequently, the peak in betweenness centrality might not reflect the existence of a native scale of an observed network.

6.5 Conclusion

This work investigated the feasibility of learning coarse scale network information from a single fine scale starting point. It showed that by using node merger to collapse binarised brain networks down from around 500 regions, one can produce results comparable to those generated using tractography. It should be noted though that the starting point of this process is very important, as uncertainties accumulate at each merging step. This means that the starting scale needs to be fine enough in order to characterise the investigated network. For example, starting at around 100 regions, where the variation in the observed network measures is comparatively high between parcellations, it may prove difficult to capture the behaviour at fewer regions accurately.

With the proposed framework, starting around 500 regions, it was possible to show qualitative and quantitative group/scan differences in measure trajectories between a preterm cohort scanned at birth and at term equivalent age, as well as a control group. The results show that network differences exist over all scales and that the control group, compared to the preterm cohort, exhibits higher transitivity and efficiency, as well as lower betweenness centrality. These results suggest differences in network development, where the exposure to the extra-uterine environment may impair the development of a more efficient network topology.

In general it would be beneficial to find an optimal parcellation scale for network analysis. It has been indicated that observed network properties are possibly the result of merging nodes, such as the heavy-tail degree distribution and the preferential connectivity between nodes with similar degree [4, 75]. In particular the latter could mean that organisational principles, such as the rich-club, might emerge from a random network by merging nodes. Investigating these effects further will be the aim of future work. Importantly, if the scales

at which a brain is analysed are “too coarse”, this could result in an inaccurate assessment of structure, as nodes are effectively merged in these investigations.

By using the collapse with respect to the measure betweenness centrality, it was shown that the indicative peaking of the measure after collapsing may be correlated with a native scale that defines a network. However, it should be emphasised that this feature is also correlated with the density of the network and the network type. Decoupling these aspects will be an important part of future studies.

Additionally the synthetic networks used to analyse this feature rely on a node within a network being split into two subunits. This study chose to retain the connectivity profile of the original node for each subunit, without a connection between them, however, other schemes have been proposed. Alava et al. [4], for example, split the nodes connectivity profile randomly and assign each of its subunits a part of the connectivity profile, with or without connecting the subunits. In their work, however, each node represents an 'atom', which, after splitting, loses its original properties. In the brain, on the other hand, multiple fibres form a bundle which allow regions to be interconnected. Each axon in these bundles originates from a single neuron, which resembles the atom in a brain network. Considering that a brain region consists of many such atoms, the region may be subdivided while broadly keeping the same connectivity profile. Nonetheless, investigating different methods for subdividing nodes in order to oversample a given network may be an interesting area of research in the future, as it possibly allows fine scale information to be inferred from coarse scale information.

Chapter 7

Limitations and Future Work

The approaches presented in this work can be used to distinguish between groups with less bias towards the scale at which network analysis is done. Network normalisation, discussed in chapter 4, can be used to compare networks at a single or local scale and it was shown that using uniform weight randomisation reduces the number of node dependence the most. However, even though determining the best normalisation scheme based on the number of node dependence alone may be a good starting point, other properties of the network may play an important role in finding good surrogate models for normalisation.

In contrast, the multi-scale framework presented in chapter 5 utilises the dependence on the number of nodes for group comparison using the trajectories of network measures across scales. Each network measure calculated at a given scale, however, has an uncertainty due to the multiple random parcellations which can be generated at the same scale. Chapter 5 did not characterise these uncertainties, as they require estimating the measure distribution a given scale and subsequently need many random parcellations and tractography runs. This may form the basis of future work.

The network collapse discussed in chapter 6 infers coarse scale network information from a single fine scale network, by successively merging pairs of nodes. This approach is dependent on the initial fine scale starting network. Subsequently, variations in estimating the starting network may lead to variations at each merging step. Using probabilistic tractography may lead to erroneous connections, in particular at fine scales, which may then lead to variations in the average collapse trajectories.

This chapter focuses on discussing the scale dependence in surrogate networks used for network normalisation and the reliability of network estimation. In addition, some potential methods that can be used to place a network on a scale between lattice networks and random networks are outlined, which will be the aim of future work.

7.1 Scale Dependence in Surrogate Networks

The results of the network normalisation methods presented in chapter 4 support the use of uniformly drawn weights when generating surrogate networks for normalisation. The normalisation step divides an observed network measure by those calculated from random realisations of the observed network. Assuming that the scale dependence can be eliminated using this approach, i.e. resulting in an approximately constant value after normalisation, the observed network measure $m_o(N)$ would satisfy the relationship

$$m_o(N) \approx c\, m_s(N), \tag{7.1}$$

where c is a constant and $m_s(N)$ is the network measure taken from the surrogate network as a function of the number of nodes N. Subsequently a normalisation method to eliminate the dependence on the number of nodes would use surrogate measures with a similar dependence as the original data. This was assessed by investigating surrogate measures calculated from random networks as presented in section 4.2.2.

Each random network used for normalisation is generated using a combination of a method for assigning edges and a method for assigning edge weights. Three types of edge assignments were investigated, based on an Erdös-Rényi model (ER), pairwise switching of the edges (PS), and preserving the edge structure of the observed network (EP). Weights were assigned based on the original edge weights (OW), using uniform random numbers between zero and the maximum weight in the observed network (UNI) and weights generated based on shortest paths in the network (D). Additionally, in case of pairwise switching, the weighted nodal degree can be preserved, when executing a switch (WDP). For each of these randomisation schemes, random network realisations are calculated for the 28 preterm subjects subjects at both time points (baseline and follow-up scan) with 100 networks each (see section 2.3).

In order to assess the trends of the network measures, scatter graphs of them are plotted for each method against the number of regions, where each

point represents a network based on a single random parcellation for one subject. The trends in the scatter plots can then be compared to the observed network measures. In order to make the results comparable, due to the differences in the offset of the individual surrogate measures, the median was subtracted from the data within each subject. The results for one of the network measures (characteristic path-length) are shown in Figure 7.1.

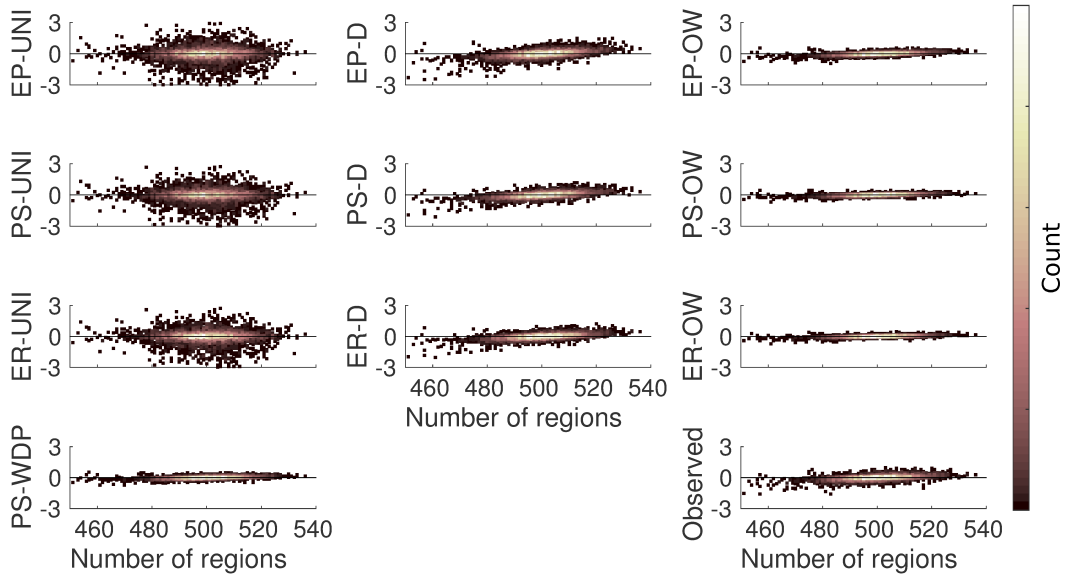

Figure 7.1: Scatter plots for characteristic path-length for 56 subjects with 100 random parcellations each and each randomisation scheme against the number of regions. In addition the observed network measures are plotted for comparison (bottom right). The data were shifted to the same scale by subtracting the median for each subject.

As indicated by the results, it is not clear if the randomisation schemes using uniformly drawn weights follow the same trend as the observed network measures due to the relatively large variation of the network measure in the surrogate networks. Notably this spread of data is biggest for the uniformly drawn weights, compared to all other methods.

To confirm that the normalisation reduces the number of region dependence, as outlined in chapter 4, the normalised values for each scheme are plotted against the number of regions. Assuming that the normalisation successfully eliminated the number of region dependence, one would expect to see a slope of zero with scattering around a mid-line. To allow for easier comparison, due to the differences in offset and scale, the median was subtracted and the results were divided by the inter-quartile range for each subject. The results for characteristic path-length are shown in Figure 7.2.

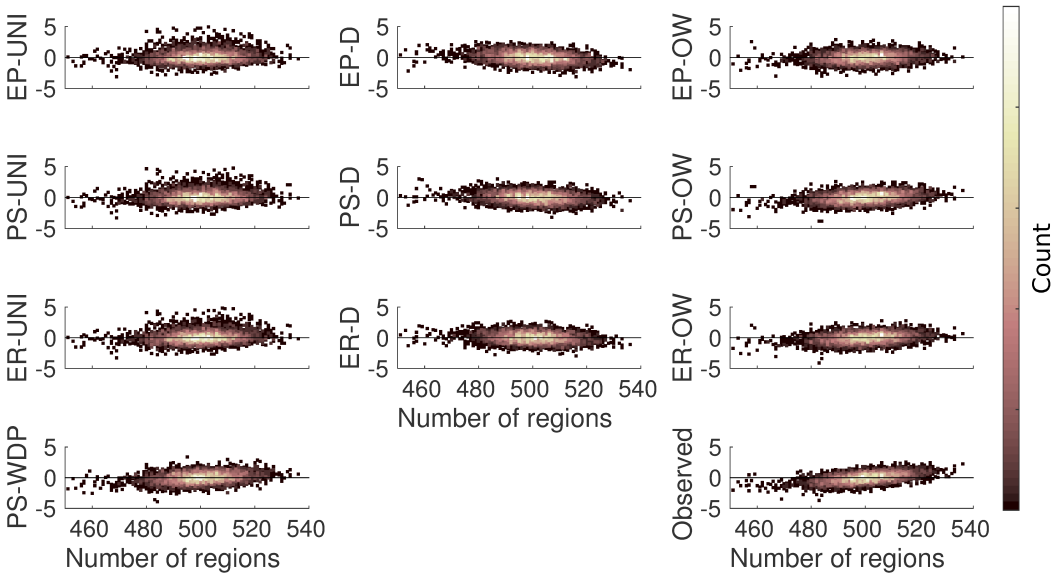

Figure 7.2: Scatter plots of characteristic path-length of 56 subjects with 100 random parcellations each against the number of regions after applying normalisation and of the observed network measures (bottom right). The data was put on the same scale by subtracting the median and dividing by the inter-quartile range for each subject.

The results indicate that a trend in characteristic path-length remains for most of the normalisation schemes. Based on these plots, drawing weights uniformly (UNI) or simply reshuffling the weights (EP-OW) eliminates the dependence the most, i.e. exhibits a slope closer to zero, which is in agreement with the calculated Spearman rank correlation coefficients (Table 4.4).

Intuitively, a random surrogate network is expected to follow a similar trend as the observed network measure, as in equation 7.1. However, the apparently best schemes for normalisation (UNI), do not appear to follow the same trend as the observed network, as shown in Figure 7.1. It is not obvious, why a normalisation by measures that do not appear to match the original trend should decrease the number of region dependence. One explanation could be that the increased variation in the randomised graph measures might conceal the trend after normalisation. If this was the case, however, there should not be an increase in inter-measure correlations, as shown in Figure 4.7. Furthermore, it is possible that the comparison with multiple independent surrogate networks may reduce the overall scattering in case of the uniform weighting schemes.

This work focused on using only one surrogate network per observed network for normalisation. By investigating multiple realisations of surrogate net-

works, however, one can estimate the underlying network measure distribution associated with a given randomisation scheme. A first analysis by generating ten realisations per randomisation scheme did not improve the reduction of the dependence of a given network measure with the number of nodes, compared to using one sample. However, by using more than ten samples, the distribution of network measures may be better estimated. This approach might reveal the overall trend of the uniform weighted normalisation schemes more clearly and show a better agreement with the trend of observed network measures. However, estimating the measure distribution is computationally very expensive as many random surrogate networks are needed and weighted network measure calculation is, compared to unweighted network measure calculations, relatively slow. A more detailed investigation of using many random network realisations for normalisation is needed in future work.

7.2 Reliability of Network Estimation

Group comparisons based on network theory are highly dependent on the framework for estimating networks. Here, dMRI data and a probabilistic tractography algorithm were used [23]. This section will briefly discuss limitations which may arise from the tractography algorithm ProbtrackX.

Due to the iterative step-wise nature of many tractography algorithms, the overall errors in estimating streamline trajectories can accumulate. Tractography algorithms have to deal with many uncertainties when estimating pathways between brain regions, such as the inability to determine precise end points in the cortex and effects due to the use of termination criteria [72]. Additionally it has been pointed out that probabilistic tractography estimates short range connections, i.e. connections between brain regions that are spatially close, with greater confidence than long range connections [72]. Moreover, it was shown recently that, even though probabilistic tractography may provide better long range connectivity information than deterministic tractography (see section 2.2.2), the amount of missed long range connectivity might be in the order of 50% [118].

Due to the relatively coarse resolution of dMRI data with typical voxel sizes of $2 \times 2 \times 2\ mm^3$ [126] and axonal diameters typically of less than 10 μm [101], some fibre patterns are particularly difficult to distinguish. One example of patterns that are difficult to distinguish is given by kissing and crossing fibres, as illustrated in Figure 7.3. Methods such as super-resolution can improve the

resolution of diffusion data to some extent [126], however, resolving the issue of distinguishing between these patterns remains an open challenge.

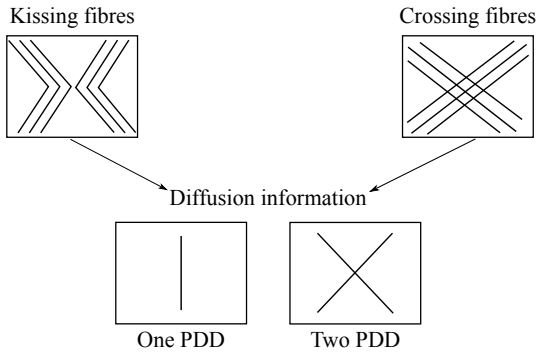

Figure 7.3: Illustration of kissing and crossing fibres in a single voxel. Both patterns produce the same diffusion information, which is dependent on the number of principal diffusion directions (PDD) that are modelled.

Furthermore, by using a probabilistic tractography algorithm, there may be differences between separate runs of the algorithm. It is therefore important to assess the effect of this variation in the networks. In a stability analysis of the networks generated, the agreement between two runs of ProbtrackX for the same diffusion data was investigated. Note that ProbtrackX uses a fixed random seed for its sampling that leads to identical output from repeated runs. Figure 7.4 shows scatter plot comparisons of the edge weights produced by two independent tractography runs, i.e. with different random seed, at three different network scales. The mean integrated anisotropy along all paths is used as weight of each edge (see section 3.7.2). In this weighted analysis, differences between two estimated networks can be seen, as all points would lie on a straight line if the two iterations completely agree.

If a similar analysis is conducted on the binarised networks, i.e. on the networks adjacency matrices, a percentage of agreement on how many connections were found in both executions of the tractography algorithm can be estimated. Table 7.1 shows the result of the agreement in percent at the different scales.

Table 7.1: Percentage of agreement between two independent tractography executions using the networks adjacency matrix.

Scale	100	300	500
Agreement	94%	95%	96%

Note that the values are given as percentages and that the total number of edges increases with the number of regions. However, independent tractogra-

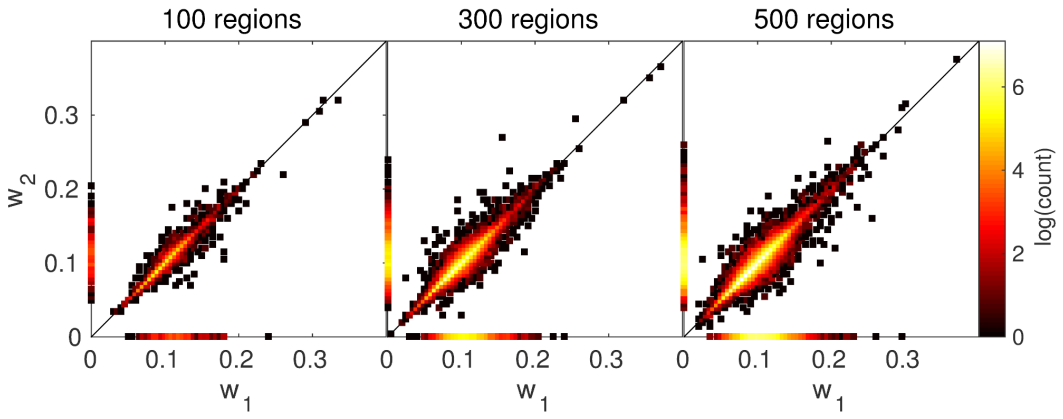

Figure 7.4: Comparison of two network estimates obtained by separate tractography runs at three different scales using ProbtrackX. Each connection with its weight w_1 in the first run is plotted against its counterpart from the second run with weight w_2. The counts for all weight pairings is encoded in the colour scheme.

phies agree on average on $95 \pm 1\%$ of the connectivity profile over all scales investigated.

In general, it is possible to estimate the overall effect of these variations in network estimation on measures. A detailed analysis of the variation, by estimating the structural connectivity profile multiple times from independent tractography executions is an appropriate topic for future work.

Further work could also seek to determine the accuracy of the tractography algorithm used and optimise network theoretical approaches in the human brain by finding the most appropriate algorithm. Bastiani et al. [16], for example, propose a method for estimating if the tractography algorithm produces "acceptable" results, by comparing estimated connections between brain regions with connections biologically known to be present. However, this method relies on the exact delineation of regions of interest, which, as described in section 2.1, is challenging in a neonatal cohort. Further development in tractography algorithms and validation using tracer studies may help to alleviate this challenge by providing more accurate connectivity profiles of the developing human brain.

7.3 Characterising Network Type with Multi-Scale Analyses

One striking feature in the observed network measures that motivated the use of multi-scale frameworks (chapters 5 and 6) was the difference in the shapes of the network measure trajectories. As previously described, results presented by Van Wijk et al. [164] show graphs of network measures taken on random, small-world and lattice network topologies over multiple scales. These graphs suggest that different network topologies exhibit different shapes of the network measure trajectories. Figure 7.5 shows network trajectories for betweenness centrality and characteristic path-length taken from random (ER; $p = 100\%$), small-world (SW; $p = 10\%$) and lattice-like (L; $p = 1\%$) network topologies over scales of $s = 50, 60, \ldots, 400$ regions using the framework presented in section 6.2.3 and with weights drawn randomly from a Gaussian distribution.

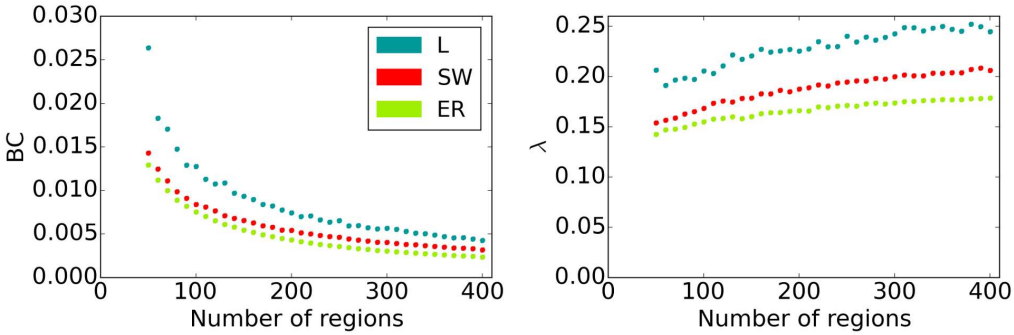

Figure 7.5: Measure trajectories of betweenness centrality (BC) and characteristic path-length (λ) for lattice (L), small-world (SW) and random (ER) network topologies for weighted undirected graphs over multiple scales.

The results show that trajectories of different network topologies over multiple scales have different shapes. The effect appears to be more pronounced for characteristic path-length than for betweenness centrality. Moreover, determining the network type of an observed network is an important goal when comparing healthy populations and patients, as deviations of it may be indicative of disease. For example, work presented by Rubinov et al. [122] suggest a subtle randomisation in schizophrenia. During the early development of the human brain substantial changes occur with regard to the structural connectivity profile (see section 2.1) and it is possible that events such as premature birth may influence the structural network topology (see for example [8]).

This section outlines two possible approaches to determine the type of a network by placing it on a scale between lattice and random networks. The first approach is directly related to the network trajectories investigated in chapter 6 and determines the best fit to binarised surrogate networks evaluated over multiple scales. The second approach introduces the concept of measure landscapes, which will be refer to as *m-scapes*. M-scapes are a mapping of network scale and randomisation percentage to investigated network measures and an approach that may be used to determine the extent of network randomisation is described.

7.3.1 Shape of Measure Trajectories

The first approach starts by creating trajectories from surrogate networks that are on a scale between lattice and random network topologies. This can be achieved by using the approach outlined in section 6.2.3 and applying the network collapse framework discussed in chapter 6 to generate measure values over multiple scales. The surrogate networks are size and density matched to the observed network, allowing for individual differences in network density to be factored out.

In order to match the density of surrogate networks in the context of section 6.2.3, the density of the observed network is calculated and subsequently the neighbourhood order of connected nodes in the surrogate lattice network is increased until its density either matches or exceeds that of the observed network. If the observed density was exceeded, edges in the network are randomly deleted, until the required density is reached. In general, the whole process could be repeated multiple times, each time generating a density matched network with slightly different topology. In this section, however, only one sample of the density matched networks is used.

After the density matched lattice network has been generated, randomisation of edges can be iteratively executed. This creates a spectrum of density matched surrogate networks with equal size to the observed network with varying degrees of randomisation. Each of these networks can then used as input to the network collapse framework. Network measure calculations over all steps of the collapse provide trajectories corresponding to the surrogate networks and in turn for each level of randomisation. The framework is illustrated in Figure 7.6.

The change of network measure trajectories while altering the randomisation percentage between $p = [1, 4, \ldots, 100]$ is shown for in Figure 7.7. Entire

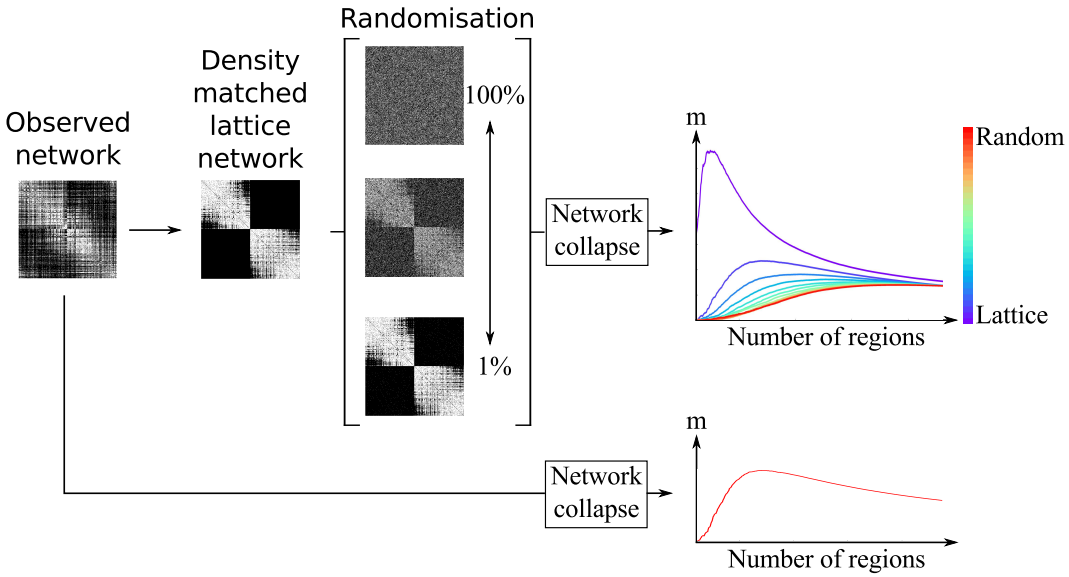

Figure 7.6: Framework for comparing network measure trajectories. An observed measure trajectory is generated using the network collapse model. Separately, a density matched lattice network is estimated and multiple randomised realisation of the lattice network are generated. These are used as input to the network collapse. Each resulting trajectory may subsequently be compared to the trajectory of the observed network.

trajectories may subsequently be compared by calculating their L_1 distance. The randomisation value of the surrogate network that best describes the observed trajectory, i.e. with the smallest distance, is then used to provide an estimate of the randomisation in the observed network. In order to focus on the shapes of the trajectories, each network measure's trajectory may be zero-centred by subtracting the mean of the trajectory value.

In a first analysis, the framework was applied to a group of term born infants (see section 2.3) by generating a total of 34 density matched surrogate networks per subject with randomisation levels of $p = [1, 4, \ldots, 100]\%$, which were used to estimate the percentage of randomisation of each subject. Each network was used 10 times as a starting point for the collapse framework. The average trajectory over the ten repetitions was subsequently compared to the average collapse trajectory of the observed network (again from ten repetitions). In order to speed up the process of the network collapse, the number of consecutive mergers before network measures were calculated was set to 25, until the number of nodes was below 200, where it was reduced to 10. The node merger was used until the resulting network was below a scale of 25. Figure 7.8 shows the randomisation percentage estimated for each subject, where each scatter point represents the randomisation estimated for

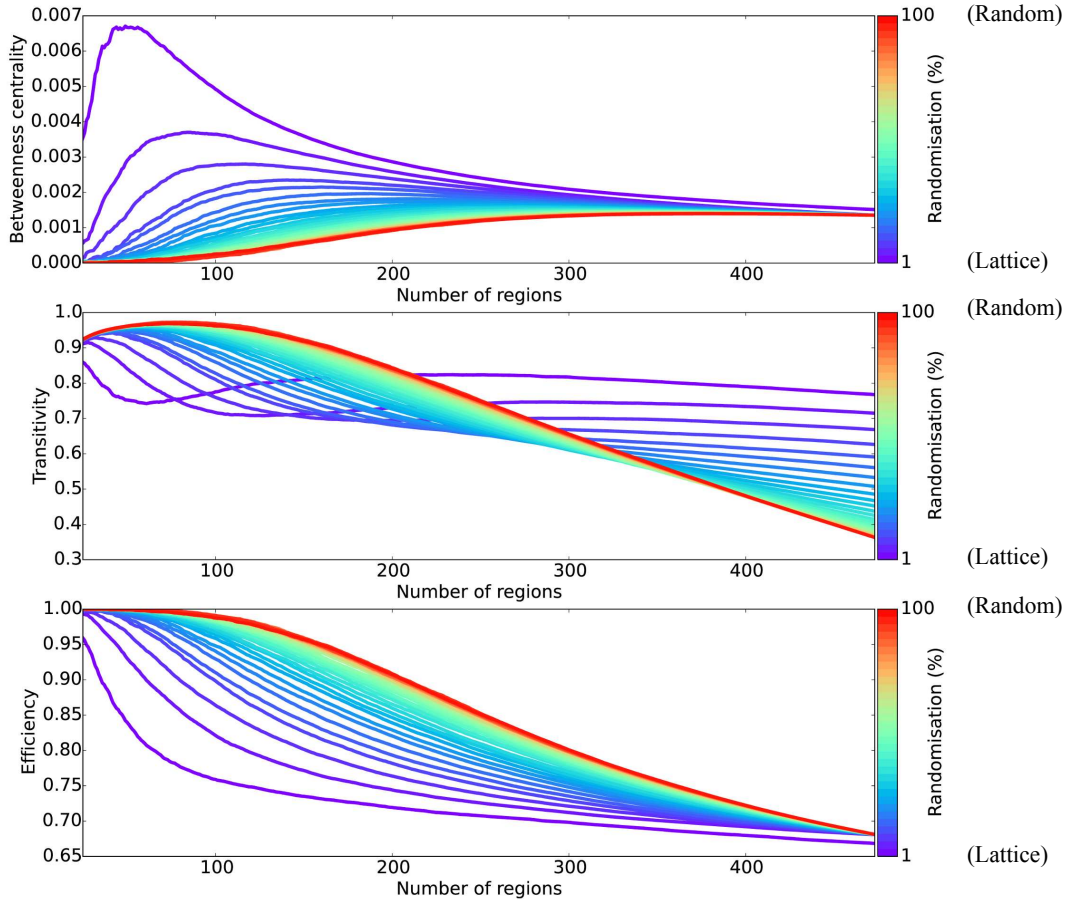

Figure 7.7: Change of betweenness centrality, transitivity and efficiency trajectories as the network type is randomised between $p = [1, 4, \ldots, 100]\%$. Each trajectory can serve as a reference, against which a trajectory from observed brain data can be compared.

each network measure.

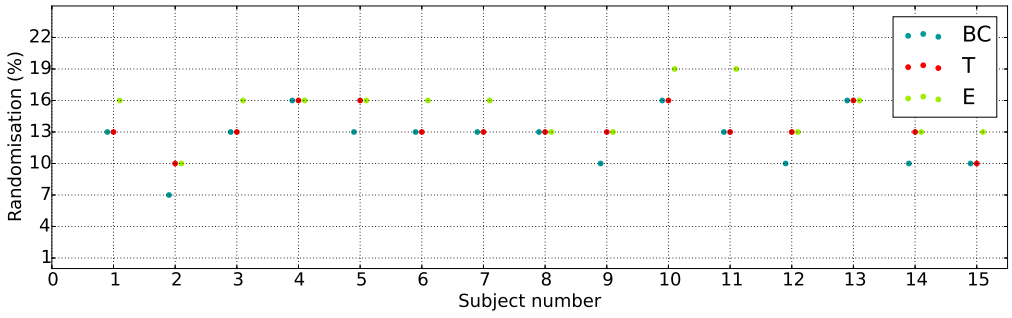

Figure 7.8: Estimated percentage of network randomisation in 15 control group infants, using betweenness centrality (BC), transitivity (T) and efficiency (E).

The results show that the estimation of the randomisation percentage is

relatively stable across measures. Table 7.2 summarises the average percentage estimated for each network measure, where the average was taken over all subjects.

Table 7.2: Average percentage of randomisation and standard deviation estimated in the term control group.

Measure	BC	T	E
Estimated Randomisation (%)	12.7 ± 2.4	13.5 ± 1.7	15.5 ± 2.5

The estimated randomisation percentages based on the three different network measures suggest a randomisation of approximately 14% for the control group. Note that the randomisation percentages p were coarsely sampled. This offers an opportunity for improvement when estimating the scale of randomisation, by using smaller step sizes in p. Additionally, the resolution of the collapse framework can be improved by using smaller numbers of mergers executed before a network measure is calculated. The application of this framework to a preterm cohort will be the aim of future work. Also, the investigation of group differences in a larger sample of subjects with known clinical or demographic information may be useful to demonstrate the utility of the randomisation level estimation as presented here. It should be noted that this framework is not limited to neonatal cohorts and that it may be used to determine topological changes in brain networks in development and disease more generally.

7.3.2 M-Scapes

In a second approach, an analysis based on measure landscapes, or m-scapes, is proposed, which map out the behaviour of a given network measure as the size and randomisation percentage of the network are altered.

M-Scape Creation

In order to create an m-scape for a measure m, one starts out by generating a lattice network at a scale s. Subsequently multiple randomised networks are generated by randomising p% of the edges. At each step of randomisation, the value of the network measure is recorded. The entire set of network measures calculated with different randomisations at scale s subsequently represents a row in the m-scape. Afterwards the scale s is changed and the process repeated. The framework is illustrated in Figure 7.9.

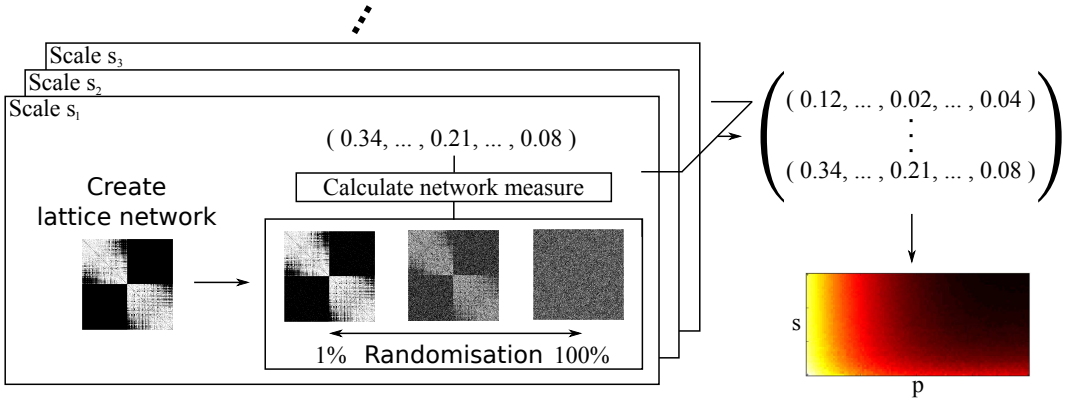

Figure 7.9: Framework used for generating m-scapes. After a lattice network at scale s is generated, multiple randomised networks are generated by randomising $p\%$ of the edges. For each network the global network measure is recorded. Subsequently the scale is altered and the process repeated. The set of all measures represents a measure landscape (m-scape).

With this procedure it is possible to create m-scapes for all network measures of interest. Figure 7.10 shows the m-scapes and measure distributions for betweenness centrality, transitivity and efficiency, evaluated at scales of $s = 50, 60, ..., 500$ and randomisation levels of $p = 1, 2, .., 100\%$. The networks used to calculate the network measures are created using the approach presented in section 6.2.3 with $n = 2$.

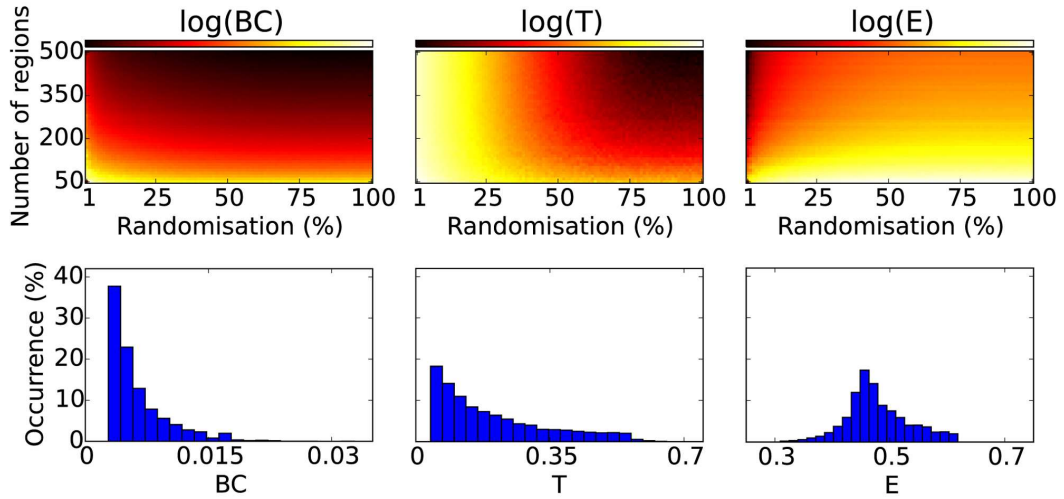

Figure 7.10: M-scapes for betweenness centrality, transitivity and efficiency (top). Each point is calculated at a given scale s, i.e. number of regions, with a given percentage of randomisation. The overall distribution of each network measure is represented by the corresponding histogram (bottom).

Estimating Randomisation Percentage

The goal is to estimate the randomisation percentage found in an observed network by finding its' position in the m-scape. When applying network analysis to real data, the scale of the observed network is usually known. Consequently it becomes unnecessary to compare the entire m-scape with an observed network measure and it is sufficient to extract the row in the m-scape that corresponds to the scale of the observed network for comparison. The line profile of a row in an m-scape can therefore be used to estimate the randomisation percentage, at which the measure value is found. This principle is illustrated in Figure 7.11.

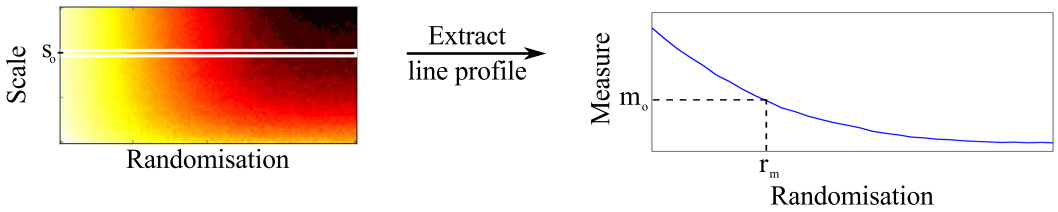

Figure 7.11: Estimating the randomisation percentage, based on an observed network measure value. From a given m-scape the line profile at the scale of the observed network is extracted and used for finding the randomisation percentage r_m corresponding to the observed measure value m_o.

In order to test this framework five networks are created as described earlier (see section 6.2.3, $n = 2$). The scales of each network were chosen randomly and the set of scales is given by $s = \{60, 182, 271, 344, 457\}$. In addition, five randomly chosen levels of edge randomisation are investigated for each of these networks given by $p = \{28, 31, 47, 63, 92\}\%$. For the resulting 25 networks their global betweenness centrality, transitivity and global efficiency were calculated.

For each network measure the line profile of the m-scapes as shown in Figure 7.11 was extracted and the randomisation percentage for each of the 25 networks was estimated. This approach results in a set of three estimates per network, one per network measure, as shown in Figure 7.12.

The results for the three different network measures show varying efficacy of predicting the percentage used to generate the test networks. In general the estimation at low percentages of randomisation seems to be more accurate than for high percentages for all measures. Betweenness centrality and efficiency also seem to underestimate the randomisation scale at higher percentages, whereas transitivity seems to result in a good estimate with small variations around the percentage used for generating the networks. Notably the randomisation estimates for each of the 25 networks did not agree on a single value across

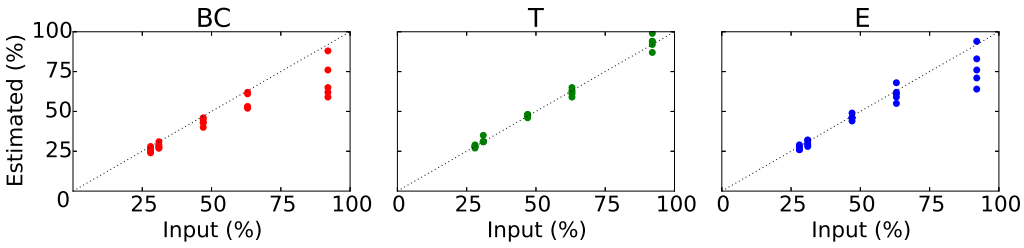

Figure 7.12: Results of estimating randomisation percentage of test networks using m-scapes. Points indicate the estimated percentage in comparison to the percentage used to generate each of the 25 networks (input) for each of the three network measures.

measures. Using the average for each set, however, showed a good agreement with an error of approximately 6%, compared to the original values.

Uncertainties in M-Scapes

M-scapes as shown in Figure 7.10 are not unique. Multiple executions of the randomisation process will result in slight variations in the calculated network measures for each combination of scale and randomisation level. This variance can be used to create a confidence interval at each point in the m-scape. Subsequently, when placing an observed network measure value in the m-scape, this confidence interval can be taken into account to achieve a better estimate of the randomisation percentage. Placing a network measure within an m-scape that includes a confidence interval leads to a range of randomisation percentage estimates, so that the observed value $r_m^o \in [r_m^{lo}, r_m^{hi}]$. Figure 7.13 shows the principle of estimating the randomisation percentage of an observed network, while incorporating the confidence interval of the m-scape.

For this work, however, only one m-scape was generated and therefore the confidence interval was defined empirically for use with each point in the m-scape. This can be achieved, for example, by rounding the network measure values in the m-scape and the observed network to their second significant digit.

Using the 25 networks described earlier, their randomisation percentage was estimated with this approach. For each network measure the corresponding randomisation intervals r_{BC}, r_T and r_E were determined. Subsequently, the observed network was assigned a range of randomisation percentage

$$r_{comb}^o = r_{BC} \cap r_T \cap r_E \tag{7.2}$$

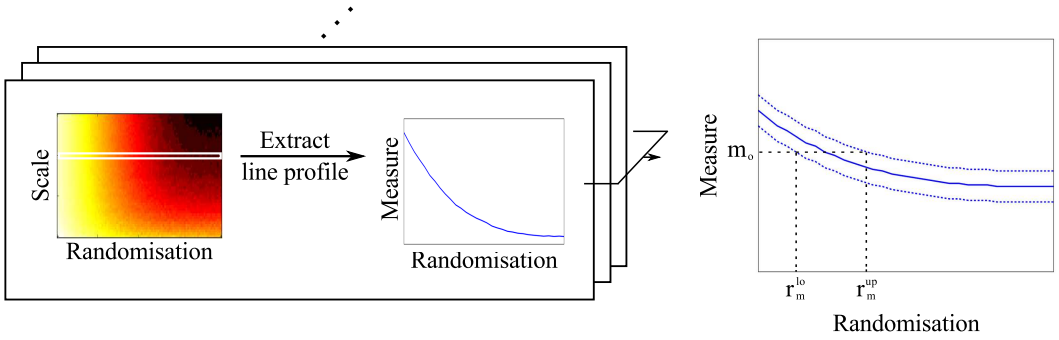

Figure 7.13: Principle of estimating a networks randomisation percentage with uncertainties in m-scapes. Uncertainties in the network measures derived from repetitions of m-scape creation may be used to identify a range of randomisation percentages within which an observed network can be placed.

given by the intersection of all ranges. A point estimate for the randomisation level of a network may then be given by the centre of the combined range r^o_{comb}.

For four out of the 25 networks the intersection of all three measures was empty and therefore no randomisation percentage was estimated. This could result from the predefined confidence interval ϵ being too small or a coarse m-scape grid being used. The remaining 21 networks' randomisation percentages were predicted with an average error of 3% compared to their original values. These results, shown in Figure 7.14, suggest that the approach can be used to estimate the randomisation percentage of an observed network.

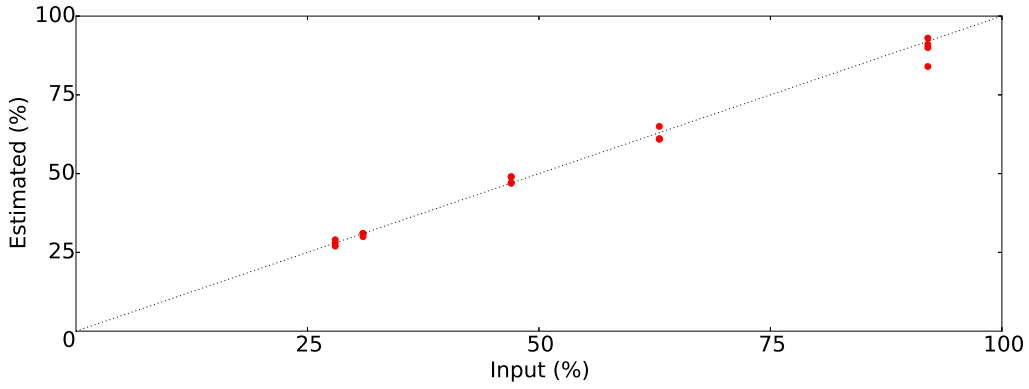

Figure 7.14: Results of estimating randomisation percentage of test networks using m-scapes including a confidence interval. Points indicate the consensus estimated percentage from three network measures in comparison to the percentage used to generate each of the 21 networks (input).

Uncertainties in Network Scale

The scale of an observed network is usually known. However, it is possible that an observed network has a latent scale at which network theory is most descriptive of the network's properties. In this case, the number of nodes of the observed network may not correspond to the latent scale and subsequently using the row in the m-scape corresponding to the scale of the observed network may not be the best approach. M-scapes, however, map scale and randomisation percentage to network measure values. Subsequently it is possible to use an m-scape to determine a combined estimate for the randomisation percentage and scale.

Given an observed network measure value, one can estimate regions or bounds of agreement in the m-scapes incorporating the confidence intervals as discussed above. Figure 7.15, for example, shows of the bounds for the network measure corresponding to $(s = 280, p = 51\%)$ in the m-scapes for each measure.

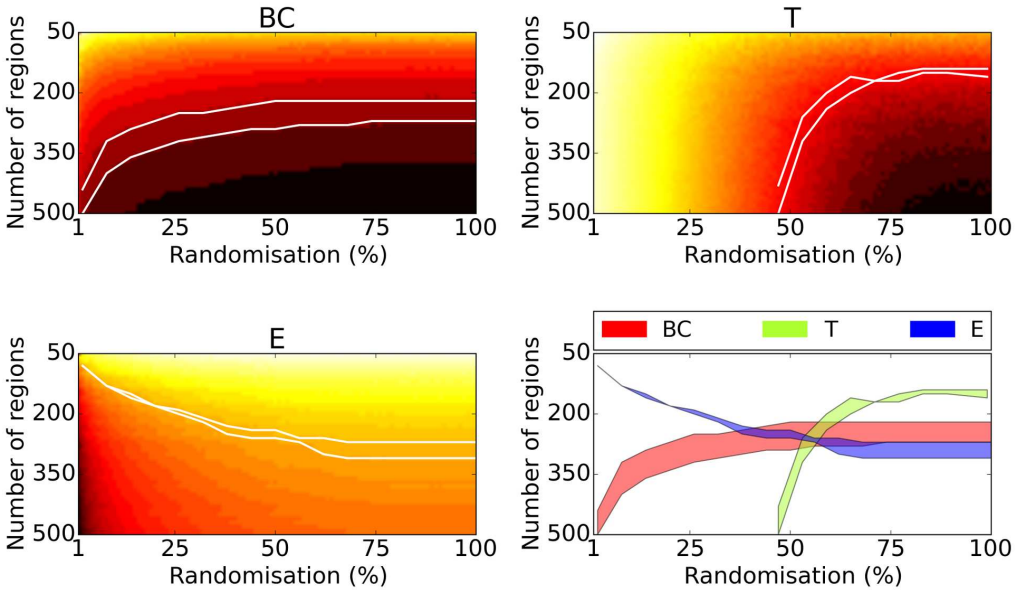

Figure 7.15: Regions of approximately equal network measures value corresponding to the value of the network with 280 regions and 51% randomisation for each network measure (enclosed by white lines). Subsequently the intersect of the regions can be estimated (bottom right).

The intersection of all regions defined by the bounds can then be used to estimate the observed network scale and randomisation level based on a consensus vote (see Figure 7.15, bottom right). That means that one determines

the combined area A^o_{comb} given by

$$A^o_{comb} = A_{BC} \cap A_T \cap A_E, \tag{7.3}$$

where A_{BC}, A_T and A_E are defined as indicated in Figure 7.15 (bottom right) in red, green and blue, respectively. Again, a point estimate for the randomisation level and scale of a network may then be given by the centroid of the combined region A^o_{comb}.

In the case presented in Figure 7.15, the point estimate is given by (284,53%). It should be emphasised that the resolution in scale of the m-scapes as presented above is relatively low, with one sample taken every ten regions along the scale axis. Nonetheless, the overall agreement with the selected point is good. This process was applied to the 25 test networks and for 24 out of the 25 networks randomisation percentage and scale could be estimated. For one network there was no intersection between all three regions. The results of the comparison between estimated randomisation percentage and scale, compared to the values used to generate the test networks are shown in Figure 7.16.

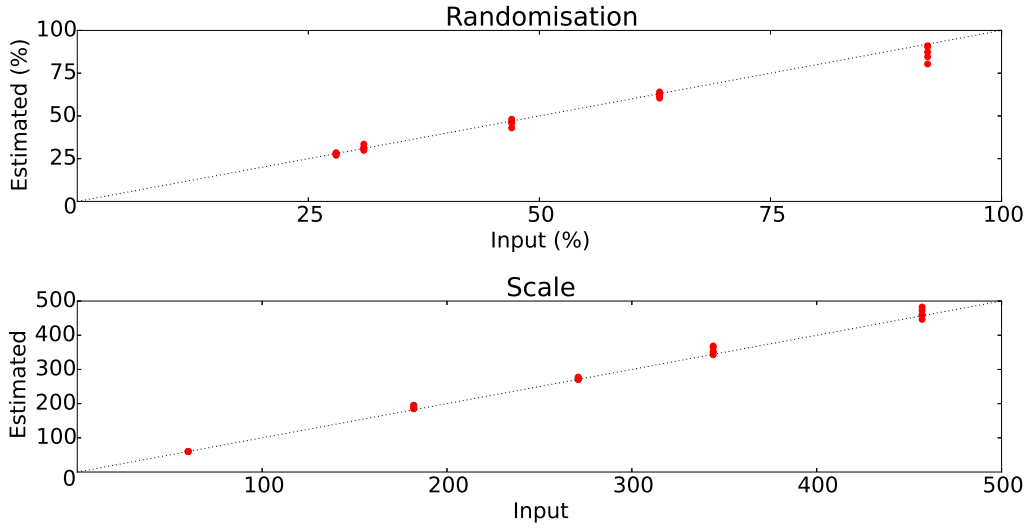

Figure 7.16: Results of estimating randomisation percentage and scale of test networks using m-scapes. Scatter points indicate the consensus of the estimated randomisation percentage (top) and scale (bottom) from three network measures in comparison to the randomisation percentage and scale used to generate each of the 21 networks (input).

The average error of the estimated scale and randomisation percentage is given by 2% and 3%, respectively. It should be noted that the set of test networks were not enforced to have a scale equal to those used to generate

the m-scapes. Nonetheless, this approach was able to determine both scale and randomisation percentage using a coarse grid. The networks tested in this approach are already generated at their native scale. Investigating the possibility of inferring the native scale if a network was over-/under-sampled, as discussed in chapter 6, will be the aim of future work.

Application to Brain Data

A network derived from brain data may be characterised according to its position in the m-scape of each measure by finding its randomisation percentage as presented in this section. A possible framework of applying this approach to brain data could subsequently involve the following steps. First, generate the structural brain network of a subject at a medium scale, for example, $s = 250$ regions. This network's density can then be used to generate density matched surrogate networks, which serve as the baseline to estimate the subject's m-scapes including confidence intervals. A consensus vote between the rows of the m-scape can be determined and subsequently the network's randomisation percentage may be estimated, which may then serve as a measure of network type. Such an application to human data, will be the aim of future work.

Chapter 8

Conclusion

Challenges arise when trying to use network theory, if the definition of the nodes is uncertain, as it is the case in the developing brain. Due to the significant biological changes in the structural connectivity profile and grey matter structure in the early stages of development, it becomes difficult to register adult based definitions of brain regions to the developing brain. Nonetheless, investigating brain development, in particular after premature birth is an important area of research, as it has been shown that approximately 50% of all infants born prematurely suffer from negative cognitive outcome [175], such as motor [94, 95], auditory [94, 125], visual [37, 94] and cognitive impairments [94]. Finding biomarkers in order to identify infants at risk of such impairments is an important goal and network theory is a promising tool for achieving this [62, 87, 165, 168].

With the challenge of registering atlases to the developing brain and the lack of a consensus on which parcellation scheme to use, stochastic approaches provide a potential alternative, as they rely on fewer assumptions compared to atlas based definitions [6, 151, 153]. One random parcellation scheme, which allows the relatively easy definition of regions in the brain at arbitrary scales is based on Poisson disk sampling. The application of random parcellation schemes such as Poisson disk sampling, however, may lead to the comparison of networks at different scales which is a non-trivial task, due to the network measures' dependence on the number of nodes in a graph [127, 164, 179]. This dependence has lead to a recent increase in studies using network analysis at multiple scales, in order to ensure that the observed trends are valid across scales.

The aim of this thesis was to develop methods to compare networks based on unknown number, location and size of brain regions, which define the nodes in the networks. Chapter 4 investigated the use of network normalisation, where an observed network measure is normalised by those calculated on a randomised surrogate network. This approach showed that, using an appropriate method for creating these surrogate networks, the region dependence can be reduced at a local scale, i.e. over a small variation in number of regions.

Observing the trends of the investigated network measures over multiple scales and for different subjects, however, revealed that the measures taken for individual subjects show a different dependence on the number of nodes. Chapter 5 showed that this dependence can be characterised and used for group comparison, by investigating the combined information of a relatively small number of networks created at a variety of scales. However, this approach may be computationally expensive, as it necessitates the use of tractographies at multiple scales. In order to alleviate this computational cost, chapter 6 proposed the use of a node merger, starting from a network with a high number of regions (high scale), in order to infer low scale network information.

The work presented was used to compare structural brain networks estimated in a serial dMRI dataset of prematurely born infants, where the infants were scanned at birth and term equivalent age, as well as a control cohort of term born babies. It showed that network normalisation, multi-scale and collapse frameworks can be used for comparing groups with statistical significance. This suggests that it may be possible to use these approaches to investigate possible biomarkers for neurodevelopmental and neurodegenerative diseases. Overall, the methods developed may help to alleviate the challenges due to unknown location, size and number of nodes in a brain network and may provide additional information on developmental difference in terms of network topology due to premature exposure to the extra-uterine environment.

Bibliography

[1] Achard et al. A resilient, low-frequency, small-world human brain functional network with highly connected association cortical hubs. *J. Neurosci.*, 26(1):63–72, 2006.

[2] C B Ahn, J H Kim, and Z H Cho. High-speed spiral-scan echo planar NMR imaging-I. *IEEE T. Med. Imaging*, 5(1):2–7, 1986.

[3] Ahn et al. Flavor network and the principles of food pairing. *Sci. Rep.*, 1:196, 2011.

[4] M J Alava and S N Dorogovtsev. Complex networks created by aggregation. *Phys. Rev. E*, 71(3):036107, 2005.

[5] Arpino et al. Preterm birth and neurodevelopmental outcome: a review. *Child's Nervous System*, 26(9):1139–1149, 2010.

[6] Ball et al. The effect of preterm birth on thalamic and cortical development. *Cereb. Cortex*, 22(5):1016–1024, 2012.

[7] Ball et al. The influence of preterm birth on the developing thalamocortical connectome. *Cortex*, 49(6):1711 – 1721, 2013.

[8] Ball et al. Rich-club organization of the newborn human brain. *P. Natl. Acad. Sci. USA*, 111(20):7456–7461, 2014.

[9] A L Barabási and R Albert. Emergence of scaling in random networks. *Science*, 286(5439):509–512, 1999.

[10] A L Barabási and E Bonabeau. Scale-free. *Sci. Am.*, 2003.

[11] A J Barkovich and C Raybaud. *Pediatric Neuroimaging*. Lippincott Williams & Wilkins, 2012.

[12] P J Basser, J Mattiello, and D LeBihan. Estimation of the effective self-diffusion tensor from the nmr spin echo. *J. Magn. Reson. Ser. B*, 103(3):247–254, 1994.

[13] Basser et al. In vivo fiber tractography using DT-MRI data. *Magn. Reson. Med.*, 44(4):625–632, 2000.

[14] D S Bassett and E T Bullmore. Human brain networks in health and disease. *Curr. Opin. Neurol.*, 22(4):340–347, 2009.

[15] Bassett et al. Adaptive reconfiguration of fractal small-world human brain functional networks. *P. Natl. Acad. Sci. USA*, 103(51):19518–19523, 2006.

[16] Bastiani et al. Human cortical connectome reconstruction from diffusion weighted MRI: the effect of tractography algorithm. *NeuroImage*, 62(3):1732–1749, 2012.

[17] Batalle et al. Altered small-world topology of structural brain networks in infants with intrauterine growth restriction and its association with later neurodevelopmental outcome. *NeuroImage*, 60(2):1352 – 1366, 2012.

[18] C Beaulieu. The basis of anisotropic water diffusion in the nervous system – a technical review. *NMR Biomed.*, 15(7-8):435–455, 2002.

[19] Beck et al. The worldwide incidence of preterm birth: a systematic review of maternal mortality and morbidity. *B. World Health Organ.*, 88(1):31–38, 2010.

[20] T E J Behrens and S Jbabdi. MR diffusion tractography. *Diffusion MRI*, pages 333–351, 2009.

[21] T E J Behrens and O Sporns. Human connectomics. *Curr. Opin. neurobiology*, 22(1):144–53, 2012.

[22] Behrens et al. Characterization and propagation of uncertainty in diffusion-weighted MR imaging. *Magn. Reson. Med.*, 50(5):1077–1088, 2003.

[23] Behrens et al. Probabilistic diffusion tractography with multiple fibre orientations: What can we gain? *NeuroImage*, 34(1):144–155, 2007.

[24] F M Benes. Myelination of cortical-hippocampal relays during late adolescence. *Schizophrenia Bull.*, 15(4):585, 1989.

[25] Betzel et al. Multi-scale community organization of the human structural connectome and its relationship with resting-state functional connectivity. *Netw. Sci.*, 1(3):353–373, 2013.

[26] Bloch et al. Nuclear induction. *Phys. Rev.*, 69(3–4):127, 1946.

[27] R Bridson. Fast Poisson disk sampling in arbitrary dimensions. In *ACM SIGGRAPH*, volume 2007, page 5, 2007.

[28] K Brodmann. Vergleichende Lokalisationslehre der Groshirnrinde. *Leipzig: Barth*, 1909.

[29] E Bullmore and O Sporns. Complex brain networks: graph theoretical analysis of structural and functional systems. *Nat. Rev. Neurosci.*, 10(3):186–198, 2009.

[30] E Bullmore and O Sporns. The economy of brain network organization. *Nat. Rev. Neurosci.*, 13(5):336–349, 2012.

[31] Cammoun et al. Mapping the human connectome at multiple scales with diffusion spectrum MRI. *J. Neurosci. Meth.*, 203(2):386 – 397, 2012.

[32] Casey et al. Imaging the developing brain: what have we learned about cognitive development? *Trends Cogn. Sci.*, 9(3):104–110, 2005.

[33] Catani et al. The rises and falls of disconnection syndromes. *Brain*, 128(10):2224–2239, 2005.

[34] J G Chi, E C Dooling, and F H Gilles. Gyral development of the human brain. *Ann. Neurol.*, 1(1):86–93, 1977.

[35] Colizza et al. Detecting rich-club ordering in complex networks. *Nat. Phys.*, 2(2):110–115, 2006.

[36] Collin et al. Structural and functional aspects relating to cost and benefit of rich club organization in the human cerebral cortex. *Cereb. Cortex*, 24:2258–2267, 2013.

[37] Dammann et al. Immaturity, perinatal inflammation, and retinopathy of prematurity: a multi-hit hypothesis. *Early Hum. Dev.*, 85(5):325–329, 2009.

[38] Danon et al. Comparing community structure identification. *J. Stat. Mech. Theory E.*, 2005(09):P09008, 2005.

[39] M A De Reus and M P van den Heuvel. Rich club organization and intermodule communication in the cat connectome. *J. Neurosci.*, 33(32):12929–12939, 2013.

[40] Delobel-Ayoub et al. Behavioral problems and cognitive performance at 5 years of age after very preterm birth: the EPIPAGE Study. *Pediatrics*, 123(6):1485–92, 2009.

[41] Dennis et al. Development of brain structural connectivity between ages 12 and 30: a 4-Tesla diffusion imaging study in 439 adolescents and adults. *NeuroImage*, 64:671–84, January 2013.

[42] E W Dijkstra. A Note on Two Problems in Connexion with Graphs. *Numer. Math.*, 1:269–271, 1959.

[43] P S Dodds, R Muhamad, and D J Watts. An experimental study of search in global social networks. *Science*, 301(5634):827–829, 2003.

[44] Dyrby et al. Validation of in vitro probabilistic tractography. *NeuroImage*, 37(4):1267–77, 2007.

[45] D Easley and J Kleinberg. *Networks, Crowds, and Markets: Reasoning About a Highly Connected World*. Cambridge University Press, New York, NY, USA, 2010.

[46] Echtermeyer et al. Integrating temporal and spatial scales: human structural network motifs across age and region of interest size. *Front. Neuroinform.*, 5, 2011.

[47] P Erdös and A Rényi. On random graphs. *Publ. Math.-Debrecen*, 6:290–297, 1959.

[48] Ewing-Cobbs et al. Corpus callosum diffusion anisotropy correlates with neuropsychological outcomes in twins disconcordant for traumatic brain injury. *Am. J. Neuroradiol.*, 27(4):879–881, 2006.

[49] Fagerholm et al. Disconnection of network hubs and cognitive impairment after traumatic brain injury. *Brain*, pages 1696–1709, 2015.

[50] G Fagiolo. Clustering in complex directed networks. *Phys. Rev. E*, 76(2):026107, 2007.

[51] Fair et al. Functional brain networks develop from a local to "distributed" organization. *PLoS Comput. Biol.*, 5(5):e1000381, 2009.

[52] Fan et al. Brain anatomical networks in early human brain development. *NeuroImage*, 54(3):1862–71, 2011.

[53] A Fornito, A Zalesky, and E T Bullmore. Network scaling effects in graph analytic studies of human resting-state fmri data. *Front. Syst. Neurosci.*, 4(22), 2010.

[54] L C Freeman. A set of measures of centrality based on betweenness. *Sociometry*, 40(1):35–41, 1977.

[55] Gogtay et al. Dynamic mapping of human cortical development during childhood through early adulthood. *P. Natl. Acad. Sci. USA*, 101(21):8174–8179, 2004.

[56] Goh et al. The human disease network. *P. Natl. Acad. Sci. USA*, 104(21):8685–8690, 2007.

[57] Goldenberg et al. Epidemiology and causes of preterm birth. *Lancet*, 371(9606):75–84, 2008.

[58] P Hagmann, P E Grant, and D A Fair. MR connectomics: a conceptual framework for studying the developing brain. *Front. Syst. Neurosci.*, 6, 2012.

[59] Hagmann et al. Mapping human whole-brain structural networks with diffusion MRI. *PLoS ONE*, 2(7):9, 2007.

[60] Hagmann et al. Mapping the structural core of human cerebral cortex. *PLoS Biol.*, 6(7):1479–1493, 2008.

[61] Hagmann et al. White matter maturation reshapes structural connectivity in the late developing human brain. *P. Natl. Acad. Sci. USA*, 107(44):19067–19072, 2010.

[62] Hahn et al. Selectively and progressively disrupted structural connectivity of functional brain networks in alzheimer's disease - revealed by a novel framework to analyze edge distributions of networks detecting

disruptions with strong statistical evidence. *NeuroImage*, 81(0):96 – 109, 2013.

[63] L Harriger, M P Van den Heuvel, and O Sporns. Rich club organization of macaque cerebral cortex and its role in network communication. *PLoS ONE*, 7(9):e46497, 2012.

[64] Hidalgo et al. The product space conditions the development of nations. *Science (New York, N.Y.)*, 317(5837):482–7, July 2007.

[65] Hilgetag et al. Anatomical connectivity defines the organization of clusters of cortical areas in the macaque monkey and the cat. *Philos. T. Roy. Soc. B*, 355(1393):91–110, 2000.

[66] Huisman et al. Diffusion tensor imaging as potential biomarker of white matter injury in diffuse axonal injury. *Am. J. Neuroradiol.*, 25(3):370–376, 2004.

[67] M D Humphries and K Gurney. Network 'small-world-ness': a quantitative method for determining canonical network equivalence. *PLoS ONE*, 3(4):e0002051, 2008.

[68] P R Huttenlocher and A S Dabholkar. Regional differences in synaptogenesis in human cerebral cortex. *J. Comp. Neurol.*, 387(2):167–178, 1997.

[69] Huttenlocher et al. Synaptic density in human frontal cortex-developmental changes and effects of aging. *Brain Res*, 163(2):195–205, 1979.

[70] T E Inder and P S Huppi. In vivo studies of brain development by magnetic resonance techniques. *Ment. Retard. Dev. D. R.*, 6(1):59–67, 2000.

[71] A Jamakovic and S Uhlig. On the relationships between topological measures in real-world networks. *Netw. Heterog. Media*, 3(2):345–359, 2008.

[72] S Jbabdi and H Johansen-Berg. Tractography: where do we go from here? *Brain Connect.*, 1(3):169–183, 2011.

[73] B Jennett and R MacMillan. Epidemiology of head injury. *BMJ*, 282(6258):101–104, 1981.

[74] Jones et al. Non-invasive assessment of axonal fiber connectivity in the human brain via diffusion tensor MRI. *Magn. Reson. Med.*, 42(1):37–41, 1999.

[75] Kim et al. Self organized scale-free networks from merging and regeneration. *Eur. Phys. J. B*, 43(3):369–372, 2005.

[76] Kim et al. Multi-resolutional brain network filtering and analysis via wavelets on non-euclidean space. In *MICCAI*, volume 8151 of *Lect. Notes Comp. Sc.*, pages 643–651. Springer, 2013.

[77] S Kintali. Betweenness centrality : Algorithms and lower bounds. *arXiv*, arXiv:0809.1906 [cs.DS], 2008.

[78] I Kostović and N Jovanov-Milošević. The development of cerebral connections during the first 20–45 weeks' gestation. In *Semin. Fetal and Neonat. M.*, volume 11, pages 415–422. Elsevier, 2006.

[79] I Kostović and M Judaš. Correlation between the sequential ingrowth of afferents and transient patterns of cortical lamination in preterm infants. *Anat. Rec.*, 267(1):1–6, 2002.

[80] M Lazar and A L Alexander. An error analysis of white matter tractography methods: synthetic diffusion tensor field simulations. *NeuroImage*, 20(2):1140–1153, 2003.

[81] T B Leergaard, C C Hilgetag, and O Sporns. Mapping the connectome: multi-level analysis of brain connectivity. *Front. Neuroinform.*, 6, 2012.

[82] R K Lenroot and J N Giedd. Brain development in children and adolescents: insights from anatomical magnetic resonance imaging. *Neurosci. Biobehav. R.*, 30(6):718–729, 2006.

[83] D Levine and P D Barnes. Cortical maturation in normal and abnormal fetuses as assessed with prenatal MR imaging. *Radiology*, 210(3):751–758, 1999.

[84] Levitt et al. Cortical sulcal maps in autism. *Cereb. Cortex*, 13(7):728–735, 2003.

[85] Li et al. The correlation of metrics in complex networks with applications in functional brain networks. *J. Stat. Mech. Theory E.*, 2011(11):P11018, 2011.

[86] Li et al. Mapping Putative Hubs in Human, Chimpanzee (Pan troglodytes) and Rhesus Macaque (Macaca mulatta) Connectomes via Diffusion Tractography. *NeuroImage*, 80:462–474, 2013.

[87] Lo et al. Diffusion tensor tractography reveals abnormal topological organization in structural cortical networks in Alzheimer's disease. *J. Neurosci.*, 30(50):16876–16885, 2010.

[88] Lynall et al. Functional connectivity and brain networks in schizophrenia. *J. Neurosci.*, 30(28):9477–9487, 2010.

[89] Makropoulos et al. Automatic whole brain MRI segmentation of the developing neonatal brain. *IEEE T. Med. Imaging*, 33(9):1818–1831, 2014.

[90] Manganaro et al. Assessment of congenital heart disease (CHD): is there a role for fetal magnetic resonance imaging (MRI)? *Eur. J. Radiol.*, 72(1):172–180, 2009.

[91] P Mansfield. Multi-planar image formation using NMR spin echoes. *J. Phys. C: Solid State*, 10(3):L55, 1977.

[92] P Mansfield, A A Maudsley, and T Bains. Fast scan proton density imaging by NMR. *J. Phys. E: Sci. Instrum.*, 9(4):271, 1976.

[93] Mariano et al. A review of atlas-based segmentation for magnetic resonance brain images. *Comput. Meth. Prog. Bio.*, 104(3):e158 – e177, 2011.

[94] Marlow et al. Neurologic and developmental disability at six years of age after extremely preterm birth. *N. Engl. J. Med.*, 352(1):9–19, 2005.

[95] Marlow et al. Motor and executive function at 6 years of age after extremely preterm birth. *Pediatrics*, 120(4):793–804, 2007.

[96] S Maslov and K Sneppen. Specificity and stability in topology of protein networks. *Science*, 296(5569):910–913, 2002.

[97] J J McAuley, L da Fontoura Costa, and T S Caetano. Rich-club phenomenon across complex network hierarchies. *Appl. Phys. Lett.*, 91(8):084103, 2007.

[98] McRobbie et al. *MRI from Picture to Proton*. Cambridge University Press, 2006.

[99] Meskaldji et al. Comparing connectomes across subjects and populations at different scales. *NeuroImage*, 8:416–425, 2013.

[100] D Moreno-Dominguez, A Anwander, and T R Knösche. A hierarchical method for whole-brain connectivity-based parcellation. *Hum. Brain Mapp.*, 35:5000–5025, 2014.

[101] S Mori and P van Zijl. Fiber tracking: principles and strategies – a technical review. *NMR Biomed.*, 15(7-8):468–480, 2002.

[102] Mori et al. Three-dimensional tracking of axonal projections in the brain by magnetic resonance imaging. *Ann. Neurol.*, 45(2):265–269, 1999.

[103] M Newman. *Networks: An Introduction*. Oxford University Press, Inc., New York, NY, USA, 2010.

[104] M E J Newman. Modularity and community structure in networks. *P. Natl. Acad. Sci. USA*, 103(23):8577–8582, 2006.

[105] Oishi et al. Multi-contrast human neonatal brain atlas: Application to normal neonate development analysis. *NeuroImage*, 56(1):8 – 20, 2011.

[106] T. Opsahl and P. Panzarasa. Clustering in weighted networks. *Social Networks*, 31(2):155–163, May 2009.

[107] Opsahl et al. Prominence and control: the weighted rich-club effect. *Phys. Rev. Lett.*, 101(16):168702, 2008.

[108] Panagiotaki et al. Compartment models of the diffusion mr signal in brain white matter: a taxonomy and comparison. *NeuroImage*, 59(3):2241–2254, 2012.

[109] Pandit et al. Traumatic brain injury impairs small-world topology. *Neurology*, 80(20):1826–1833, 2013.

[110] Pandit et al. Whole-brain mapping of structural connectivity in infants reveals altered connection strength associated with growth and preterm birth. *Cereb. Cortex*, 24:2324–2333, 2013.

[111] T P Peixoto. The graph-tool python library. *figshare*, 2014.

[112] J Pipe. Pulse Sequences for Diffusion-Weighted MRI. *Diffusion MRI*, pages 205–236, 2013.

[113] Pruessmann et al. SENSE: sensitivity encoding for fast MRI. *Magn. Reson. Med.*, 42(5):952–962, 1999.

[114] E M Purcell, H C Torrey, and R V Pound. Resonance absorption by nuclear magnetic moments in a solid. *Phys. Rev.*, 69(1):37–38, 1946.

[115] Qiu et al. Changes of brain structure and function in ADHD children. *Brain Topogr.*, 24(3-4):243–252, 2011.

[116] Rabi et al. A new method of measuring nuclear magnetic moment (letter). *Phys. Rev.*, 53:318, 1938.

[117] A R Rao, R Jana, and S Bandyopadhyay. A Markov chain Monte Carlo method for generating random (0, 1)-matrices with given marginals. *Sankhya Ser. A*, 58(2):225–242, 1996.

[118] Reveley et al. Superficial white matter fiber systems impede detection of long-range cortical connections in diffusion MR tractography. *P. Natl. Acad. Sci. USA*, pages e2820–e2828, 2015.

[119] Robinson et al. Identifying population differences in whole-brain structural networks: a machine learning approach. *NeuroImage*, 50(3):910–919, 2010.

[120] I Ronen. Studying brain cytoarchitecture with MRI – Present, future and promises of high field. *Int. J. Imag. Syst. Tech.*, 20(1):57–61, 2010.

[121] M Rubinov and O Sporns. Complex network measures of brain connectivity: uses and interpretations. *NeuroImage*, 52(3):1059–1069, 2010.

[122] Rubinov et al. Small-world properties of nonlinear brain activity in schizophrenia. *Hum. Brain Mapp.*, 30(2):403–416, 2009.

[123] Rueckert et al. Nonrigid registration using free-form deformations: application to breast mr images. *IEEE T. Med. Imaging*, 18(8):712–721, 1999.

[124] Salvador et al. Neurophysiological architecture of functional magnetic resonance images of human brain. *Cereb. Cortex*, 15(9):1332–1342, 2005.

[125] D Schendel and T K Bhasin. Birth weight and gestational age characteristics of children with autism, including a comparison with other developmental disabilities. *Pediatrics*, 121(6):1155–1164, 2008.

[126] B Scherrer, A Gholipour, and S K Warfield. Super-resolution reconstruction to increase the spatial resolution of diffusion weighted images from orthogonal anisotropic acquisitions. *Med. Image Anal.*, 16(7):1465–1476, 2012.

[127] Schirmer et al. Normalisation of Neonatal Brain Network. In *MICCAI*, Lect. Notes Comp. Sc., pages 574–581. Springer, 2013.

[128] Schirmer et al. Parcellation-independent multi-scale framework for brain network analysis. In *C. D. MRI*, pages 23–32. Springer, 2014.

[129] Schnabel et al. A generic framework for non-rigid registration based on non-uniform multi-level free-form deformations. In *MICCAI*, Lect. Notes Comp. Sc., pages 573–581. Springer, 2001.

[130] Serag et al. Construction of a consistent high-definition spatio-temporal atlas of the developing brain using adaptive kernel regression. *NeuroImage*, 59(3):2255–2265, 2012.

[131] D J Sharp, G Scott, and R Leech. Network dysfunction after traumatic brain injury. *Nat. Rev. Neurol.*, 10(3):156–166, 2014.

[132] D Simard, L Nadeau, and H Kröger. Fastest learning in small-world neural networks. *Phys. Lett. A*, 336(1):8–15, 2005.

[133] S L Simpson, S Hayasaka, and P J Laurienti. Exponential random graph modeling for complex brain networks. *PLoS ONE*, 6(5):e20039, 2011.

[134] S Smith. Fast robust automated brain extraction. *Hum. Brain Mapp.*, 17(3):143–155, 2002.

[135] Song et al. Asymmetry of white matter pathways in developing human brains. *Cereb Cortex*, bhu084, 2014.

[136] Sowell et al. Mapping cortical change across the human life span. *Nature neuroscience*, 6(3):309–315, 2003.

[137] Sowell et al. Longitudinal mapping of cortical thickness and brain growth in normal children. *J. Neurosci.*, 24(38):8223–8231, 2004.

[138] O Sporns. The human connectome: a complex network. *Ann. N.Y. Acad. Sci.*, 1224:109–125, 2011.

[139] O Sporns, C J Honey, and R Kötter. Identification and classification of hubs in brain networks. *PLoS ONE*, 2(10):e1049, 2007.

[140] O Sporns, G Tononi, and R Kötter. The human connectome: A structural description of the human brain. *PLoS Comput. Biol.*, 1(4):245–251, 2005.

[141] Sporns et al. Organization, development and function of complex brain networks. *Trends Cogn. Sci.*, 8(9):418–425, 2004.

[142] E O Stejskal and J E Tanner. Spin diffusion measurements: spin echoes in the presence of a time-dependent field gradient. *J. Chem. Phys.*, 42(1):288–292, 1965.

[143] J Stiles and T L Jernigan. The basics of brain development. *Neuropsychol. Rev.*, 20(4):327–348, 2010.

[144] Supekar et al. Network analysis of intrinsic functional brain connectivity in Alzheimer's disease. *PLoS Comput. Biol.*, 4(6):1–11, 2008.

[145] Takahashi et al. Development of cerebellar connectivity in human fetal brains revealed by high angular resolution diffusion tractography. *NeuroImage*, 96:326–333, 2014.

[146] Q K Telesford, J H Burdette, and P J Laurienti. An exploration of graph metric reproducibility in complex brain networks. *Front. Neurosci.*, 7(67), 2013.

[147] Tocchio et al. MRI evaluation and safety in the developing brain. In *Semin. Perinatol.*, volume 39, pages 73–104. Elsevier, 2015.

[148] Towlson et al. The rich club of the c. elegans neuronal connectome. *J. Neurosci.*, 33(15):6380–6387, 2013.

[149] J Travers and S Milgram. An experimental study of the small world problem. *Sociometry*, 32(4):425–443, 1969.

[150] Tustison et al. N4itk: improved n3 bias correction. *IEEE T. Med. Imaging*, 29(6):1310–1320, 2010.

[151] Tymofiyeva et al. Towards the "baby connectome": mapping the structural connectivity of the newborn brain. *PLoS ONE*, 7(2):e31029, 2012.

[152] Tymofiyeva et al. A DTI-Based Template-Free Cortical Connectome Study of Brain Maturation. *PLoS ONE*, 8(5):e63310, 2013.

[153] Tymofiyeva et al. Brain without anatomy: construction and comparison of fully network-driven structural mri connectomes. *PLoS ONE*, 9(5):e96196, 2014.

[154] Tymofiyeva et al. Structural MRI connectome in development: challenges of the changing brain. *Brit. J. Radiol.*, 87(1039):1–14, 2014.

[155] Tzourio-Mazoyer et al. Automated Anatomical Labeling of Activations in SPM Using a Macroscopic Anatomical Parcellation of the MNI MRI Single-Subject Brain. *NeuroImage*, 15(1):273 – 289, 2002.

[156] M P van den Heuvel and M A de Reus. Chasing the dreams of early connectionists. *ACS Chem. Neurosci.*, 5(7):491–493, 2014.

[157] M P Van den Heuvel and O Sporns. Rich-club organization of the human connectome. *The Journal of neuroscience*, 31(44):15775–15786, 2011.

[158] M P Van den Heuvel and O Sporns. Network hubs in the human brain. *Trends Cogn. Sci.*, 17(12):683–696, 2013.

[159] Van den Heuvel et al. Small-world and scale-free organization of voxel-based resting-state functional connectivity in the human brain. *NeuroImage*, 43(3):528–39, 2008.

[160] Van den Heuvel et al. Efficiency of functional brain networks and intellectual performance. *J. Neurosci.*, 29(23):7619–7624, 2009.

[161] Van den Heuvel et al. Aberrant frontal and temporal complex network structure in schizophrenia: a graph theoretical analysis. *J. Neurosci.*, 30(47):15915–15926, 2010.

[162] Van den Heuvel et al. High-cost, high-capacity backbone for global brain communication. *P. Natl. Acad. Sci. USA*, 109(28):11372–11377, 2012.

[163] Van den Heuvel et al. The neonatal connectome during preterm brain development. *Cereb. Cortex*, page bhu095, 2014.

[164] Van Wijk et al. Comparing brain networks of different size and connectivity density using graph theory. *PLoS ONE*, 5(10):e13701, 2010.

[165] G. Varoquaux and R C Craddock. Learning and comparing functional connectomes across subjects. *NeuroImage*, 80:405–415, 2013.

[166] Vasanawala et al. Practical parallel imaging compressed sensing MRI: Summary of two years of experience in accelerating body MRI of pediatric patients. In *Proc. IEEE Int. Symp. Biomed. Imaging*, pages 1039–1043. IEEE, 2011.

[167] Walsh et al. Assessment of fetal lung volumes and liver herniation with magnetic resonance imaging in congenital diaphragmatic hernia. *Am. J. Obstet. Gynecol.*, 183(5):1067–1069, 2000.

[168] Wang et al. Altered small-world brain functional networks in children with attention-deficit/hyperactivity disorder. *Hum. Brain Mapp.*, 30(2):638–49, 2009.

[169] D J Watts and S H Strogatz. Collective dynamics of 'small-world' networks. *Nature*, 393(6684):440–442, 1998.

[170] C Weigert. Über eine neue Untersuchungsmethode des Centralnervensystems. *Z Med Wiss*, 20. Jahrgang(42):753–757, 1882.

[171] C Weigert. Über eine neue Untersuchungsmethode des Centralnervensystems. *Z Med Wiss*, 20. Jahrgang(43):772–774, 1882.

[172] C Wernicke. Der aphasische Symptomencomplex: Eine psychologische Studie auf anatomischer Basis. 1874.

[173] Williams et al. Neonatal brain: Regional variability of in vivo mr imaging relaxation rates at 3.0 t - initial experience. *Radiology*, 235(2):595–603, 2005.

[174] Wilson-Costello et al. Improved neurodevelopmental outcomes for extremely low birth weight infants in 2000–2002. *Pediatrics*, 119(1):37–45, 2007.

[175] Wood et al. Neurologic and developmental disability after extremely preterm birth. *New Engl. J. Med.*, 343(6):378–384, 2000.

[176] Xi et al. Adapting parcellation schemes to study fetal brain connectivity in serial imaging studies. In *Conf. Proc. IEEE Eng. Med. Biol. Soc.*, pages 73–76, 2013.

[177] Xu et al. Radial coherence of diffusion tractography in the cerebral white matter of the human fetus: neuroanatomic insights. *Cereb. Cortex*, 24(3):579–592, 2014.

[178] Yap et al. Development trends of white matter connectivity in the first years of life. *PLoS ONE*, 6(9):e24678, 2011.

[179] Zalesky et al. Whole-brain anatomical networks: does the choice of nodes matter? *NeuroImage*, 50(3):970–83, 2010.

[180] S Zhou and R J Mondragón. The rich-club phenomenon in the internet topology. *IEEE Commun. Lett.*, 8(3):180–182, 2004.